An assessment of the global, seasonal, and interannual spacecraft record of Martian climate in the thermal infrared

Junjun Liu and Mark I. Richardson

Division of Geological and Planetary Sciences, California Institute of Technology, Pasadena, California, USA

R. J. Wilson

NOAA/Geophysical Fluid Dynamics Laboratory, Princeton, New Jersey, USA

[1]   Intercomparison of thermal infrared data collected by Mariner 9, Viking, and Mars Global Surveyor (MGS) is presented with a specific focus on air temperatures, dust opacities, and water ice opacities. Emphasis is placed on creating a uniform data set to most effectively reduce interinstrument biases and offsets. The annual cycle consistently shows a strong asymmetry about the equinoxes, with northern spring and summer exhibiting relatively low temperatures, very high year-to-year repeatability, and essentially no short-term (tens of days) variability. The globally averaged Martian nighttime air temperatures close annually to within a Kelvin during northern spring and summer. Daytime temperatures show more variability (3–6 K). The difference in repeatability of daytime versus nighttime temperatures is not understood. Viking and MGS air temperatures are essentially indistinguishable for this period, suggesting that the Viking and MGS eras are characterized by essentially the same climatic state. Southern summer is characterized by strong dust storm activity and hence strong year-to-year air temperature variability. Dust opacity shows a remarkable degree of interannual variability in southern spring and summer, associated with the intermittent activity of regional and planet-encircling dust storms, but exhibits high year-to-year repeatability in northern spring and summer. Specifically, late northern spring and early northern summer dust opacities appear to be completely insensitive to the occurrence (or not) of major dust storms in the previous southern spring or summer. We show that both Viking and MGS data sets exhibit significant (and similar) polar cap edge dust storm activity. The origins of the various major dust storms can be identified in the thermal infrared data from Viking and MGS, including the transport of dust from the northern autumn baroclinic zone into the southern hemisphere tropics, which has also been identified in visible imaging. We also note that the period around $L_s = 225°$ is characterized by very high dust opacities associated with dust storm development or decay in every year thus far observed by spacecraft. Water ice opacities have been retrieved from Viking infrared data for the first time. We show that the northern spring and summer tropical cloud belt structure and evolution are essentially the same in each of the multiple years observed by Viking and MGS. Relatively subtle spatial features recur in the cloud belt from year to year, suggesting the influence of surface topography and thermophysical properties and a reasonably consistent supply of water vapor. The seasonal evolution of the tropical cloud belt through northern spring and summer is shown, with the only significant deviations between years occurring from $L_s = 140°$ to $160°$, where opacities fall in the second MGS year associated with a small dust storm. Polar hood clouds are observed in Viking and MGS observations with similar timing and extent. Interactions between dust and water ice were highlighted in the Hellas basin region during the southern spring 1977a and 2001 dust storms. The observations demonstrate that the Martian atmosphere executes a very "repeatable" annual cycle of atmospheric phenomena. However, a major part of this cycle is the occurrence of highly variable and potentially major dust storm events. After such dust storm events the atmosphere rapidly relaxes to its stable, repeatable state.   *INDEX TERMS:* 5409 Planetology: Solid Surface Planets: Atmospheres—structure and dynamics; 6225 Planetology: Solar System Objects: Mars; 3309 Meteorology and Atmospheric Dynamics:

1. Introduction

[2] In order to develop an understanding of the Martian climate, and hence to be able to build valid predictive models, a good climatology of the annual cycle is required. This climatology must consist of (at least) information about the spatial and temporal behavior of air temperature and the radiatively active aerosols: dust and water ice. To be sure of the representativeness of the climatology, a uniform baseline of observations extending over multiple years is required. Fortunately, such data sets are now available in multiple forms. High-spatial and temporal resolution thermal infrared data exist from Mariner 9, Viking, and Mars Global Surveyor (MGS) extending (discontinuously) over 18 Mars years [*Hanel et al.*, 1972; *Conrath*, 1975; *Fenton et al.*, 1997; *Martin and Kieffer*, 1979; *Martin*, 1981, 1986; *Leovy*, 1985; *Tamppari et al.*, 2000; *Wilson and Richardson*, 2000; *Conrath et al.*, 2000; *Smith et al.*, 2000, 2001a; *Pearl et al.*, 2001]. These missions also provide a somewhat less uniform record of visible images [*Anderson and Leovy*, 1978; *Kahn*, 1984; *Cantor et al.*, 2001; *Wang and Ingersoll*, 2002]. A disk-integrated, multiannual record of air temperature (and other variables) is available from ground-based microwave observations [*Clancy et al.*, 1990, 1996, 2000]. Finally, Hubble Space Telescope imaging has provided information on dust and water ice hazes [*Clancy et al.*, 1996; *James et al.*, 1996]. In this paper, we will concentrate on the infrared spacecraft record, as it provides the highest temporal and spatial resolution.

1.1. Interannual Variability of the Global-Mean Climate

[3] Interest in interannual variability of the Martian atmosphere initially centered on the repeatability of the dust storms. Questions focused on whether planet-encircling dust storms occurred every year, and if not, how frequently they did occur and with what distribution of size as a function of year. These kinds of studies led to works such as *Martin and Zurek* [1993] and *Zurek and Martin* [1993]. Difficulties with these studies related to the nature of the predominantly ground-based telescopic nature of the data set, and the inevitably somewhat arbitrary definition of a "planet-encircling dust storm".

[4] The focus of interannual variability broadened greatly in the 1990s thanks to the work of Todd Clancy [*Clancy et al.*, 1990, 1996]. A growing record of the Martian atmosphere from ground-based microwave observations (1980 to present) allowed quantitative comparison of earth-facing, disk-integrated air temperatures to be undertaken. The most important result of these microwave observations was that Mars appeared much colder than observed by Viking during the northern spring and summer seasons of 1976 and 1978. This apparently large temperature drop would represent a massive shift in the Martian climate (15−20 K) within only one or two Martian years. On the basis of the much cooler temperatures, *Clancy et al.* [1996] suggested that the water condensation level should be quite low (∼15 km) and that

extensive water ice clouds should form in the tropics at this season. Indeed, such clouds were just beginning to be found in the atmosphere at that time using the Hubble Space Telescope [*Clancy et al.*, 1996; *James et al.*, 1996]. These results prompted a new, very asymmetric paradigm for the Martian annual cycle: a northern spring and summer which is relatively cool, not very dusty, and relatively rich in water vapor and ice clouds; and a southern summer rather similar to that observed by Viking with warmer air temperatures, less water vapor and water ice, and higher levels of atmospheric dust.

[5] Significant, near steady state interannual shifts in the Martian northern spring and summer climate over only a couple of Martian years would have generated profound challenges for theories of Martian climate dynamics. However, by carefully comparing sparse Viking Infrared Thermal Mapper (IRTM) data [*Martin*, 1981] from 1980 (which were not included in the *Clancy et al.* [1990, 1996] studies) and a simultaneous microwave observation during late northern summer, *Richardson* [1998] demonstrated that no interannual shift in climate had in fact occurred. *Richardson* [1998] showed that the zonal mean temperatures during northern spring and summer are highly repeatable in all years for which data were then available, and that the discrepancy between microwave and IRTM observations was in fact due to an instrumental artifact in one or another of the data sets. *Wilson and Richardson* [2000], examining diurnal temperature variability, demonstrated that it is the IRTM air temperature data that are biased high, most likely due to a leakage of surface radiation into the 15-μm air-temperature channel. They proceeded to suggest a "correction" for the IRTM 15-μm channel based on the physics of the instrument and the degree of adjustment required to bring the data into agreement with tidal theory, which incidentally brought the IRTM data (which are described in their "uncorrected" form by *Martin* [1981]) into better agreement with the microwave data. As a result of these studies, we now know that while the suggestion of a strong cooling of climate between the late-1970s and early 1980s [*Clancy et al.*, 1990, 1996] is incorrect, it is the microwave record of air temperatures which is the most representative [*Clancy et al.*, 1996], even for the period observed by Viking.

[6] MGS Thermal Emission Spectrometer (TES) observations from 1997 have been shown to be consistent with the microwave observations [*Clancy et al.*, 2000]. These confirmed cool temperatures present a problem, though, in terms of the dust opacity record from the Viking Landers (VL) [*Colburn et al.*, 1989], which shows opacities sufficiently high in northern summer as to appear inconsistent with the air temperatures (it should be noted, though, that the comparison between observed and modeled dust opacities are extremely fraught due to ambiguities in dust properties and vertical distribution). This aspect of the Viking climate record has been reexamined by *Toigo and Richardson* [2000] using simultaneous thermal infrared observations from IRTM and visible observations from

the Viking landers. By using the *Martin* [1986] IR opacity scheme and the Planetary Data System (PDS) archive of VL opacities [*Colburn et al.*, 1989], they showed that the ratio of the visible-to-infrared opacity at these two sites varies strongly, but systematically with season. Eliminating effects due to particle size and the vertical distribution assumed for dust in the IR retrieval, they show that the VL opacity measurements convolve two different aerosol opacities. During southern summer, the VL opacities correspond almost exclusively to dust opacity, with a visible-to-infrared ratio of 2.5 (as reported by *Martin* [1986] for this season). However, during northern spring and summer, much of the visible opacity is generated by water ice aerosols. As such, the dust visible opacity is much lower in northern spring and summer than reported by *Colburn et al.* [1989] ($<0.1 - 0.4$ vs. 0.6) [*Toigo and Richardson*, 2000].

1.2. Spatial Structure in Dynamical Phenomena

[7] Much of the work on interannual variability discussed above is essentially focused on the temporal evolution of global-mean or globally representative quantities. Significant work, albeit not within the context of interannual variability, has been undertaken on the spatial (geographic) behavior of Martian climate, including the seasonal evolution of water ice clouds [*Kahn*, 1984; *Tamppari et al.*, 2000; *Pearl et al.*, 2001] and the development of regional and planet-encircling dust storms [*Briggs et al.*, 1979; *Martin and Richardson*, 1993; *Fenton et al.*, 1997; *Smith et al.*, 2000, 2002; *Cantor et al.*, 2001; *Wang and Ingersoll*, 2002]. These studies used different types of data from three spacecraft:

[8] 1. Mariner 9. Television [*Leovy et al.*, 1972] and Infrared Interferometer Spectrometer (IRIS) [*Hanel et al.*, 1972] data were collected by the Mariner 9 mission in 1970–71. The Mariner 9 data sets cover the period of $L_s = 293° - 98°$ (where L_s is the seasonal indicator, measured in degrees, with $L_s = 0°$ defining northern spring equinox, $L_s = 90°$ northern summer solstice, etc.), with the majority of the data being collected between $L_s = 293° - 350°$ during the decay phase of a planet-encircling dust storm. As such, Mariner 9 does not provide information for a full annual cycle.

[9] 2. Viking. Twin Viking Orbiters each carried a two-color imager [*Briggs et al.*, 1979] and an Infrared Thermal Mapper [*Martin and Kieffer*, 1979]. Viking Orbiter 1 operated from June 1976 until July 1980, while Orbiter 2 operated from August 1976 to July 1978. The Viking Orbiter observations possessed good coverage for one-and-a-third Martian years, starting at $L_s = 84°$. Sparser coverage from Orbiter 1 extends from $L_s \sim 340°$ until the demise of that spacecraft. Both orbiters were in elliptical and relatively long-period orbits. Consequently the data were not collected in a regular, uniform, or repeating pattern. Two large dust storms occurred during the only southern summer observed by the Viking Orbiters. Parts of northern spring and summer of three Martian years were observed.

[10] 3. Mars Global Surveyor. Spatially resolved and high coverage atmospheric data from MGS primarily originate with the Mars Orbiter Camera (MOC) [*Malin et al.*, 1992] and the Thermal Emission Spectrometer (TES) [*Christensen et al.*, 1992, 2001]. MGS has been collecting data at Mars since September 1997. Between orbit insertion and the attainment of a circular mapping orbit in February 1999

($L_s = 179° - 99°$), MGS observations were noncontinuous and obtained from a decreasingly eccentric orbit [*Albee*, 2000]. During the mapping mission, the data have been acquired from a circular, near-polar orbit with a roughly 2-hour period. The orbit is held at a fixed local time, such that observations are at 2 am and 2 pm local time (this local time actually varies by several tens of minutes in either direction over the course of a Martian year). The MGS observations are therefore the most systematic of any of the spacecraft yet sent to Mars, although the range of local times sampled by the spacecraft are obviously much more restricted than those sampled by Viking.

[11] The origins of regional and planet-encircling dust storms, and the mechanisms by which they grow remain mysteries at some level. The growth of several storms have been observed by Viking and MGS including two planet-encircling dust storms in 1977 [*Briggs et al.*, 1979; *Martin and Richardson*, 1993], several regional [*Briggs et al.*, 1979; *Peterfreund and Kieffer*, 1979; *Peterfreund*, 1985; *Kahn et al.*, 1992; *Smith et al.*, 2000, 2001a, 2001b; *Cantor et al.*, 2001; *Wang and Ingersoll*, 2002], and many local dust storms [*Peterfreund*, 1985; *Cantor et al.*, 2001]. The two Viking planet-encircling dust storms were observed to begin in the Thaumasia Fossae region (45°S, 95°W) near $L_s = 205°$, and either in Isidis or in Solis Plantum near $L_s = 274°$ [*Briggs et al.*, 1979; *Martin and Richardson*, 1993]. Discerning the origins of the Viking storms is made difficult due to the relatively poor coverage in imaging and thermal infrared, as compared to MGS. A planet-encircling storm was observed by MGS in 2001 [*Smith et al.*, 2002]. This storm began just after $L_s = 180°$ as with dust lifting within and near Hellas Planitia. Several regional storms have also been observed by MGS [*Cantor et al.*, 2001, 2002; *Smith et al.*, 2000, 2001a, 2001b]. The Noachis storm of 1997 was observed to initiate in the high southern latitudes, not far from the seasonal cap edge and just to the west of the large Hellas Basin [*Smith et al.*, 2000; *Cantor et al.*, 2001]. Regional storms during the succeeding Mars year showed even more interesting behavior, with several storms beginning in late northern summer and early northern autumn as fronts developing near the edge of the northern polar vortex. These dust storms then become entrained in the lower branch of the Hadley circulation, and are subsequently swept into the southern tropics [*Wang et al.*, 2003]. We will discuss this phenomenon, as viewed in the infrared data, in more detail in the body of this paper. Finally, *Cantor et al.* [2001] point out some apparent differences in the location of local storm activity between Viking and MGS. Viking and "historical" observations (derived from ground-based telescopes) suggest local storms originate at a range of latitudes, and may show a modest tendency to track the subsolar latitude [*Peterfreund*, 1985; *Kahn et al.*, 1992]. *Cantor et al.* [2001] show that by far the majority of local storms observed by MGS were situated near the seasonal cap edge. These presumably result from surface thermal contrasts in those regions. It is open for debate whether this difference represents a change in the character of Martian local storms, or the improvement in observational coverage afforded by MGS. We will return to this point, also.

[12] The tropical cloud belt was discussed by *Slipher* [1962] and *Beish and Parker* [1990], but its significance as a component of the climate was not fully appreciated until the advent of Hubble Space Telescope (HST) observations of

Table 1. Correspondence Between the Year Designations Used in This Paper and Other Dating Systems and Events[a]

Year Designation Used in This Paper	Calendar Years (Part)	*Clancy et al.* [2000] Year	Spacecraft	Dust Storm Events
IRIS	1971–1972	9–10	Mariner 9	1971
Viking Year 1	1976–1977	12	Viking Orbiters 1 and 2	1977a, 1977b
Viking Year 2	1977–1979	13	Viking Orbiters 1 and 2	
Viking Year 3	1979–1980	14	Viking Orbiter 1	
TES Year 1	1997–1998	23	MGS (aerobraking and SPO)	Noachis
TES Year 2	1998–2000	24	MGS (SPO and 1st mapping year)	"flushing" storm
TES Year 3	2000–2002	25	MGS (2nd mapping year)	2001
TES Year 4	2002–2003	26	MGS (3rd mapping year)	[b]

[a]Each year is defined to start from $L_s = 0°$ except for the IRIS data, where the observation period extends from $L_s = 293°$ in Year 9 of the *Clancy et al.* [2000] calendar to $L_s = 98°$ of Year 10.
[b]Note: Southern spring and summer data had not been collected at the time of this publication.

Mars in the mid-1990s [*Clancy et al.*, 1996; *James et al.*, 1996]. From HST observations, it became apparent that the belt is most prominent during late northern spring and early northern summer. The existence of the belt during the Viking mission was realized in analysis of IRTM data by *Tamppari et al.* [2000]. The *Tamppari et al.* [2000] study shows the formation of a tropical cloud belt around $L_s = 65°$ and decaying at some point after $L_s = 125°$. MGS observations show that the cloud belt initiation and termination are gradual events, although punctuated with rapid changes in optical thickness [*Pearl et al.*, 2001; *Wang and Ingersoll*, 2002]. We will discuss the evolution of the tropical cloud belt in Viking and MGS observations in greater detail within the body of this paper.

1.3. Understanding the Observations: How Well Can We Model Them?

[13] The records of air temperature, dust, and water ice provide combined constraints on the dynamical behavior of the atmosphere. However, insight into the nature of these dynamics is limited without a physical framework within which to place the observations. This framework is provided by general circulation models (GCM). One area of ongoing work with these models focuses on explaining the annual cycle of air temperatures in terms of the seasonal evolution of dust [*Forget et al.*, 1999; *Lewis et al.*, 1999; *Wilson and Richardson*, 2000]. An important part of this is understanding the seasonal evolution of the dust in the atmosphere, with models now including simple schemes for dust injection at the surface, and transport of radiatively active dust within the atmosphere [*Wilson and Hamilton*, 1996; *Newman et al.*, 2002]. As such, defining a valid description of the Martian climate, including mean behavior and some gauge as to the degree of variability, is essential for providing a "target" for the GCMs to shoot at, and in return allowing the GCMs to provide a predictive, quantitative gauge of how well we understand the seasonal evolution of Martian climate and the mechanisms operating therein.

[14] Understanding the dynamical mechanisms of dust storm evolution provides a major challenge for observational science and dynamical modeling. While the decay of storms appears relatively well understood, insofar as GCMs are able to predict dust fallout consistent with observed time-scales [*Murphy et al.*, 1990, 1993; *Wilson and Hamilton*, 1996; *Wilson and Richardson*, 1999], their origins remain obscure. However, analysis of higher resolution data provided by MGS combined with dynamical modeling holds out hope that these important systems will be understood at some

point. In particular, the observations now show distinct categories of behavior, including the development of storms near the cap edge, as part of frontal storm systems, and in regions with strong topographic slope, the entrainment of dust in global scale wind systems, and the merging of regional scale storms into coherent global systems [*Cantor et al.*, 2001]. The data are most helpful in specifying a range of tangible phenomena in which each of the models can aim at sequentially improved representation.

[15] The location of the tropical cloud belt just north of the equator in northern spring and summer prompts an obvious suggestion that it is associated in some way with the Hadley circulation [*Clancy et al.*, 1996; *Tamppari et al.*, 2000]. To date, the only published attempt to examine this structure with a numerical model is that of *Richardson et al.* [2002]. This study suggests that the cloud belt forms as water vapor condenses in the Hadley upwelling belt. The location of the cloud belt is a function of asymmetric vapor supply (from the north), the location of upwelling plumes that form the Hadley cell, and the size of ice particles. High spatial and temporal resolution observations of the origin and decay of the cloud belt, and of the degree to which this cycle varies from year-to-year will provide important constraints on models and should allow more detailed insight into the nature of dynamics, water ice microphysics, and the water cycle.

1.4. This Work

[16] We stated at the beginning of this introduction that what is needed to make significant progress in developing mechanistic understanding of the Martian atmosphere is a spatially resolved climatology that defines a "typical" or "average" annual cycle of air temperatures and radiatively-active aerosols, and an understanding of the temporal and spatial deviations from this typical cycle. In order to develop such a record, spatially resolved data from multiple Martian years are required. Further, the data sets must either be uniform in the sense that essentially the same type of raw data is available for each year, or have sufficient overlap of operation that the systems are effectively cross-calibrated. The latter criteria have not yet been met for Martian observations. However, the infrared record of the Martian atmosphere available from Mariner 9 IRIS, Viking IRTM, and MGS TES meets the first criteria, and as such we can now begin to assemble an initial version of a Martian climatology (the years covered and our naming convention for these various years is described in Table 1). The key to assembling the raw data into a uniform data set is convolving the IRTM channel spectral response functions with the

higher spectral resolution IRIS and TES data. This allows the generation of essentially uniform data sets that extends from 1971 to the present, covering parts of at least 9 Martian years, and with a 18 Mars year spread from the earliest Mariner 9 observation to the latest from MGS. While significant data gaps exist, complete annual cycles are available from the late 1970s and from 1997 to present. The combined data set is essentially identical in form to that of the Viking IRTM record, and can be analyzed with tools developed for that instrument. Only by generating this kind of uniform data set can ambiguities in retrieval and technique be eliminated, reducing the possibility of aliasing instrument/retrieval biases as interannual variability.

[17] In this paper, we initially describe the method by which we obtain the consistent, IRTM-like data set across the full suite of infrared spacecraft observations. We also discuss the retrieval schemes used to extract quantitative information about dust and water ice opacity, and examine their validity. We then proceed to examine the records of air temperature, dust opacity, and water ice opacity sequentially. We focus on defining a typical annual cycle for each variable, and on gauging the degree of interannual variability. We also examine the spatial structure of perturbations. For example, the combined data set provides the first completely uniform means to intercompare the large dust storms observed by Mariner 9 and Viking with the regional and global storms observed by MGS. The results are summarized in section 6.

[18] Note that all maps shown in this paper use east longitude, with the maps having the prime meridian at center. Longitudes in the western hemisphere are shown with negative values. Also note that almost all maps (and some of the other figures) in the official electronic version of this paper are in color (the figures can also be found at http://www.gps.caltech.edu/~mir).

2. Description of Retrieval Scheme

[19] The purpose of this study is to examine interannual behavior and variability of the Martian climate over the course of the spacecraft data record. This data takes the form of infrared spectral observations from Mariner 9 (IRIS), Viking (IRTM), and MGS (TES). Unfortunately, the data sets are heterogeneous: IRIS was a 2.4 cm^{-1} resolved spectrometer, IRTM a 5-channel thermal infrared radiometer, and TES a (generally) 10 cm^{-1} resolved spectrometer. Thankfully, the IRTM band passes were sufficiently wide so that "synthetic" or equivalent IRTM channel data can be generated from both IRIS and TES data sets. This is done by applying the measured spectral response functions for IRTM (shown in Figure 1) to IRIS and TES radiances, and then converting these band integrated radiances to IRTM channel brightness temperatures using calibration curves measured for the IRTM channels before launch.

2.1. Air Temperature

[20] Retrieval of air temperatures is essentially complete with the generation of IRTM-equivalent 15-μm band brightness temperatures (henceforth referred to as *T15*) from IRIS and TES. These data provide information on air temperature throughout a significant fraction of the lower atmosphere, with peak information content centered at the 0.5 mbar (~25 km) level. The weighting function for *T15* is shown in
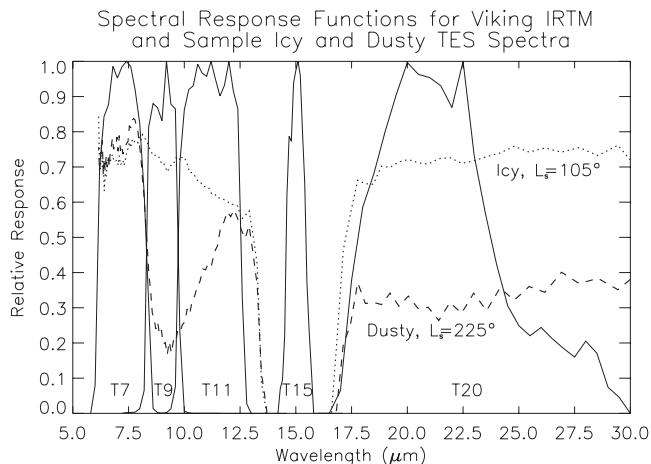

Figure 1. Spectral response functions for the Viking Infrared Thermal Mapper infrared channels. The solid curves show the response functions for each of the channels, with labels below each curve. Also shown are TES spectra corresponding to cloudy and dusty atmospheres (collected at $L_s = 105°$ and $L_s = 225°$, respectively).

Figure 1 of *Wilson and Richardson* [2000]. Measurement uncertainty in the individual *T15* measurements can be as high as 2.5 K for IRTM, the sources of which are discussed by *Martin and Kieffer* [1979]. We take a similar uncertainty as being appropriate for the TES- and IRIS-derived *T15* values. Most of the temperature data presented in this paper have been binned in substantial numbers, with the TES data benefiting from higher data volume than the IRTM data. For quantitative comparison of temperatures, in which we are generally only interested in the globally integrated value, we additionally average over multiple spatial bins. Thus the random instrument error in our integrated, global temperature measurements is typically substantially less than 0.5 K.

[21] The record of temperature derived from Viking IRTM *T15* data provided the standard picture of the Martian annual cycle before the advent of TES observations [*Martin and Kieffer*, 1979; *Leovy*, 1985]. However, it was only recently recognized that this channel was likely affected by a leakage of surface radiation outside of the measured spectral response function [*Wilson and Richardson*, 2000]. This suggested that biasing of the *T15* data may have had an impact on dust opacities retrieved from IRTM data using the *Martin* [1986] scheme, due to the role of *T15* in defining the air temperature profile in that retrieval scheme. In this paper, we examine the "leakage hypothesis" and the "correction" algorithm suggested by *Wilson and Richardson* [2000]. We then examine the impact of this leakage on retrieved dust opacities in section 2.2.2.5. While this effect may also influence the retrieval of water ice opacity (which we examine), this paper provides the first retrieval of water ice opacity from IRTM data, and thus discrepancies arising do not modify previous published results.

2.2. Dust Opacity
2.2.1. *Martin* [1986] Dust Opacity Retrieval Scheme
[22] Dust opacities are retrieved from the IRTM and equivalent IRTM data derived from IRIS and TES using a

modified version of the retrieval scheme developed by *Martin* [1986] and later employed by *Martin and Richardson* [1993] and *Martin* [1995] to study Viking era dust behavior, and by *Fenton et al.* [1997] to derive dust opacities during the Mariner 9 mission. The scheme makes use of the fact that the 9-μm channel of IRTM is situated on a strong silicate absorption feature, as shown in Figure 1. By contrasting the brightness temperatures in the 9-μm (absorption feature) and 7-μm (continuum) channels (henceforth *T9* and *T7*, respectively), a measure of the relative dustiness of the atmosphere can be gained. This measure is made quantitative in the Martin scheme by defining an air temperature profile, constrained by *T15* and a model of the surface-atmosphere temperature contrast, and by then calculating the top-of-the-atmosphere (TOA) *T9* and *T7* brightness temperatures using a scattering radiative transfer model. Dust optical properties are based on *Toon et al.* [1977], which provides a very good model of dust spectra in the thermal infrared at wavelengths short of the 15-μm CO_2 band. A modified gamma particle size distribution is used with r_{eff} = 1.6 μm and υ_{eff} = 0.2, following *Tomasko et al.* [1999]. The scheme is iterative in that a Newtonian convergence code is used to drive opacity in the direction necessary to match the model $T7 - T9$ with that observed. In practice, roughly three iterations are typically required to reach agreement in modeled and observed $T7 - T9$ of less than 0.5%. This scheme is extensively described by *Martin* [1986]. In particular, the error for individual retrievals is assessed to be less than 25% (for $T7 - T9$ = 2 K, and 10% for $T7 - T9$ = 10 K). Averaging over the large data volumes substantially reduces this random uncertainty in opacity measurement.

2.2.2. Improvement to the Martin Scheme

[23] For this study, we have implemented a number of improvements and adaptations in the retrieval scheme. These include incorporation of global thermal inertia, albedo, and emissivity maps, topographic correction, and the ability to distribute dust nonuniformly in the vertical.

2.2.2.1. Global Albedo and Thermal Inertia

[24] Thermal inertia and albedo values derived from global maps are used in the retrieval scheme to constrain the surface-atmosphere temperature contrast with the aid of thermal model results [*Martin*, 1986]. In addition, the albedo was been used in the original *Martin* [1986] scheme to derive surface emissivity, using the relationship of *Christensen* [1982]. Albedo is not used for this purpose in our study (see section 2.2.2.4). In previously published works, albedo and thermal inertia maps from *Pleskot and Miner* [1981] and *Palluconi and Kieffer* [1981] have been used, which only extend from 60°S and 60°N. For this study, we use fully global thermal inertia and albedo maps generated from the blending of the *Pleskot and Miner* [1981] and *Palluconi and Kieffer* [1981] maps with the polar maps derived by *Vasavada et al.* [2000].

2.2.2.2. Vertical Distribution

[25] Dust was assumed to be uniformly distributed in the vertical (i.e., was assumed to have uniform mass mixing ratio as a function of height) in previous applications of the Martin scheme. This assumption has been relaxed in this study (and in that of *Toigo and Richardson* [2000]) so that a nonuniform vertical distribution function can be specified. Typically, this function is that devised by *Conrath* [1975] on

the basis of IRIS observations of the decay of the 1971 planet-encircling dust storm, and we use a typical vertical distribution parameter value of ν = 0.03, which corresponds to a transition from uniform to essentially zero dust at roughly 35 km [see *Haberle et al.*, 1999, Figure 2]. *Toigo and Richardson* [2000] examined the impact of dust vertical distribution on retrieved opacity, and found that the impact of relatively shallow distributions likely appropriate for low opacity conditions during northern spring and summer is quite small (<10%).

2.2.2.3. Topographic Normalization or "Correction"

[26] The Martin scheme provides a retrieval of the total column opacity of dust. Maps of dust opacity from *Martin* [1986], *Martin and Richardson* [1993], and *Fenton et al.* [1997] provide insight into the global distribution of this quantity. While this represents a measure of the total amount of dust in a given atmospheric column, it should be noted that such a presentation can mask dynamically-induced variations in dust distribution (such as those associated with active dust lifting) with variations due to the depth of the atmospheric column. Because the range of Martian topography is quite large (over one scale height, or 10 km), the variation of column opacity due to this affect alone is significant. This can be seen in Figure 2. Opacity maps for the period L_s = 225°–230° from the first TES mapping year show the opacity normalized to the MOLA reference elevation (Figure 2a) and compared with the full nadir opacity (Figure 2b). The topography correction is undertaken assuming a scale height of 10 km, consistent with the value for the bulk atmosphere. Figure 2c shows the difference between these maps, indicating the degree of dust variability due only to topography. The magnitude of the topographic effect is around 0.1–0.2, or 20–40% of the total column opacity. The difference map obviously corresponds very well to the MOLA topography map, and the effect on the opacity map is to diminish the opacity for low topographic regions (such as the Hellas Basin, and the Acidalia, Arcadia, and Utopia Planitia) and to increase it somewhat over high regions (such as the Tharsis Plateau). Note, for example, the "topographic dust storms" in the Hellas basin (30°S and 60°W) and in the northern plains (north of 30°N and at 160°W and 190°W) that disappear in the corrected data. It should be noted, though, that the topographic correction in this case does not remove all of the structure in the opacity map because at this season, several major regional dust storms were occurring (discussion in section 4). In this paper, topographically corrected (or simply normalized) dust opacities are shown and discussed, unless otherwise stated. These normalized opacities provide much better insight into the relative distribution of the dust mixing ratio.

2.2.2.4. Global Emissivity Maps

[27] Variations in the emissivity of the surface at 7 and 9 μm can generate differences between *T7* and *T9* in the absence of dust. In the presence of dust, the difference in emissivity at 7 and 9 μm will influence the retrieved dust opacity, biasing it high or low depending on the sign of the difference. Previous versions of the Martin scheme have used the observed relationship between albedo and the emissivity in these two bands derived by *Christensen* [1982]. More accurate maps of emissivity in the IRTM bands have been published in the time interval since this
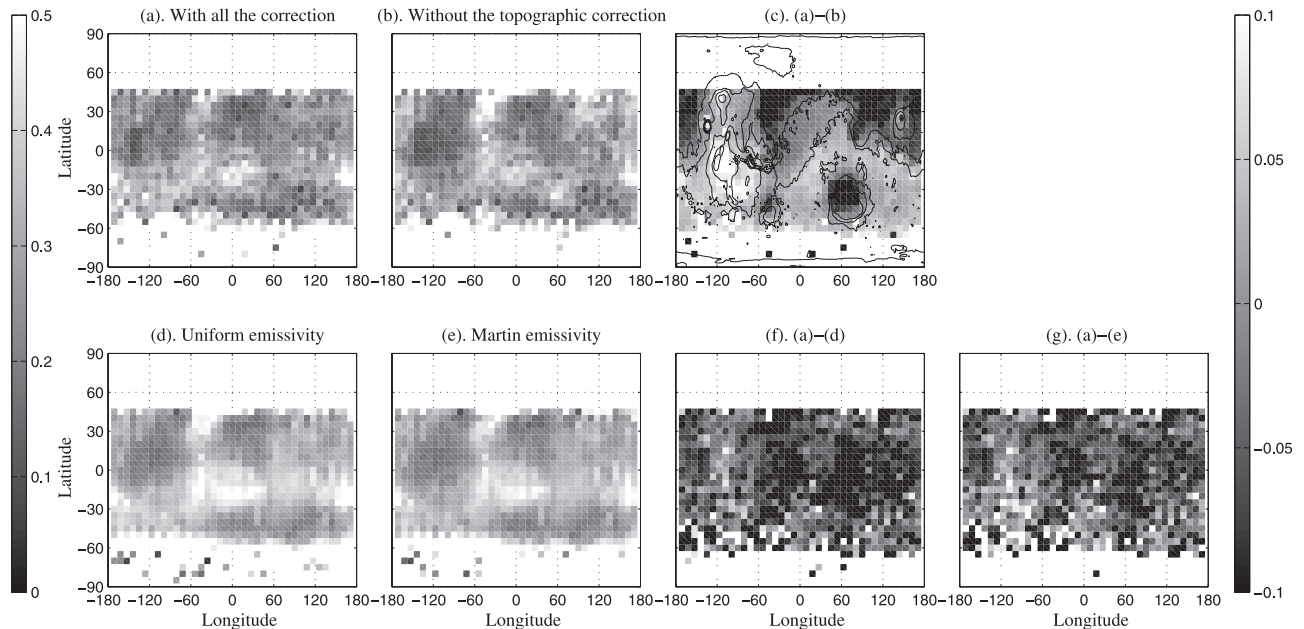
Figure 2. The dust opacity maps for $L_s = 225°−230°$. a) The column opacity normalized to the mean MOLA elevation. b) The retrieved dust opacity without the topographic correction. c) The difference between a) and b). d) The retrieved dust opacity with the uniform emissivity. e) The dust opacity generated with the original *Martin* [1986] scheme. f) The difference between a) and d). g) The difference between a) and e).

scheme was last used. These maps from *Christensen* [1998] were derived by finding the highest, brightness temperature in each bin of a gridded global map, and then deriving emissivity for the IRTM channels assuming that the channel with the highest brightness temperature possessed unit emissivity at that point on the planet. It was usually found that the *T7* channel had the highest emissivity, and thus the broadest effect of including the emissivity maps (relative to a uniform unit emissivity map) is to reduce the opacity. The effect of using the measured emissivities can be seen by comparing data from $L_s = 225°−230°$ in Figures 2a and 2d. Figure 2a shows opacity derived using measured emissivity, while in Figure 2d opacity is calculated assuming unit surface emissivity in both *T7* and *T9* channels. In both figures, the data have been topographically normalized. In general, the opacity is decreased by the correction for nonunit emissivity. However, there is also significant modification of the spatial opacity patterns as a result of using the measured emissivity. In particular, the part of the equatorial dust belt between 60°W and 120°W and 30°S to the equator is entirely due to a surface emissivity effect. The difference between Figures 2a and 2d is shown in Figure 2f. This figure correlates well with the pattern of 9-μm surface emissivity, but the influence is not completely direct, as the emissivity is also used in the retrieval to generate the near-surface temperature profile. For completeness, we also show the opacities generated with the original *Martin* [1986] scheme (Figure 2e) and the difference between this map and that generated with the measured emissivity (Figure 2g). Although the opacities are slightly lower than in the uniform emissivity case, the map is more similar to the uniform opacity case than the fully corrected case, suggesting that the emissivity formulation in the

original retrieval scheme does not do a particularly good job.

2.2.2.5. Effect of Correcting T15 on the Retrieval of Dust Opacity

[28] The dust opacity retrieval scheme [*Martin*, 1986] uses a profile of air temperature to define the dust emission temperature. This profile is constructed using a model of the surface temperature and the T15 values as a gauge of temperature at ∼25 km. As discussed above and in section 3, the (original) IRTM *T15* is biased to warm temperatures by an unaccounted for leakage of surface thermal emission. As such, it is necessary to assess the impact of *T15* correction upon the retrieval of 9-μm dust opacity. Zonal-mean dust opacity retrieved using corrected and uncorrected IRTM *T15* data show- that the effect of correction of *T15* generates a less than 10% effect (not shown). Cross correlation between these opacity values shows a highly linear trend with a slope of unity. In short, the correction of *T15* appears to have a minimal effect on the retrieved opacity. In any case, we proceed to use opacities derived with corrected IRTM *T15* values.

2.3. Water Ice Opacity: Adapting the *Martin* [1986] Scheme

[29] In order to provide a quantitatively consistent assessment of the cloudiness of the Martian atmosphere across the spacecraft record, we need a water ice retrieval scheme that works well for all available data sets. As IRTM represents the lowest spectral resolution system, methods that are appropriate for IRTM can be applied to TES and IRIS, but not necessarily vice versa.

[30] Previous methods for identifying water ice clouds with IRTM have focused on brightness temperature differ-

ences between $T11$ and $T20$ [*Christensen and Zurek*, 1984; *Christensen*, 1998; *Tamppari et al.*, 2000]. In the latter case, the effects of surface emissivity were explicitly treated (which can generate spectral brightness temperature contrasts that can be confused for clouds). However, these approaches do not generate opacity estimates. Specifically, the effects of the vertical temperature structure and of radiative transfer in the atmosphere are ignored. These effects make quantitative spatial and temporal comparison of "cloudiness" difficult with these earlier schemes. While it is true that in making estimates of the water ice opacity, one needs to make assumptions about the ice optical properties and the vertical distribution of the ice, additional information can be folded in from the simultaneous measurements of air temperature in the form of the $T15$ data. It is also worth noting that if we can fold in the air temperature data, the remaining ad hoc assumptions about particle size and vertical distribution are identical to and no more excessive than those that must be made in retrieving ice opacities at higher spectral resolution [e.g., *Pearl et al.*, 2001]. Here, we chose to adapt the *Martin* [1986] scheme to retrieve water ice opacity.

[31] The *Martin* [1986] scheme was originally developed to retrieve only dust opacity. However, fundamentally, the scheme is suited to extracting opacities for the generalized case of a two band radiometer system, where one band is located primarily in an extinction feature with another nearby channel located on a continuum. In principal, the Martin scheme can be adapted to retrieve other aerosol components where sufficient contrast and choice of channel spectral band passes allow it. To retrieve water ice opacity, we must first choose which channels to use.

[32] The error in the derived water ice opacities are related to the same causes as those for dust, as mentioned above and described by *Martin* [1986]. Thus the relative ice opacities are characterized by an error of <25%. However, there exists major uncertainty in particle size and vertical location of the cloud. This can be thought of as introducing a "systematic error" for the absolute water ice opacities. In this study, though, the absolute value of the opacity is not of major quantitative interest. Differences in opacity due to changes in cloud particle size and cloud deck height between years are as interesting a signature of interannual variability as that of atmospheric water ice abundance (which opacity is more typically taken to be a measure of).

2.3.1. Band Choice

[33] Figure 1 shows that the 11-μm channel of IRTM provides a good sampling of the 10–15 μm water ice extinction feature. We will use this channel as our "in band" (water ice sensitive) channel, as with the earlier IRTM ice cloud mapping studies. The choice of "continuum" is less clear. $T7$ and $T20$ in principal provide good continuum estimates. In fact, $T7$ provides a much better true continuum. Figure 1 shows that $T7$ remains the highest temperature regardless of whether dust or water ice is present in the atmosphere. In contrast, $T20$ is weakly affected by the long-wave trailing end of the 10–15-μm water ice feature, and is quite significantly affected by dust. However, it is this differential sensitivity to dust that makes $T20$ a better continuum choice for water ice opacity estimates than $T7$. Considering Figure 1, it is clear that if there is some dust in the atmosphere, $T11-T7$ will be strongly

negative, because the 8–12-μm silicate band provides significant extinction in the $T11$ channel. As this dust signal will be of the same sign as a water ice signal, and hence indistinguishable, this means makes $T11-T7$ a poor choice for isolating water ice. For $T11-T20$, the situation is quite different. If dust is in the atmosphere, $T20$ is more effected by dust than $T11$, generating a positive signal. This will have the opposite sign as a water ice signal, where the extinction in $T11$ exceeds that in $T20$. As such, dusty atmospheres can be excluded from retrieval by only attempting to retrieve ice opacity when $T11-T20$ is negative. In the case of positive $T11-T20$, we ascribe zero ice opacity. It can be argued that when dust and ice are both present in the atmosphere in significant quantity, our separate retrieval approaches will fail. This is true. A background haze of dust will result in underestimation of water ice opacity by acting to make the $T11-T20$ difference more positive. Fortunately, Mars cooperates in that dusty conditions tend not to be icy and vice versa. This is based on a variety of observations [*Toigo and Richardson*, 2000; *Clancy et al.*, 1996; *Smith et al.*, 2001a], although a problem does exist in deriving northern tropical dust opacities in northern summer (see section 5). As such, we proceed with separate retrievals of dust and water ice.

2.3.2. Surface Emissivity

[34] As with the dust opacity retrieval scheme, we incorporate the IRTM-band surface emissivity maps of *Christensen* [1998]. The importance of using measured surface emissivities was emphasized by *Tamppari et al.* [2000]. In that case, emissivities were used in a surface thermal model to generate "clear sky" $T11-T20$ maps as a function of season and local time. The difference between the measured $T11-T20$ and these "clear sky" values were used to diagnose the presence of water ice clouds. Modeling "clear sky" differences was important since using the measured $T11-T20$ alone would have resulted in false water ice cloud detections in regions with 11-μm surface emissivities lower than 20-μm surface emissivities. In our case, the measured emissivities are built into the retrieval scheme, and hence serve the same purpose of compensating for surface spectral contrasts. In addition, these emissivities are used to model the near surface air temperatures.

2.3.3. Water Ice Optical Properties

[35] We must choose optical properties for water ice particles in order to retrieve opacities. In this work, we use the real and imaginary indices of refraction from *Warren* [1984], and a modified gamma particle size distribution with an effective mean radius (r_{eff}) of 1.2 μm and a width of 0.2. The refractive indices are well known, but the particle size is a free parameter and one for which there is strong evidence for temporal and spatial variability. Unfortunately, the IRTM data are insufficient to allow retrieval of particle size information. Thus, to allow quantitative mapping, we chose a single particle size distribution and produced maps of water ice with the explicit understanding that the opacities relate only to that choice of distribution (i.e., the absolute values will change if the particle size distribution changes). Here, we examine the impact of our choice of particle size distribution on the retrieved ice opacities.

[36] The particle size and indices of refraction enter the retrieval through specification of scattering properties, which are calculated using Mie theory. The single scattering
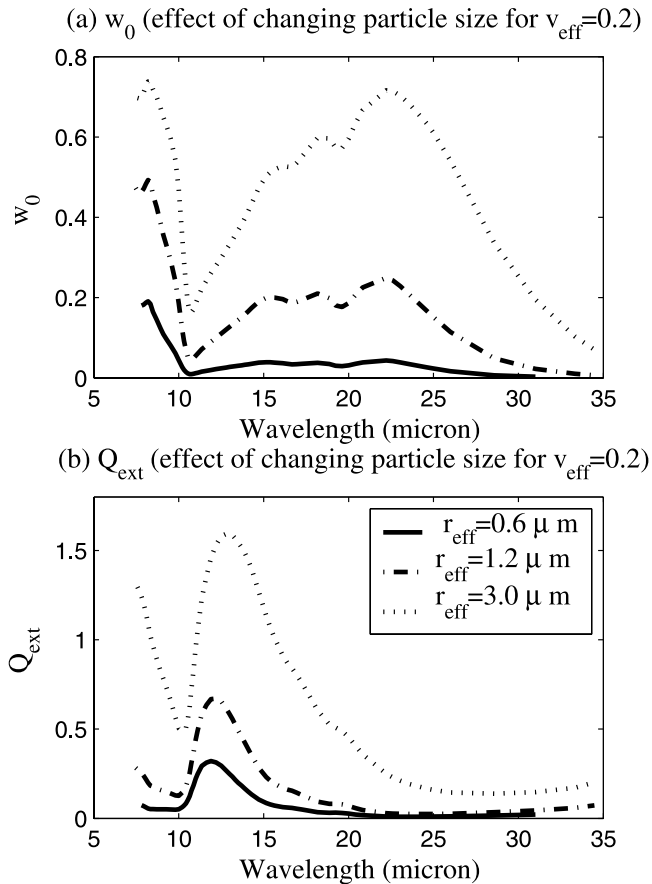
(a) w_0 (effect of changing particle size for v_{eff}=0.2)

(b) Q_{ext} (effect of changing particle size for v_{eff}=0.2)

Figure 3. The optical properties of water ice particles. a) Single scattering albedo for three different particle sizes (as indicated). b) The extinction coefficient corresponding to a).

albedo and the extinction coefficient are shown for choices of particle size in Figures 3a and 3b. The prominent rise in extinction parameter at $12-13$ μm is due to an ice absorption feature, demonstrated by a lack of an equivalent peak in the single scattering albedo. Three particle size distributions of the same width (ν_{eff} = 0.2) are shown for r_{eff} = 0.6 μm, 1.2 μm, and 3.0 μm (Figures 3a and 3b). Since these particle sizes are near the sharp transition in extinction efficiency as the size parameter crosses unity, there is a strong dependence of peak extinction efficiency on mean effective particle size [*Goody and Yung*, 1989]. This will lead to a roughly linear dependence of opacity on particle size (for representative particle size distributions).

[37] Figures 4a–4d show maps of cloud opacity for L_s = $100°-120°$ that were derived for the three particle size distributions used to construct Figure 3, and a size distribution of r_{eff} = 1.2 μm and ν_{eff} = 0.6. The spatial patterns of cloud and the local variations in cloud thickness are very similar between all four maps. The main effect is a scaling of opacity. This is better illustrated in Figures 4e and 4f, which show opacity derived assuming the standard size distribution (r_{eff} = 1.2 μm and ν_{eff} = 0.2) is plotted against opacity derived with the other particle size distributions. The trends are all essentially linear, with relations for mean particle size being: $\tau_{0.6} = 2 \times \tau_{1.2}$ and $\tau_{3.0} = 0.8 \times \tau_{1.2}$, while for variation in size variance the trend has a slope of unity.

2.3.4. Topographic Correction

[38] The code is capable of correcting the water ice opacities for air column depth in the same manner described for dust. However, it seems highly unlikely that water ice is distributed uniformly in the atmosphere [e.g., *Kahn*, 1984; *Jaquin et al.*, 1986; *Pearl et al.*, 2001]. Thus, as with *Pearl et al.* [2001] and *Smith et al.* [2001b], we do not present topographically corrected water ice opacities.

3. Air Temperature

[39] Air temperature is in some sense the most fundamental of the climate variables discussed in this paper. It is the variable most directly interpretable in terms of diabatic (mainly radiative) and adiabatic (dynamical) heating. It is also the variable most readily comparable with dynamical models. Unfortunately, the record of air temperature from the Viking IRTM instrument was evidently contaminated, making the extended, multispacecraft air temperature record the most tainted (relative to the dust and water ice records). On the basis of careful study of the tidal signatures in the Viking IRTM *T15*, *Wilson and Richardson* [2000] showed that IRTM *T15* diurnal temperature variations were unrealistically large and phased incorrectly (given a straightforward interpretation of the weighting function). They suggested that some small contribution of surface radiation was making its way into the *T15* channel detector that was not represented in the nominal spectral response function. Assuming that this radiation is of a wavelength well removed from the 15-μm CO_2 feature (otherwise it would appear as an atmospheric contribution, while the tidal analysis demonstrated that the extra radiance must have originated at the surface), they suggested a simple "correction" for *T15* which mixes radiance from the 20-μm channel into the 15-μm channel (accounting for the leak of surface radiation into the *T15* channel). A direct prediction of the *Wilson and Richardson* [2000] study is that while daytime IRTM *T15* values should be spuriously large compared to the actual air temperatures sampled by the weighting function shown in Figure 1, the nighttime measurements should be reasonably accurate. This is because at night, the surface temperatures are lower than those of the mid-level atmosphere, and thus surface emission leaking into the channel will have little effect on the measured temperatures.

[40] In this section, we critically examine the *Wilson and Richardson* [2000] "surface radiance leakage" hypothesis by comparing daytime and nighttime observations between TES and IRTM. We then proceed to examine the seasonal and interannual variations within each of and between the IRIS, IRTM and TES records.

3.1. Assessment of the Surface Radiance Leakage Hypothesis

[41] At the heart of the *Wilson and Richardson* [2000] hypothesis is the idea that observed IRTM daytime temperatures are biased to higher temperatures relative to nighttime observations. This is a consequence of the physical mechanism proposed for the defect in the IRTM *T15* channel, namely an out-of-band leakage of surface emission, which is very "bright" during the daytime. In turn, this mechanism was suggested because of the strong variance between the tidal signature of air temperatures demonstrated by IRTM
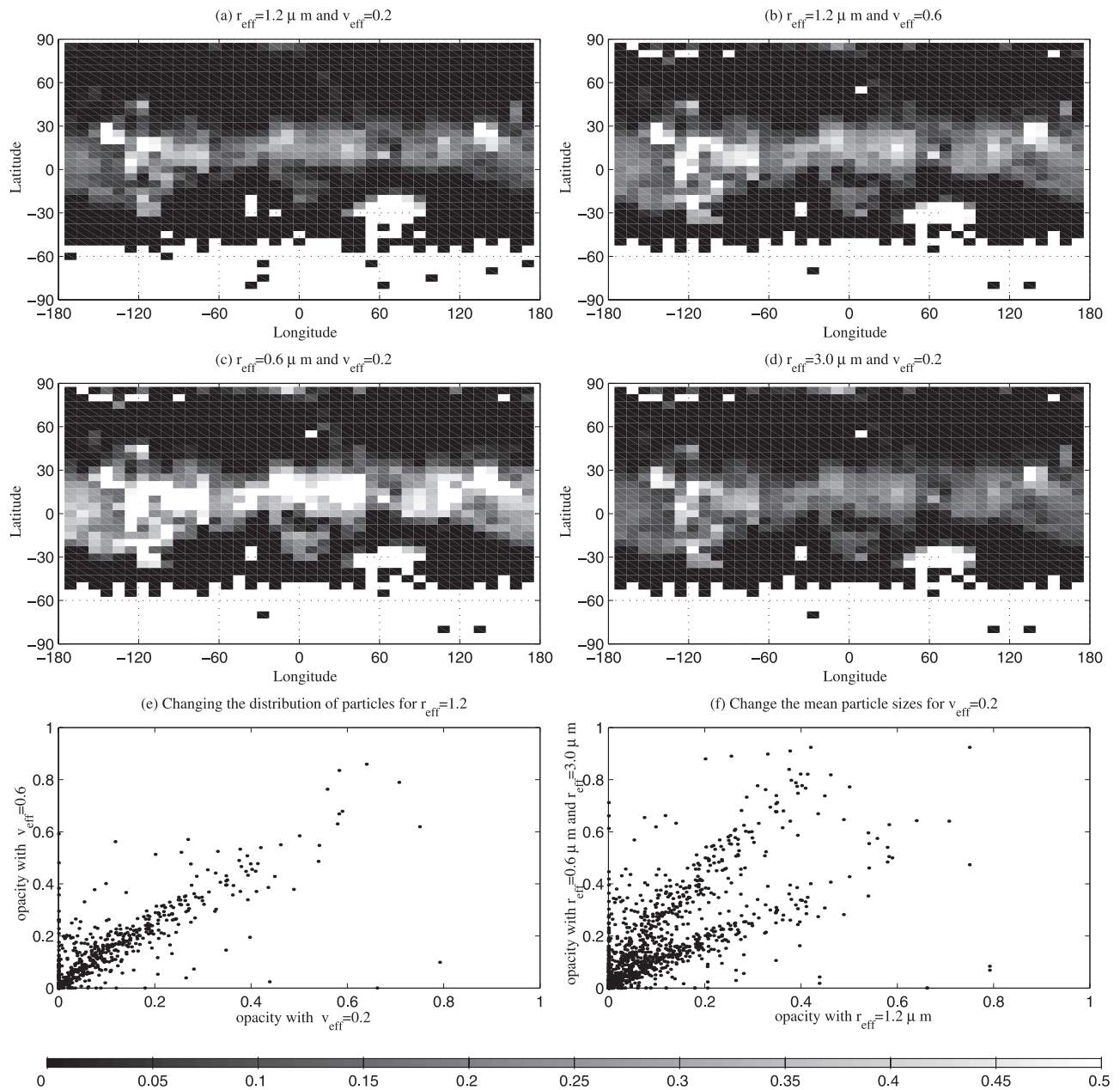
Figure 4. Water ice opacity maps for $L_s = 100°-120°$ derived using the different particle size distributions. Water ice opacity generated with a) $r_{eff} = 1.2$ μm, $\upsilon_{eff} = 0.2$, b) $r_{eff} = 1.2$ μm, $\upsilon_{eff} = 0.6$, c) $r_{eff} = 0.6$ μm, $\upsilon_{eff} = 0.2$, d) $r_{eff} = 3.0$ μm, $\upsilon_{eff} = 0.2$. e) The correlation between the opacity derived with $r_{eff} = 1.2$ μm, $\upsilon_{eff} = 0.6$ and the opacity derived with $r_{eff} = 1.2$ μm, $\upsilon_{eff} = 0.2$. f) The correlation between the opacity generated with $r_{eff} = 0.6$ μm, $r_{eff} = 3.0$ μm and $r_{eff} = 1.2$ μm with the same particle size distribution ($\upsilon_{eff} = 0.2$).

[*Martin*, 1981] and that consistent with basic tidal theory and GCMs [*Wilson and Richardson*, 2000].

[42] The leakage hypothesis states that the actual *T15* radiance (R_{15}) is composed of a mixture of the radiance within the measured spectral response function (R_{air}) and the radiance from the surface, for which we use the 20-μm channel radiance (R_{20}). As such, the radiance within the measured spectral response function can be defined as:

$$R_{air} = (1 + m)R_{15} - mR_{20}$$

where *m* is the "mixing parameter" controlling the amount of admitted surface emission. We use $m = 0.08$ based on comparison between the IRTM data and GCM predictions of tidal magnitudes, following *Wilson and Richardson* [2000]. The radiance is converted to temperature using a conversion function derived from laboratory calibration data for IRTM.

[43] To test this hypothesis, we compare the diurnal and spatial variation of observed and corrected IRTM temperature with that observed by MGS TES. Similar spatial tests against the much sparser Mariner 9 IRIS were also shown by *Wilson and Richardson* [2000].
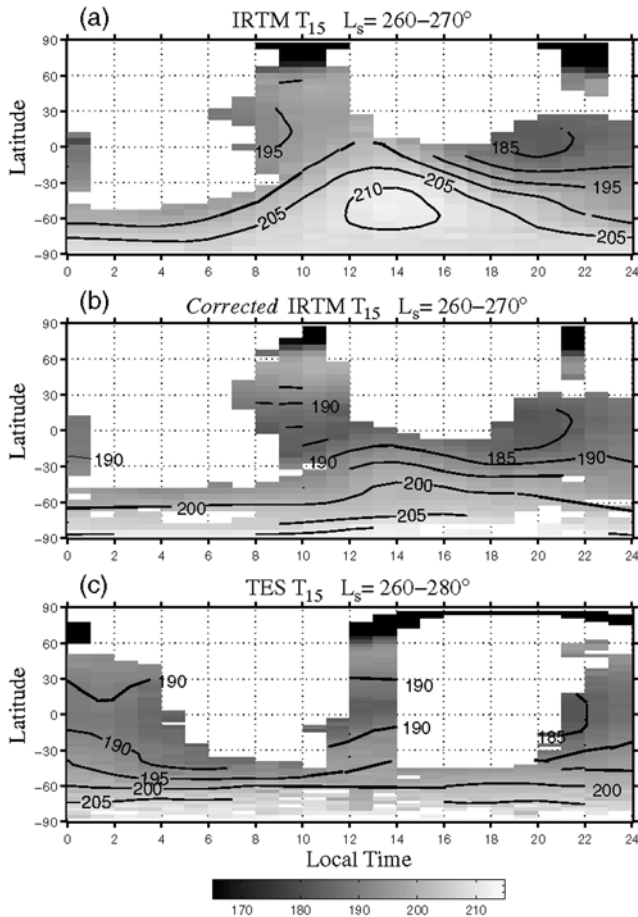
Figure 5. Diurnal variation of IRTM and TES *T15* as a function of latitude for SH solstice. Data has been binned at intervals of 1 hour in local time and 5 degrees in latitude. a) Original IRTM *T15* variation which shows the prominent effect of midday surface temperature bias. b) Corrected *T15* diurnal variation as discussed in the text. c) Diurnal variation of TES *T15* obtained during the Science Phase orbits. Note the absence of a midday temperature maximum in the TES data, which is in close correspondence with the corrected IRTM data.

[44] The diurnal coverage of MGS TES during the aerobraking and science phasing orbits was more extensive than the twice daily observation obtained when MGS attained mapping orbit, and thus a better range of local times can be used for comparison with the IRTM observations. Figure 5a shows IRMT T15 as a function of local solar time and latitude for a relatively clear period near summer solstice in the southern hemisphere. This season was selected as there is corresponding TES data There is a prominent region of high temperature in the region of the midday subsolar point that is highly correlated with the maximum of surface temperature. As argued by *Wilson and Richardson* [2000], this contribution is readily distinguished from the expected diurnal variation of midlevel (0.5 mbar) atmospheric temperature. Figure 5b shows the estimated true atmospheric temperature variation resulting from the correction procedure described above. The resulting temperature variation suggests the presence of a semidiurnal

thermal tide in the tropics that, according to GCM simulations, is consistent with the observed semidiurnal surface pressure variation observed at the Viking lander 1 site. Figure 5c shows the diurnal temperature variation in TES T15 for the comparable season. There is a very close correspondence in pattern with the corrected IRTM T15 field. In particular, there is no indication of the strong midday temperature maximum seen in the original IRTM data. The early morning temperatures are quite comparable. It is a general result that TES tropical 2 pm T15 temperatures are consistently warmer than the 2 am temperatures. This is a consequence of the phase variation with height of the vertically propagating diurnal tide prominent in the tropics. This signature is well-illustrated in zonally averaged temperature fields of *Banfield et al.* [2002].

[45] Figure 6 shows data comparisons between IRTM and TES *T15* at two seasons ($L_s = 20°-30°$ and $L_s = 80°-95°$) and at two local times ($0000-0400$ LT and $1200-1600$ LT, which we will refer to as "2 am" and "2 pm", respectively) as a function of latitude and longitude. Although the IRTM data are somewhat sparse, consistent geographical structures can be seen between the TES and IRTM T15 data at 2 am for $L_s = 20°-30°$ (Figures 6a and 6b). These geographic temperature variations represent quasi-stationary structures in the atmosphere of dynamical origin (i.e., stationary waves and nonmigrating thermal tides) [*Wilson*, 2000; *Banfield et al.*, 2002]. The resilience is explained in two ways. First, the wave dynamics generating these structures depend upon the background wind structure and the radiative heating, all of which are rather similar at the same season in any given year, all else being equal. Second, we have selected the data to minimize interannual variations in forcing by choosing data in northern spring and summer which appears to be the least dusty and most repeatable of seasons [*Richardson*, 1998]. The similarity between the TES and IRTM data at $L_s = 20°-30°$ and 2 am extends beyond spatial similarities. The differences are shown in Figure 6d. For given points in the binned data, differences are generally within $1-2$ K. Averaging across these binned data on a point-by-point basis shows that the two data sets agree to within 1 K. At least from the perspective of 2 am *T15*, TES, and IRTM report indistinguishable global-mean temperatures and geographical temperature structures.

[46] Figure 6c shows corrected IRTM *T15* for the same period. These "corrected" *T15* are very similar to the uncorrected IRTM *T15* and the TES *T15*, as shown in the difference plot (Figure 6e). Averaging over these binned differences shows that the corrected IRTM and TES *T15* are identical to within 1.4 K, thus the "correction" does not significantly affect the nighttime temperatures.

[47] The daytime temperatures from IRTM and TES are shown in Figures 6f and 6g for $L_s = 20°-30°$. The IRTM data are very sparse and biased to high latitudes. However, it is clear that the original IRTM *T15* are significantly warmer. Averaging over the difference plot (Figure 6i) results in a net difference of 12.4 K. The corrected IRTM *T15* are shown in Figure 6h. The corrected data are much more similar to the TES *T15*. Averaging over the difference map (Figure 6j) shows that the corrected IRTM *T15* is within 0.7 K of the TES T15.

[48] Late northern spring data ($L_s = 80°-95°$) are shown in Figures 6k–6t. Again, the nighttime temperatures
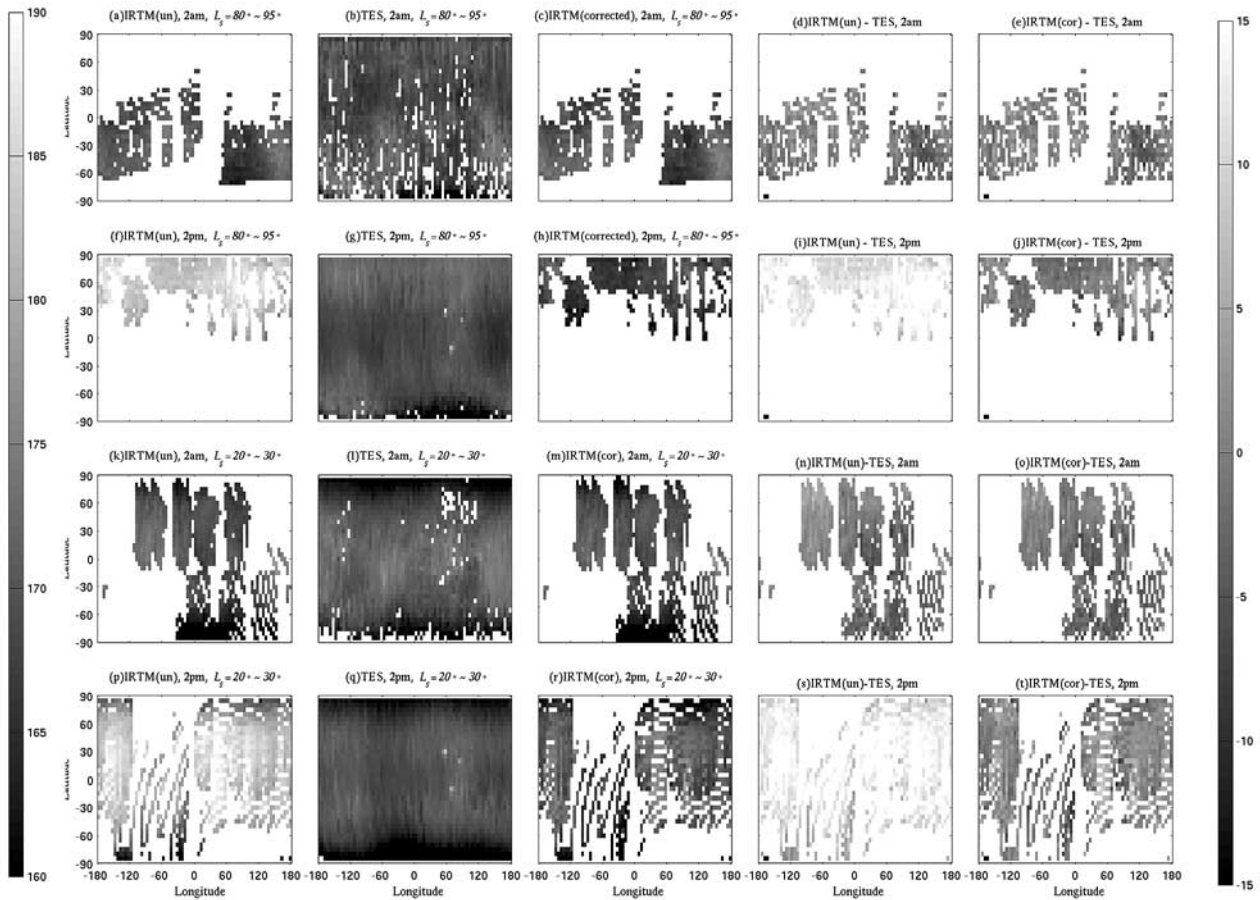
Figure 6. Day-night IRTM and TES *T15* comparisons illustrating the leakage of surface emission into the IRTM *T15* channel. The first three columns on each row show uncorrected IRTM, TES, and corrected IRTM data, respectively, displayed as a function of latitude and longitude. The data are binned by 5° of latitude and 5° of longitude. The two final columns in each row show differences between uncorrected IRTM and TES data, and corrected IRTM and TES, respectively. Data are shown for 2 am and 2 pm, and for $L_s = 80°-95°$ and $L_s = 20°-30°$.

(Figures 6k–6m) are very similar to each other in value and geographical structure. Averaging over difference maps (Figures 6n and 6o) shows differences of only 0.47 K and 0.24 K between TES and original IRTM, and between TES and corrected IRTM, respectively. The coverage in the daytime data is much better than at the earlier season described above. Nevertheless, the original IRTM daytime temperatures are again significantly warmer (average offset of 11.6 K) that the TES *T15* (Figures 6p and 6q). With correction, the temperatures become much more consistent, showing an average difference of only 1.1 K.

[49] These analyses provide a simple test of the correction procedure and the leakage hypothesis. However, by itself, this test would prove very little. What constrains daytime temperatures to agree across the spacecraft record? It is important to remember that the leakage hypothesis resulted from a study of tidal dynamics, and the correction and mixing parameters were chosen only to bring the diurnal variation of IRTM *T15* data into agreement with tidal theory and models. It is significant to note that nighttime temperatures from IRTM (corrected and uncorrected) agree very well with TES. This suggests that either the processes controlling nighttime temperatures in these two years were identical or it possessed

differences that exactly cancelled. However, given the similarity in dust opacities at these seasons (section 4), we know that the forcing was very similar. An important additional constraint on the system is that the temperature structure is related to forcing by the dynamical and thermal equations that govern atmospheric motions. These equations greatly limit the range of states that the atmosphere can inhabit. These equations are represented in GCMs and in a range of simplified models. It is the application of these constraints, and the observed similarity in forcing which allows us to rule out the uncorrected IRTM *T15* observations with certainty. We therefore claim that the leakage hypothesis and correction defined by *Wilson and Richardson* [2000] have been successfully tested. We will proceed to use IRTM data in their corrected form, and wherever possible, only the nighttime values (as we do recognize that the correct IRTM daytime temperatures may still have some uncertainty) to examine interannual variability of air temperature.

3.2. Seasonal Cycle of Global-Mean Temperatures

[50] In this section, we will describe the seasonal cycle of air temperature that is represented in the infrared spacecraft record. While the seasonal cycle has been examined and
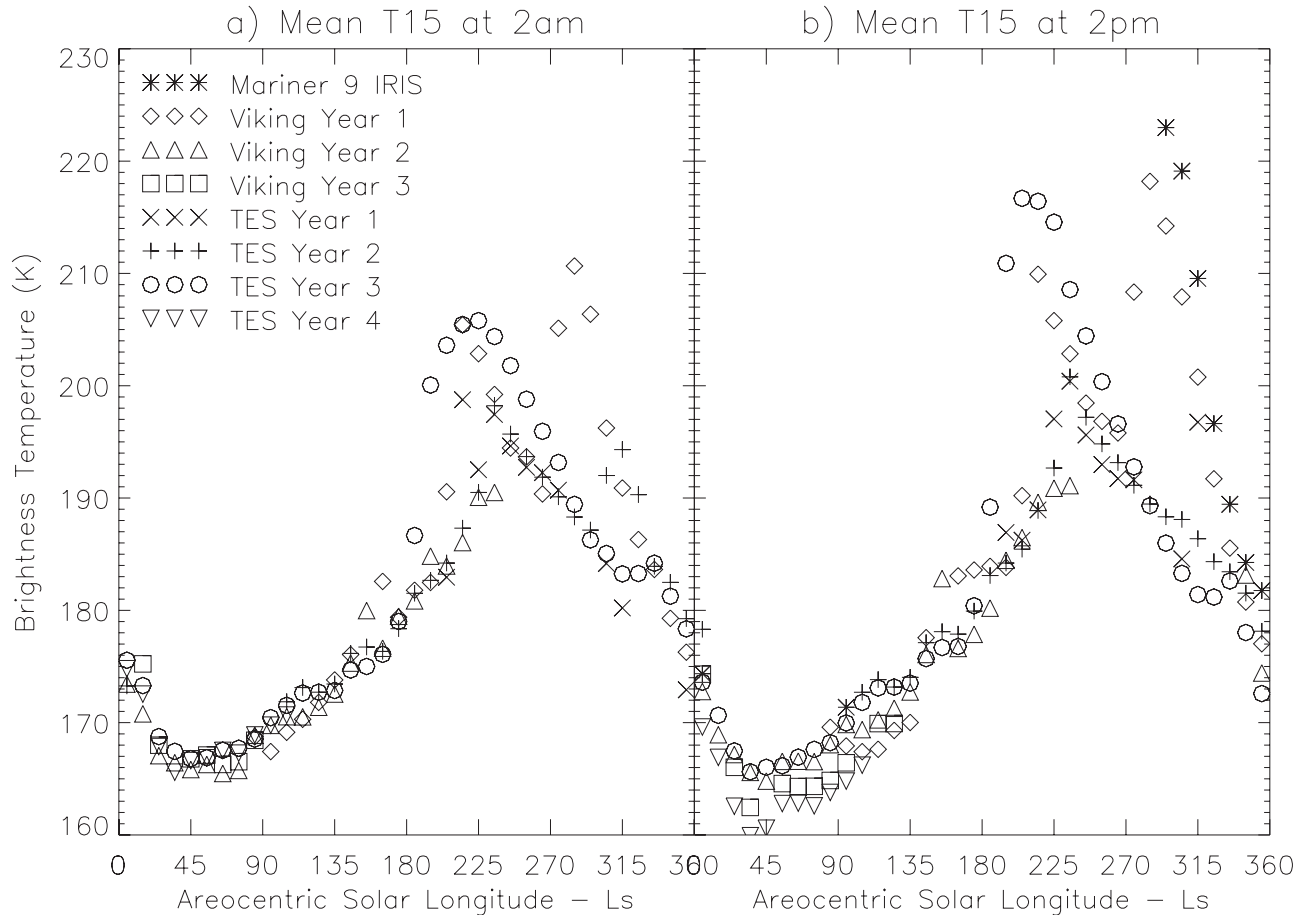
Figure 7. The seasonal evolution of global mean T15 atmospheric temperatures. Effective tropical- and midlatitude-mean air temperatures are shown for all longitudes and latitudes between 60°N and 60°S. The data have been binned by 10° of L_s. The production of values for spacecraft years other than TES year 2 are discussed in the text. Temperatures are shown for a) 2 am and b) 2 pm.

described before [*Martin*, 1981; *Leovy*, 1985; *Clancy et al.*, 1990, 1996, 2000; *Richardson*, 1998; *Conrath et al.*, 2000; *Wilson and Richardson*, 2000; *Smith et al.*, 2001a], previous efforts have been hindered by heterogeneity in the observations that limit confidence in the representativeness of the cycles presented. Here, we take special care to produce the most homogeneous data set possible.

[51] Figure 7 shows air temperatures "averaged" over 10° of L_s, 5° of latitude and longitude, and for local times between midnight and 4 am (Figure 7a) and noon and 4 pm (Figure 7b). The data are not direct averages but are constructed in the following way. A reference annual cycle is constructed from the TES *T15*, for which there is excellent coverage. We make latitude and longitude maps of the TES data between 60°S and 60°N, and at 5° latitudinal and longitudinal resolution. These maps are essentially completely populated by the TES data for the full Martian year beginning with the commencement of the mapping mission (for our purposes, $L_s = 115°$ in TES year 2), except for the $L_s = 10°-20°$ bin, which is poorly filled due to solar conjunction. An average over the populated bins is made, which forms a reference "global mean" temperature curve as a function of L_s. We do this for both nighttime and daytime data. For all other data (pre-mapping and later mapping mission TES, IRTM, and IRIS), we construct

similar maps of 0−4 am and 12−4 pm data, which may be substantially less well populated than the mapping mission data. By doing a point-by-point difference between these maps and the nearly fully-populated TES *T15* maps, we establish an offset between each data set and the TES reference for each L_s bin. Seasonal records for each of the nonmapping mission TES data are constructed by adding these offsets to the TES average values. This method is used because it guarantees the minimum possible biasing of latitudinal, longitudinal, and local time coverage into erroneous interannual and interinstrument differences.

[52] Nighttime temperatures from IRTM should be more reliable than daytime temperatures for the reasons discussed in section 3.1. These temperatures are shown in Figure 7a. The nighttime curve shows minimum temperatures of 166 K ± 1 K, occurring from $L_s = 45°-70°$. Data from two Viking (2 and 3) and two TES (3 and 4) years are shown in this season. The very high degree of repeatability is remarkable. In particular, the two TES years (for which the highest data volume is available) show a difference in mean temperature of substantially less than 0.5 K. The daytime data are more puzzling at this season. While the Viking year 2 and TES year 3 data agree very well, the Viking year 3 and TES year 4 are substantially lower. Low data volume and the effects of correction can be invoked to dismiss the Viking

year 3 data, but the TES year 4 data have high volume and correction is not an issue. TES year 4 daytime data are consistently 3–5 K cooler than those of the TES year 3 data. The difference only in daytime temperatures is an interesting puzzle that needs further examination. If the differences between TES year 3 and 4 are real, rather than instrumental, the fact that the years with cooler daytime temperatures follow the occurrence of planet-encircling (global) dust storms may be of significance.

[53] The temperatures steadily increase from the minimum at $L_s = 45°–70°$ until about $L_s = 140°$. After this point, temperatures become more variable from year-to-year as they become influenced by large transients associated with dust storms. *Wilson and Richardson* [2000] pointed out a distinct jump in air temperatures just before $L_s = 150°$ in Viking years 1 and 2. These steps can be seen in Figure 7a as steps of roughly 5 K. However, the signal here is somewhat muted compared to the presentation by *Wilson and Richardson* [2000] due to the more rigorous averaging technique used here. Figure 7 shows that the air temperature cycle is highly repeatable throughout northern spring and summer. It also shows that the globally integrated and time-averaged temperatures are very steady; there is essentially no globally integrated, very short-term (few tens of days) variability or transience. Telescopic microwave observations [*Clancy et al.*, 2000] follow the broad outline of the spacecraft data but an exact comparison is compromised by the disk average nature of the microwave observations. *Haberle et al.* [1999] discuss some aspects of this. In addition, there is some variability in the sub-Earth latitude and local time of day in the microwave observations. In any case, the short-term variability in the microwave record [*Clancy et al.*, 2000] most likely represents uncertainty in the observation, rather than being an intrinsic property of the atmosphere in the aphelion season.

[54] It is interesting that a distinct peak in air temperatures occurs at about $L_s = 235°–240°$. This "peak" (at about 195 K) is during the southern spring dust storms that are observed to occur in each of the years observed by spacecraft. The peak doesn't represent the true peak for all years observed. For example, in Viking year 1, air temperatures pass through this "peak" value as they fall from their 1977a dust storm maximum of 205 K at $L_s = 210°$. However, there are no years observed for which temperatures are lower than this "peak" value at $L_s = 235°–240°$. This is consistent with the dust opacity observations (section 4) that show dust events at this season in all years observed. *Richardson* [1998] proposed that the annual cycle of air temperatures could be thought of as being composed of a repeatable "background" cycle of air temperature (maintained, presumably, by a mixture of the eccentricity cycle and feedbacks involving dust lifting), with transient storm events superposed that generate large and variable spikes. This view is now somewhat hard to reconcile with the observations in that the cycle "peak" defined here is generated by storm activity. Does a storm happen every year at this season such that these events can be folded into a repeatable annual cycle? More observations are required to provide a definitive answer.

[55] After the southern spring maximum (defined by the curve of minimum temperatures for a given L_s, which also happens to be the curve populated by the largest number of overlapping measurements from different years), temperatures generally decline, but do include very large excursions to higher temperatures associated with the 1977b and Mariner 9 dust storms. By $L_s = 0°$, temperatures return to highly repeatable values. While the cycle definitely appears to have one minimum and one maximum (but may be biased by an unrepresentative dust storm features in all years observed?), the annual cycle is skewed such that the transition from maximum to minimum is more rapid (less than 170° of L_s from $L_s = 240°–50°$) than the rise from minimum to maximum (more than 190°). The presence of the storm season maximum at $L_s = 235°–240°$ gives the maximum a sharply defined peak, rather than the soft curve of the northern spring minimum. Apart from episodic dust storm activity, the annual temperature variation has strong annual and semi-annual harmonics, with the annual harmonic related to the variation of insolation due to eccentricity (with aphelion just after $L_s = 70°$) and the semi-annual component related to the variation in solstitial-to-equinoctial pattern of heating. Variability is less than ±2.5 K from $L_s = 0°$ to after $L_s = 180°$, with the exception of two IRTM data points (one from each of year 1 and year 2). For southern spring and summer it makes little (if any) sense to talk about interannual variability of climate as the variance is so dominated by transient storm systems. Many more years will need to be sampled before meaningful statistics on this season can be developed. Although uncertainty exists due to the extent of sampling, which stands at 5 Martian years, it would seem that a very clear minimum temperature curve can be defined for this season, and that storms can generate upward excursions of at least 30 K.

[56] On the basis of the nighttime air temperature data, every northern spring and early northern summer yet observed were identical to within the level of experimental error (to within ±1 K). This result stands irrespective of the IRTM *T15* "leakage" since the nighttime temperatures are essentially unaffected by this instrumental defect, as discussed in section 3.1 and by *Wilson and Richardson* [2000]. This result is consistent with the suggestion of repeatability during this season first introduced by *Richardson* [1998], but places much tighter constraints on the amount of interannual variability than any previous study. The daytime data, however, suggest a somewhat different story, with temperatures varying from year-to-year by up to 6 K in this season. This day-night discrepancy is unexpected and not understood. However, it is interesting to note that the years with cooler daytime temperatures are those that follow years with global dust storms. Whatever is going on, it is not the direct response one would expect for prolonged fall-out of dust following a major storm, or for enhanced dust lifting associated with global dust storms placing surface dust in more readily erodable locations. In any case, despite the discrepancy, the growing evidence for interannual repeatability (be it at levels of <1 K or <6 K) of the northern spring and summer season does raise a problem for the interpretation of lander entry profile observations. Three such profiles exist from Viking Landers 1 ($L_s = 98°$, 4:13 pm, 22.3°N, 48.2°W) and 2 ($L_s = 117°$, 9:06 am, 47.6°N, 229.5°W), and Mars Pathfinder ($L_s = 142°$, 3:00 am, 19.3°N, 33.6°W). The only leverage we have in this study for comparison with these profiles is the fact that the *T15* weighting function can

be applied to each profile, and the resulting IRTM-like "observation" compared to IRTM and TES data. When this is done, the *T15* values generated are: 181.8 K (VL1), 178.7 K (VL2), and 182.4 K (MPF). These measurements are for different seasons, locations, and local times, so direct intercomparison would be extremely ill-advised and would likely lead to false conclusions. Instead, the various orbiter data sets (which have all been shown to agree after "correction" of IRTM) can be searched for coincident observations in latitude, longitude, local time, and season. By restricting the search to 5° in latitude, 10° in longitude, 1 hour in local time, and 4° of L_s, we find that all landing sites have multiple available observations, but that only VL1 is observed in more than one year. IRTM observations of the VL1 site from Viking year 1 produce an average *T15* of 164.5 ± 4 K from 12 observations. TES observations of the VL1 site from TES year 3 produce *T15* = 167.9 ± 2 K from 356 observations. IRTM observations of the VL2 site from Viking year 1 have *T15* = 163 ± 3 K from 47 observations. TES observations of the MPF site from TES year 2 have *T15* = 173.2 ± 4 K from 29 observations. In each case, the spacecraft infrared observations are 10–20 K lower than the entry profiles. We have no explanation for this, but suggest that the agreement between essentially all other observational data sets suggest that the entry profile data may be biased warm.

3.3. Seasonal and Latitudinal Evolution of Air Temperatures

[57] Zonal-mean *T15* data from all three infrared instruments are shown in Figure 8. These average data are binned by 5° of latitude and 5° of L_s. All available longitudes and local times are averaged together without weighting. These observations can be compared with the annual cycles of IRTM observations presented by *Martin* [1981] and *Wilson and Richardson* [2000], and of TES observations presented by *Smith et al.* [2001a]. We do not treat the binning of these data with as much precision as the global-mean data as we do not subject them to the same rigorous quantitative analysis. It is, however, worth noting that the averaging of dayside and nightside data leads to a bias that is most prominent during dust storm periods. For example, the MGS 2 am–2 pm orbit leads to high-biased tropical air temperatures as the semidiurnal tide has maxima at 3 am and 3 pm [*Wilson and Richardson*, 2000]. Since precise measurement of temperatures during dust storms is not a major focus of this paper, and the separated daytime and nighttime temperatures have been shown in Figure 7, we proceed to examine the diurnally averaged temperature products.

[58] In the tropics and midlatitudes, the zonal-mean data reflect the global-mean trends described in section 3.2. In the polar regions, the trends are much more strongly controlled by the local season, with local winter containing the minimum temperature. The transition from the global-mean temperature cycle to the locally controlled cycle occurs near 60°, with the latitude being lower in the south and higher in the north. Each of the solstice seasons exhibits strong evidence for the Hadley circulation, as discussed by *Wilson and Richardson* [2000]. The signature of this circulation is especially evident during the various dust storm events in southern spring and summer. Elevated temperatures in the summer hemisphere reflect enhanced heating

associated with the absorption of solar radiation by dust. At these times, a corresponding temperature maximum exists in the winter hemisphere associated with adiabatic heating in the Hadley cell down-welling branch. The strongest of these patterns is evident in the southern summer of Viking year 1 associated with the 1977b planet-encircling dust storm (the IRIS storm likely generated an even stronger pattern, but the IRIS observations are unfortunately biased to the southern latitudes). During the 1977b event, this adiabatic heating is sufficient to elevate polar winter temperatures well above the CO_2 condensation profile, resulting in a "polar warming" event [*Jakosky and Martin*, 1987; *Wilson*, 1997; *Forget et al.*, 1999]. While less dramatic, the signature of the Hadley circulation is equally evident in the northern spring and summer, with distinct minima in temperatures occurring at the equator in between the two maxima, consistent with theory and models of the Hadley circulation [e.g., *Schneider*, 1983; *Haberle et al.*, 1982; *Wilson*, 1997]. Using corrected data, the patterns of air temperature in all of the data sets in northern spring and summer are exceedingly consistent. It should be noted that the main perturbation signatures in the *T15* data sets are associated with dust storm events (the events at $L_s = 205°$ and $L_s = 274°$ in Viking year 1 and at $L_s = 225°$ in TES years 1 and 2; see section 4.).

4. Dust Opacity

[59] Dust has a major effect on the Martian atmosphere through its modification of radiative heating rates. As such, the thermal state of the atmosphere and the general circulation is closely related to the behavior of dust. The largest perturbations in the air temperature record discussed in section 3 are due to dust storms. These dynamical phenomena remain poorly understood despite their observation in the Martian atmosphere for over a hundred years. In this section, we examine the seasonal cycle of "background" dustiness, specifically focusing on the degree of year-to-year variability as a function of season. We also examine the dust storm events contained in the IRIS, IRTM, and TES records.

4.1. Comparison With the MOC Images and the TES Team Retrievals

[60] The dust opacity retrieval scheme used in this study has a long heritage, and has been improved through inclusion of measured surface emissivity (see section 2). The quality of the scheme can be assessed by comparing opacity maps generated with this scheme against those derived by spectral signature matching (as done by the TES team [*Smith et al.*, 2000]), and by comparing them against MOC images (Figure 9). We have chosen a period with strong spatial variability in dust for this comparison, in order to demonstrate the ability of the infrared schemes to "map" dust in a manner consistent with the images. The specific season is $L_s = 225°–230°$, during which images show the obvious signature of dust storms, generated in the northern winter baroclinic storm zone, being "flushed" across the equator in the low-level branch of the Hadley circulation (see *Cantor et al.* [2001] and section 4.3 for visible and thermal infrared observations of this phenomena).
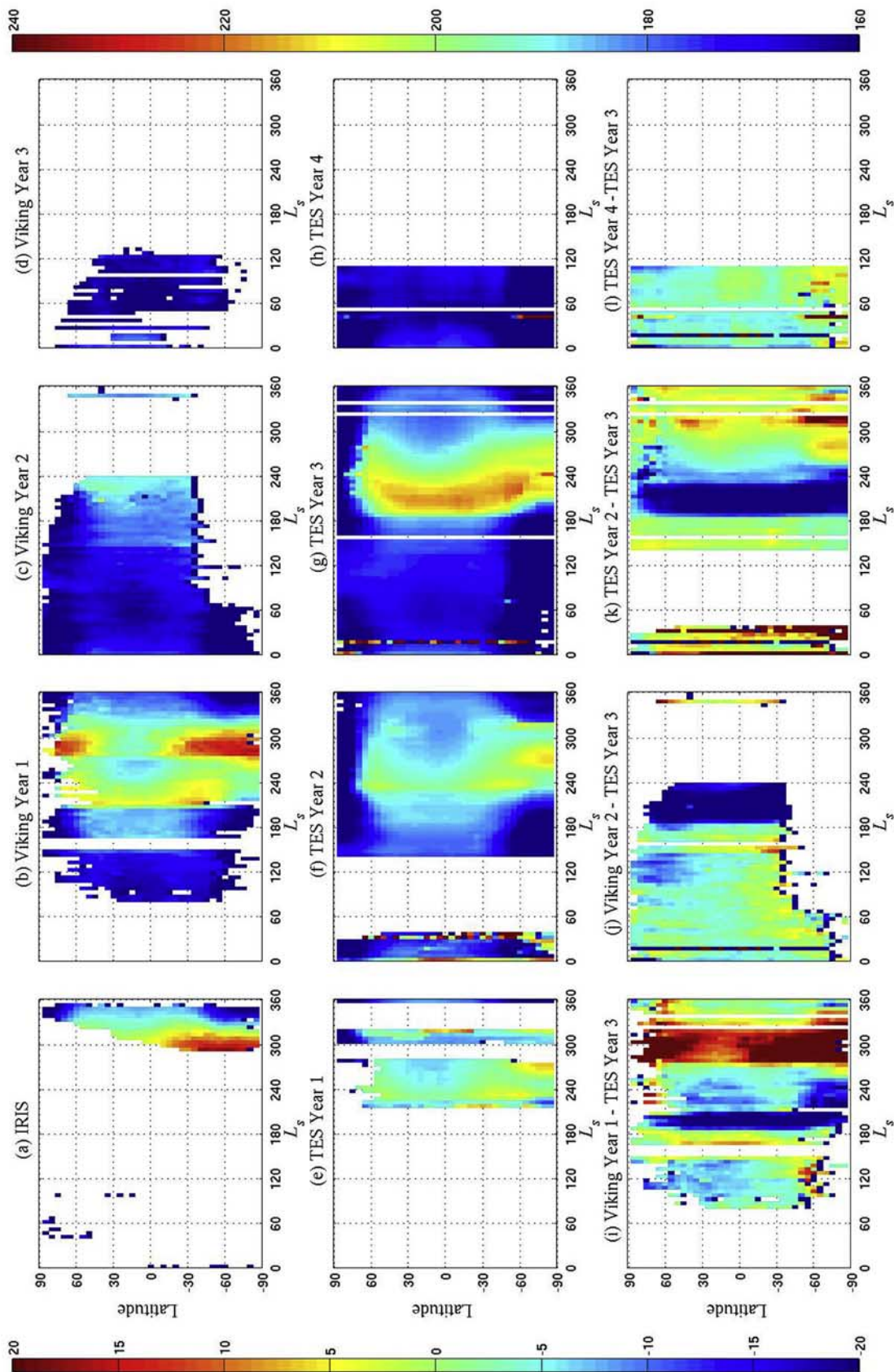
Figure 8. Zonal mean *T15* as a function of latitude and L_s. The data are binned by 5° of latitude and 5° of L_s. All available longitudes and local times are averaged together without weighting. Data are shown for a) IRIS, b) Viking Year 1, c) Viking Year 2, d) Viking Year 3, e) TES year 1, f) TES year 2, g) TES year 3, h) TES year 4. i)–l) Differences between various years. Note the color bar for a)–h) is on the right, while the color bar for i)–l) is on the left.
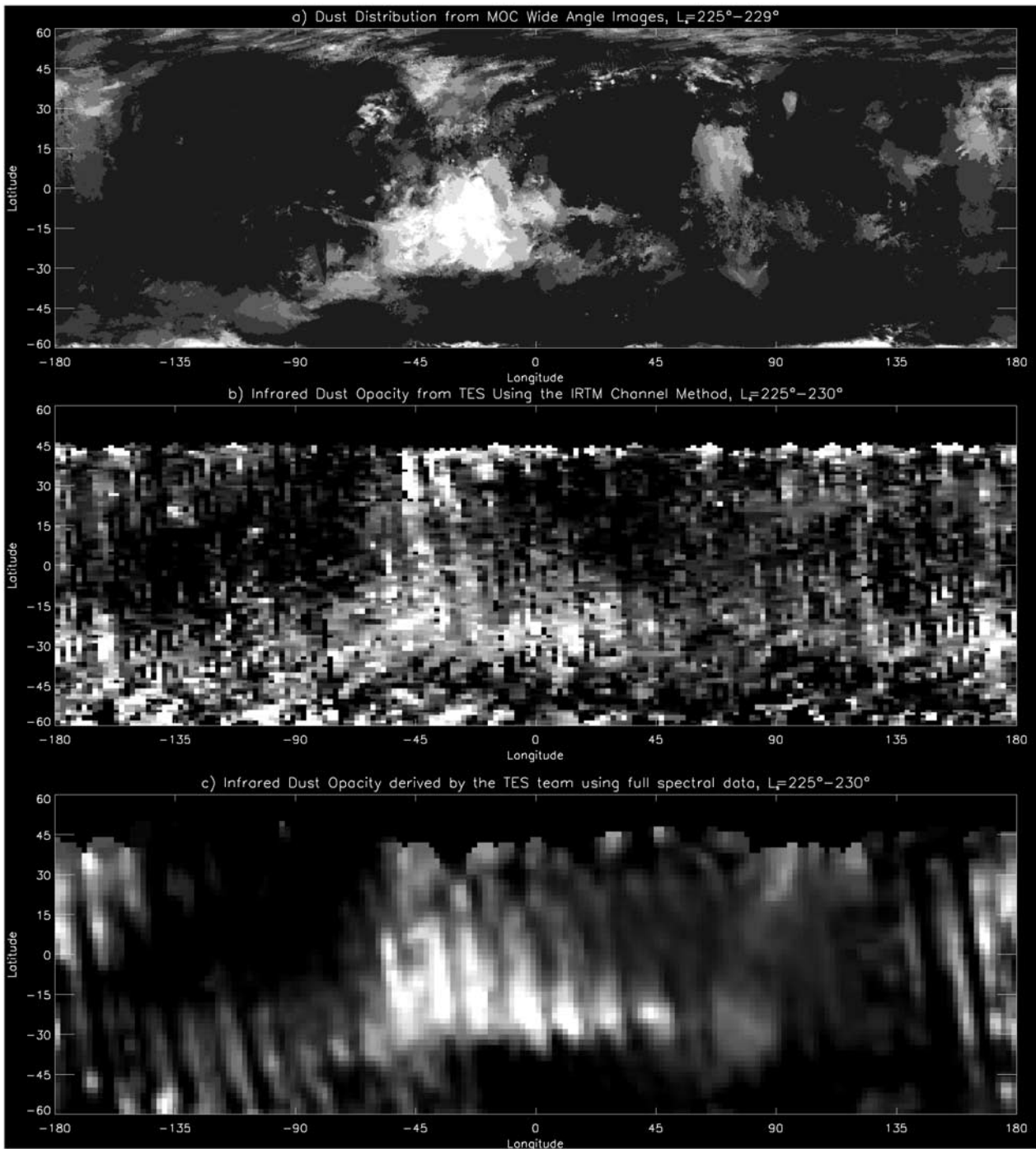
Figure 9. Dust in the Martian atmosphere for $L_s = 225° - 230°$ from TES Year 2. a) Dust as identified using the Mars Orbiter Camera Wide-angle color imager (H. Wang, personal communication, 2002). b) 9-μm dust opacity using the IRTM scheme discussed in this paper. c) Infrared dust opacity retrieved by the TES-team (M. Smith, personal communication, 2002). Both sets of infrared data have been topographically corrected.

[61] Figure 9a is derived from the MOC WA red images, using threshold criteria for the presence of dust [*Wang and Ingersoll*, 2002]. Figure 9b shows 9-μm opacity maps based on the difference between the IRTM 9 and 7 μm channels. Figure 9c shows dust opacity as derived by the TES team [*Smith et al.*, 2000]. Several major features exist in these dust maps. A large concentration of dust is observed between 10°S and 30°S, and 50°W and 40°E. This is the accumulation region for dust flushed across the equator. Mildly elevated opacities can be seen along the entire length of the belt at roughly 30°S. Elevated opacity can also be seen in the dust source region in Acidalia Planitia (40°N, 40°W). A secondary region of cross-equatorial transport can be seen at 180° longitude. The diffuse dust haze at this
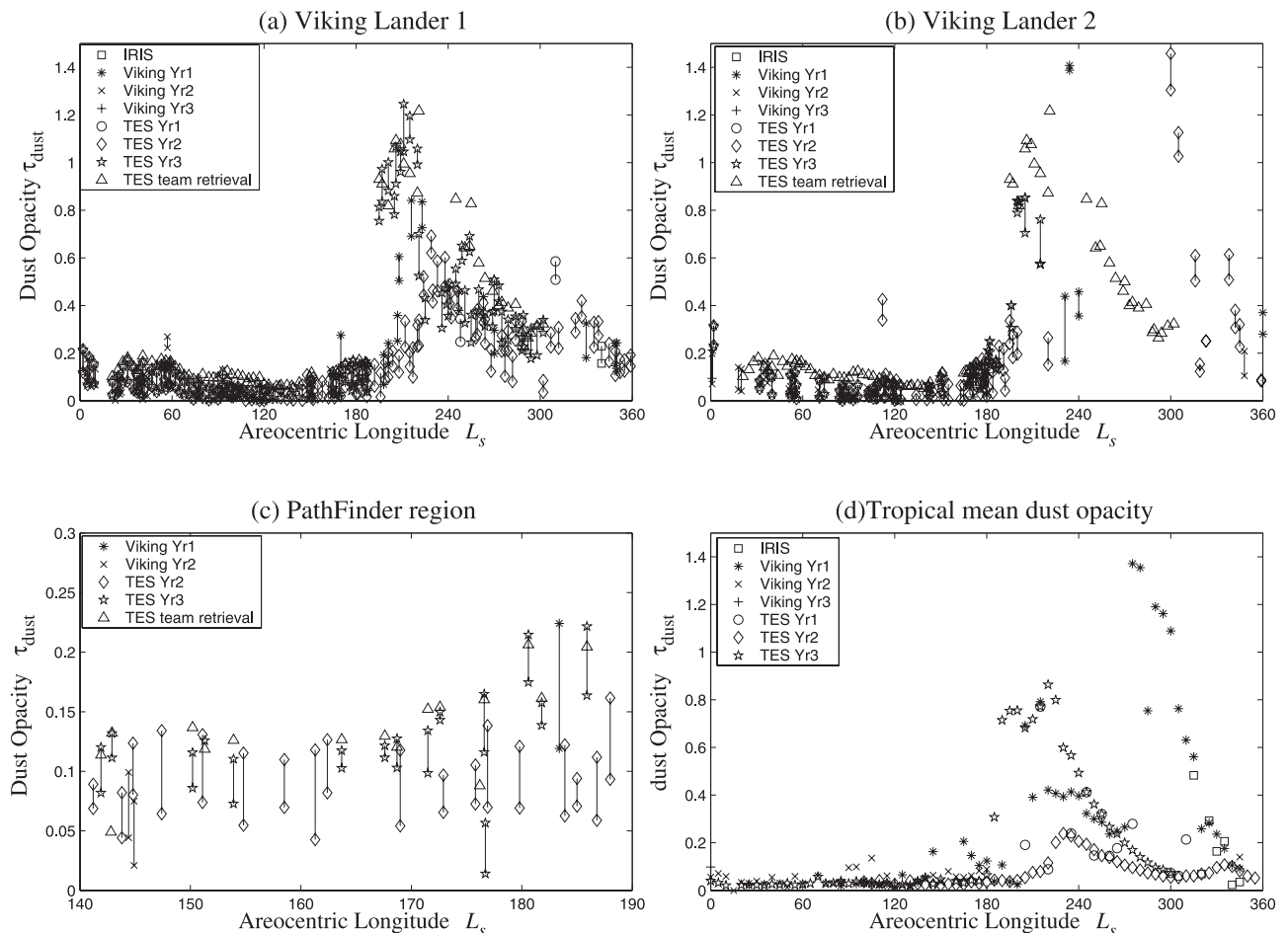
Figure 10. Nontopographically corrected infrared dust opacity for a) the Viking Lander 1 region (22.5°N, 46°W), b) the Viking Lander 2 region (48.5°N, 225.7°W), and c) for the Path Finder region (19.3°N, 33.6°W). Viking Lander region data are shown for the full annual cycle, while the Pathfinder data are only shown for the duration of that mission ($L_s = 140° - 190°$). d) The equatorial averaged dust opacity for all the years. The data are averaged over 5° of L_s, 5° of latitude and 9° of longitude. Only the daytime observations are included. The opacities are constructed using the same mapping and differencing technique used to generate air temperature values for Figure 7. In this case, the latitude range extends from 2.5°S to 2.5°N.

location generally trends from the northeast to the southwest to the west of Elysium. The *Martin* [1986] IRTM scheme is seen to do a very good job in capturing not only the broad behavior of dust, as seen with MOC, but also many of the fine details. On this basis, we conclude that the IRTM dust opacity method is highly robust and capable of providing detailed insight into the spatial distribution of dust. The accuracy of the scheme for cases of high simultaneous water ice cloud opacity, however, is discussed in section 4.2.

4.2. Seasonal Cycle and Interannual Variability
4.2.1. Evolution of Tropical-Average and Landing Site Opacities

[62]   Trends in opacity are illustrated in Figure 10, which shows dust opacities for boxes 5° wide in latitude and longitude, centered on the Viking Lander (VL) Mars Pathfinder (MPF) sites, and for a zonal belt from 2.5°S to 2.5°N. These opacities are not topographically normalized and can be compared with the dust opacities for VL sites derived by *Toigo and Richardson* [2000]. This figure shows that

opacities are at a minimum just after $L_s = 130°$. The maxima in opacity occur at $L_s = 220° - 230°$, associated with dust storms at various stages of development or decay at this season in all the years observed by spacecraft. Maximum opacities are around $\tau_{IR} = 1.0$.

[63]   Three sets of points are plotted on the Lander panels of Figures 10a–10c. Two correspond to different versions of the IRTM-type retrieval of opacity, while the third is the TES-team retrieved opacity (these opacity values can be found on the TES PDS data volumes) [*Smith et al.*, 2000]. The lower-bound IRTM-retrieval points are the direct retrieval of opacity with the measured emissivity maps. The emissivity maps used to represent the emissivity of the ground at 7 and 9 μm were derived by *Christensen* [1998] for the clearest of periods. Unfortunately, even during these periods, some minimal dust was in the atmosphere. It is obvious then that if we attempt to retrieve the dust opacity in the atmosphere with this scheme we will grossly underestimate it for the period of lowest opacity (early to mid northern summer) - as the actual opacity of the atmosphere
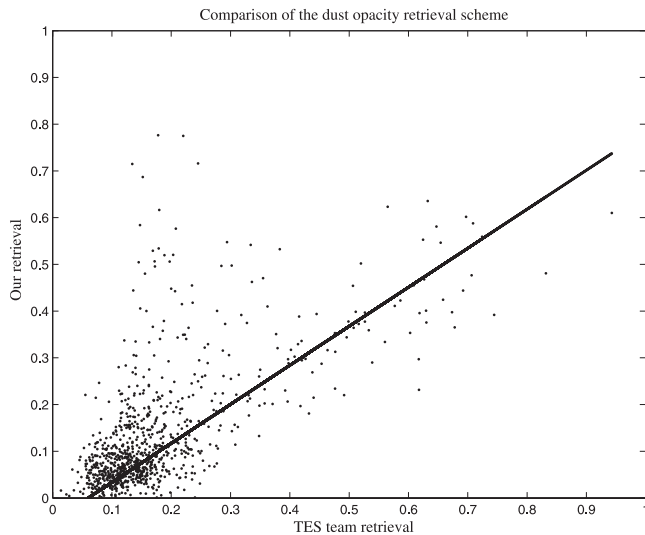
Figure 11. The correlation between the opacity retrieval used in this study and the TES team retrieval included in Planetary Data System released data volumes. In this case, the data are taken from the data volume MGST_0239. The illustrated slope corresponds to the theoretical ratio derived by *Smith et al.* [2000].

at this season is already folded into the surface emissivity maps. This effect can be bound by recalculating 9-μm opacity with surface emissivity set equal at 7 and 9 μm ($\varepsilon_7 = \varepsilon_9$). This will result in an overestimate of 9-μm opacity (except for the effects of water ice - see below), since $\varepsilon_7 > \varepsilon_9$ for nearly all real rocks [*Christensen*, 1998]. These points are shown as the upper values in Figures 10a–10c. Examining the VL1 site observations, the uniform emissivity retrievals show minimum opacities at $L_s = 130°$ of over $\tau_{IR} = 0.05$. The TES team retrievals for this site show minimum opacities at the same season and only very slightly higher than our uniform opacity retrieval ($\tau_{IR} = 0.08$). Figure 11 shows that the ratio of the IRTM-retrieved opacity to the TES team retrieved opacity is not unity, with TES team opacities slightly higher. Thus our upper-bound, minimum opacity estimate and the TES team minimum opacities at VL1 have almost the same magnitude.

[64] The trend in opacity at the Mars Pathfinder site is also shown in Figure 10c. Observations from MPF provide a tight constraint on visible dust opacities because multi-color sky data were collected that allow dust and water ice opacities to be properly distinguished [*Smith and Lemmon*, 1999; *Tomasko et al.*, 1999; *Toigo and Richardson*, 2000]. The MPF visible observations, divided by the empirical visible-to-infrared opacity ratio of 2.5 derived by *Martin* [1986], are also shown. This plot shows again TES-team opacities to agree with upper-bounds on the IRTM-retrievals. However, both are below the visible opacity values. This cannot be due to water ice contamination of the visible opacities, as the dust opacities have been extracted separately from the total opacity thanks to the multiple color data. In order to bring the visible and infrared observations into agreement, a visible-to-infrared ratio of 3.5–4 is required. As shown by *Toigo and Richardson* [2000], very small particles (in a narrow distribution) are required to achieve this, which would be in contradiction to previous

estimates of the dust particle size distribution [e.g., *Pollack et al.*, 1995]. If the difference is not due to particle size, it would appear either that the infrared or the visible opacities are being biased by the water ice cloud to a degree greater than recognized.

[65] The presence of water ice can depress T_7 values and hence reduce the apparent dust opacity of the atmosphere, based on $T_7 - T_{11}$. The potential effect of water ice on these retrievals has been demonstrated by *Toigo and Richardson* [2000] (see their Figures 4 and 5). While for almost all other circumstances this interference is not a major issue due to the absence of water ice clouds, in the tropics in northern spring and summer this effect is significant and leads to a substantial underestimate of dust opacity. The effect is well illustrated in Figure 12, which shows dust and water ice retrievals from the TES team (as extracted from the PDS data volumes) shown along side our retrieval of dust for $L_s = 100°–110°$. In the high northern latitudes, both schemes retrieve relatively high dust opacities at roughly 180° longitude ($\tau_{IR} \sim 0.2–0.3$). However, in the tropics, the TES team dust retrieval results in dust maxima that are strongly correlated geographically with the higher water ice opacities. Our retrieval shows minimum dust opacities in these locations. That the dust and water ice should have co-located maxima in the tropics is likely since there should
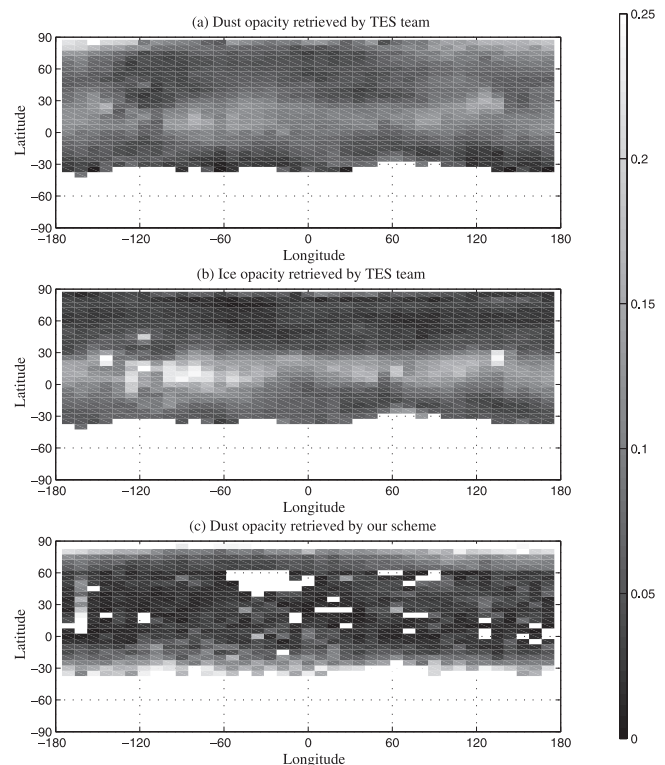

Figure 12. Comparison of dust opacity retrieved using the scheme described in this paper with the TES team retrievals of dust and water ice opacity in the northern summer ($L_s = 100°–110°$). The data are binned in 5° of latitude and 9° of longitude. a) The dust opacity map retrieved by the TES team. b) The ice opacity map retrieved by the TES team. c) The dust opacity map retrieved by our scheme. Data are from TES Year 3.

be a tendency to concentrate dust in the upwelling plumes of the Hadley cell that also give rise to the water ice cloud belt [*Wilson and Hamilton*, 1996; *Richardson et al.*, 2002]. The maximum in dust opacity in the tropics is also supported by independent retrievals of temperature and dust by *Santee and Crisp* [1993]. As such, values of dust loading derived in and around the tropical ice cloud belt by our dust opacity scheme are likely significant underestimates. In principal, it would be possible to adapt the *Martin* [1986] scheme to undertake simultaneous retrievals of dust and water ice. However, the effect is only significant for accurate estimation of minimum tropical opacities in northern spring and summer. More importantly, the main focus of this paper is on interannual variability and the broad spatial behavior of dust and water ice. As Figure 9 demonstrates, during the periods when dust is active (southern spring and summer) the separate retrieval scheme produces excellent results. Further, our study of the interannual variability of dust would only be compromised if there were significant interannual variability of water ice, which we shall show that there is not.

4.2.2. Latitudinal and Seasonal Evolution

[66] The seasonal evolution of zonal-mean dust opacity for all available spacecraft years is shown in Figure 13. The data have been binned in $5°$ of latitude and $5°$ of L_s, using only data collected between 10 am and 6 pm, with all longitudes being included. This figure should be compared with Figure 8, which shows zonal-mean air temperature, in order to see the tight coupling between dust and air temperatures. These figures should also be compared with the annual cycle of observations presented by *Smith et al.* [2001a]. The main signatures in both data sets are the dust storms in southern spring and summer. In particular, all years for which observations exist show strong dust activity at $L_s = 230°$. We will discuss these further in section 4.3.

[67] Examination of the figure shows that opacities are at a minimum in northern spring and summer in the tropics and lower midlatitudes. The distribution with latitude does not show the same structure as air temperature as there are no minima in the tropics. After correcting for topography, the dust is relatively uniformly spread in latitude. As discussed above, our retrieval of dust can be biased by the presence of water ice (this will affect opacities only in the tropics in northern spring and summer), and hence there is likely a tropical dust maximum in this season that is not captured in our retrieval. Opacities begin to rise slowly in late northern summer, and maximize in southern summer.

[68] Persistent dust activity can be seen along the edge of the growing and retreating seasonal ice caps in Figure 13. This is a difficult region within which to retrieve dust due to large temperature inversions over the CO_2 ice cap. However, our code discards any point for which the ground temperature is estimated to be lower than the low-level air temperature. As such, we exclude a priori any case for which "bad" opacities would be generated: all opacities shown are derived over warm surfaces with good spectral contrast. Along the edge of the retreating seasonal caps (both north and south) in the TES year 2, it can be seen that the elevated opacities extend several bins from the edge of data coverage, and show smooth grading of opacity to background levels. This can be contrasted with the lack of elevated opacity along the growing edge of the northern

seasonal cap. Suffice it to say, we do not believe these signatures result from errors in retrieval. These opacities reflect local cap-edge dust storms generated as a result of strong winds driven by cap edge thermal contrasts. There is also strong evidence for these cap edge storms in the MOC data [*Cantor et al.*, 2001; *James and Cantor*, 2001; *Wang and Ingersoll*, 2002]. Indeed, comparison of our Figure 13 with Figure 13 from *Cantor et al.* [2001] shows similar distributions of opacity with latitude as a function of season. Taking $L_s = 150°$ as an example, *Cantor et al.* [2001] show cap edge activity south of $35°$S and north of $60°$N. Our Figure 13 shows opacities higher than 0.4 south of $40°$S. In the north, opacities increase slightly at $70°$N, but are not as elevated as seen in the imaging. At $L_s = 210°$, *Cantor et al.* [2001] show dust activity south of $50°$S and north of $30°$N. In this case, our Figure 13 shows elevated opacity south of $50°$S and north of $40°$N.

[69] It is clear from Figure 13 that the infrared dust opacities are lower in late northern summer (when the northern polar air temperatures are falling) than in other seasons near the cap edge. This may be due to coverage, but we suggest that this could reflect "scrubbing" of dust out of the atmosphere at this season by condensing water ice [e.g., *Kahn*, 1990; *Richardson et al.*, 2002]. Alternatively, the dust may be coated with water ice, as suggested on the basis of MOC image analysis by *Cantor et al.* [2001] and *James and Cantor* [2001]. The strong cap edge activity in late southern spring eventually results in significant dust opacities covering much of the high southern latitudes. Some of these are associated with regional dust storms, as discussed in section 4.3. It is worth noting that we obtained significantly higher polar dust opacities than those of *Smith et al.* [2000, 2001a, 2001b, 2002], who obtained dust opacities during the TES year 2 dust storm that are equal or higher in the tropics than at high latitudes. This can be seen in a different form in Figure 11. It is not clear, a priori, whether our opacities are an over estimate, the TES team retrievals are an underestimate, or whether the true opacities lie between these two estimates. Examination of MOC color WA images (H. Wang, personal communication, 2002) suggests higher polar opacities than tropical opacities during this storm, indicating that there is no major discrepancy between our retrieval and the MOC imagery.

[70] Cap edge lifting events at these seasons and latitudes are evident and nearly identical in the three TES years. Some evidence for these cap edge storms is also present in the Viking data. In Viking year 1, there is evidence of cap edge lifting along the retreating southern seasonal cap edge that is very similar to that seen in TES year 2. Viking year 2 shows some evidence for cap edge activity along the retreating edge of the northern seasonal cap. These observations suggest that similar cap edge activity was ongoing during both the Viking and MGS missions, and that there may not be as strong of a distinction in cap edge storm behavior between the periods observed by the different spacecraft as suggested by *Cantor et al.* [2001] (see also *James and Cantor* [2001]).

4.2.3. Interannual Variability of Dust

[71] Figure 10d shows that the northern spring and summer season dust opacity is extremely repeatable, regardless of which location is considered. Five Mars years worth of observations are available in northern summer for
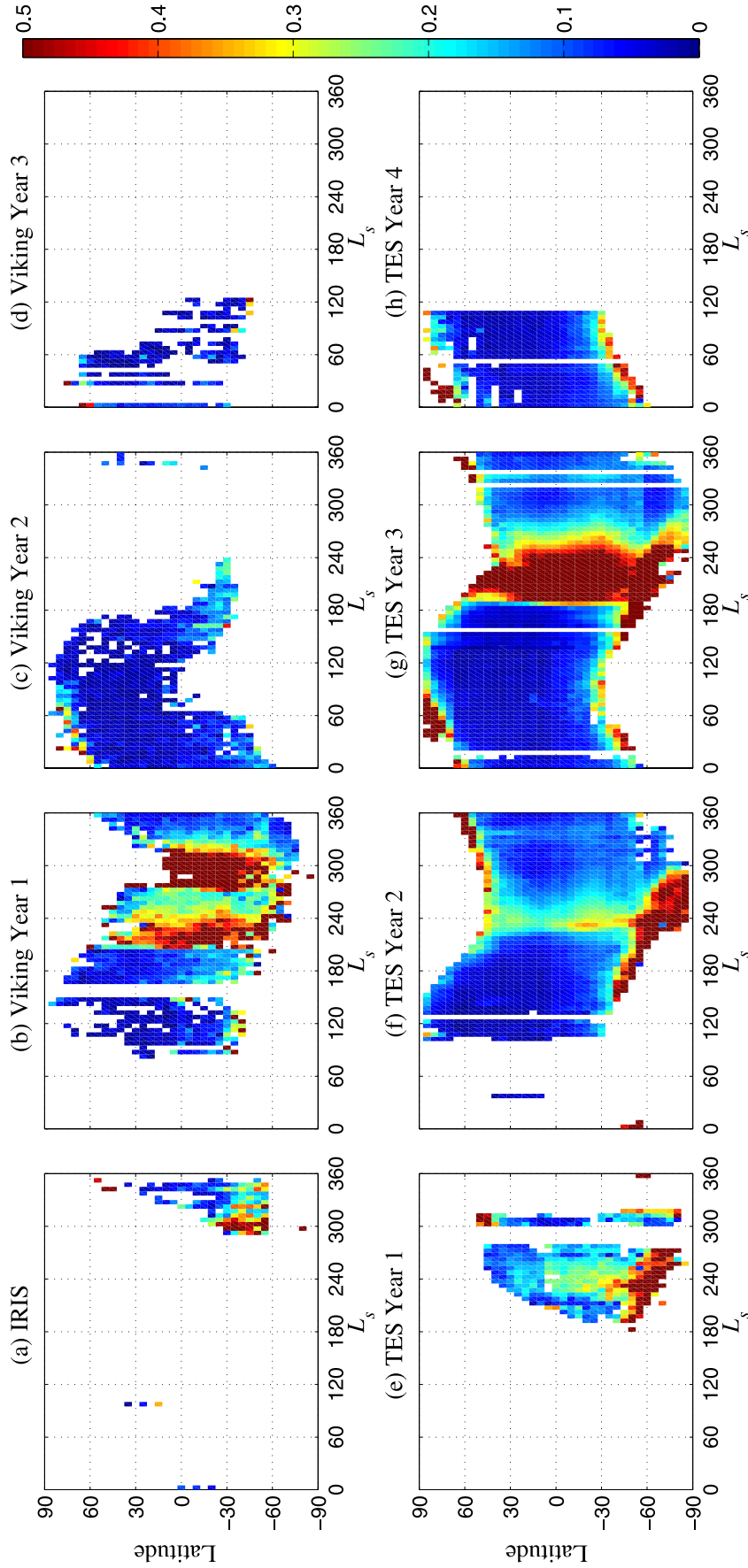
Figure 13. Zonal-mean dust opacity (IRTM 9-μm channel wavelengths) as a function of latitude and L_s. The data are binned by 5° of latitude and 5° of L_s, including only data collected between 10 am and 6 pm, with all longitude being included. Data comes from: a) IRIS, b) Viking Year 1, c) Viking Year 2, d) Viking Year 3, e) TES year 1, f) TES year 2, g) TES year 3, and h) TES year 4.
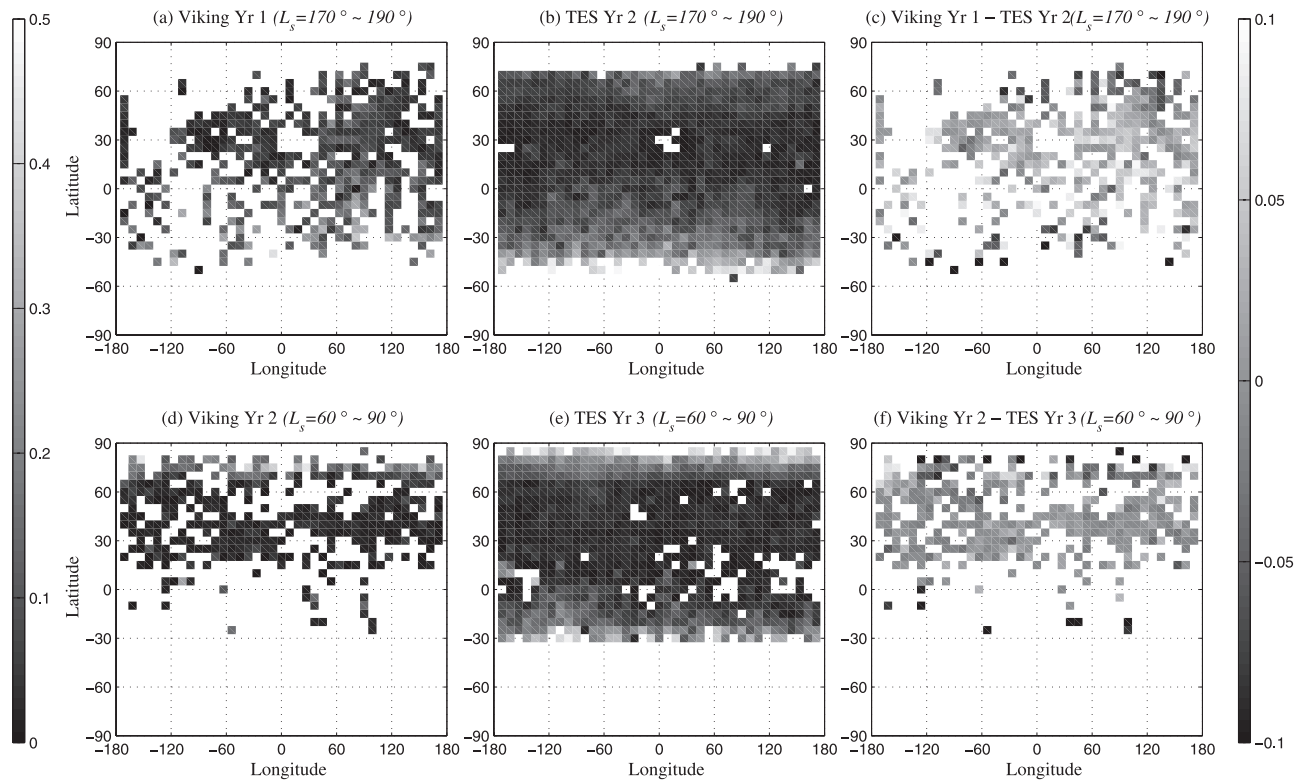
Figure 14. Dust opacity difference between years for Northern summer and spring. The data are averaged over 5° of latitude and 9° of longitude, for local times 10 am to 6 pm. a) Dust opacity for Viking year 1 for $L_s = 170°-190°$. b) Dust opacity for TES year 2 for $L_s = 170°-190°$. c) a)–b). d) Dust opacity for Viking year 2 for $L_s = 60°-90°$. e) Dust opacity for TES year 3 for $L_s = 60°-90°$. f) d)–e).

these sites, with the opacities repeating in these years to within 10% for the equatorial belt. With reduced coverage over the lander sites, the repeatability is reduced to about 20%. The equatorial dust opacity plot was constructed with a method similar to that for the global air temperatures, which uses spatial information to reduce spatial biases in the averaging. This method is illustrated in Figure 14, which shows the geographical distribution of opacity for $L_s = 60°-90°$ for Viking year 2 (during the period of highest repeatability) and TES year 3, and for $L_s = 170°-190°$ (during the transition from the repeatable northern summer into the southern spring season during which substantial dust storms can develop) for Viking year 1 and TES year 2. The differences in coverage between Viking and MGS are quite clear. If straight differences are taken between these maps (say between Figures 14d and 14e, with means of 0.056 and 0.119) the result can be deceptively large (0.06). However, if the differences are only taken between the maps where coincident coverage exists, a better approximation to the true difference is achieved (i.e., without spatial biases). Figures 14c and 14f show the spatial distribution of point-by-point differences across these maps. Taking the average of these differences generates nonbiased difference values of 2×10^{-2} (Figure 14c) and -8×10^{-4} (Figure 14f). Thus the dust opacities are highly consistent from year to year for northern spring and summer, to within 20% for $L_s = 170°-190°$, and less than 10% for $L_s = 60°-90°$. Some spatial patterns of difference can be seen between the Viking and TES years for $L_s = 170°-190°$. The Viking data show somewhat

elevated opacity in the southern midlatitudes that is associated with local dust activity in the Hellas basin (see figures of *Martin and Richardson* [1993]). If this event is removed from the Viking data, the difference between the TES and Viking data sets are even smaller. The repeatability of the dust cycle, most pronounced during the mid- to late-northern spring and early to mid-northern summer is highly consistent with the very tight closure of the annual air temperatures (to within 1 K; see section 3) in these seasons. These results are undermined to some degree by the influence of ice on the retrieval of dust opacity, as described above. However, the water ice also shows a strong pattern of repeatability (see section 5.3). In addition, the lack of interannual variability in northern spring and summer dust opacity is consistent with the lack of variability of the pressure tides at the VL sites [*Wilson and Hamilton*, 1996], which should reflect any changes in the thermal forcing of the atmosphere by dust.

4.3. Dust Storm Origin, Evolution, and Decay
4.3.1. Southern Spring Dust Storms
[72] The spacecraft record of Mars' southern spring now extends to four Mars years. In each of these years (Viking year 1, and all MGS years) the atmosphere is extremely dusty at $L_s = 230°$, which is associated with major dust storm development or decay. It is these elevated dust events that generate the distinct and sharp spike in the global air temperature record at this season (Figure 7). The southern spring storms are shown in zonal-average opacity form in
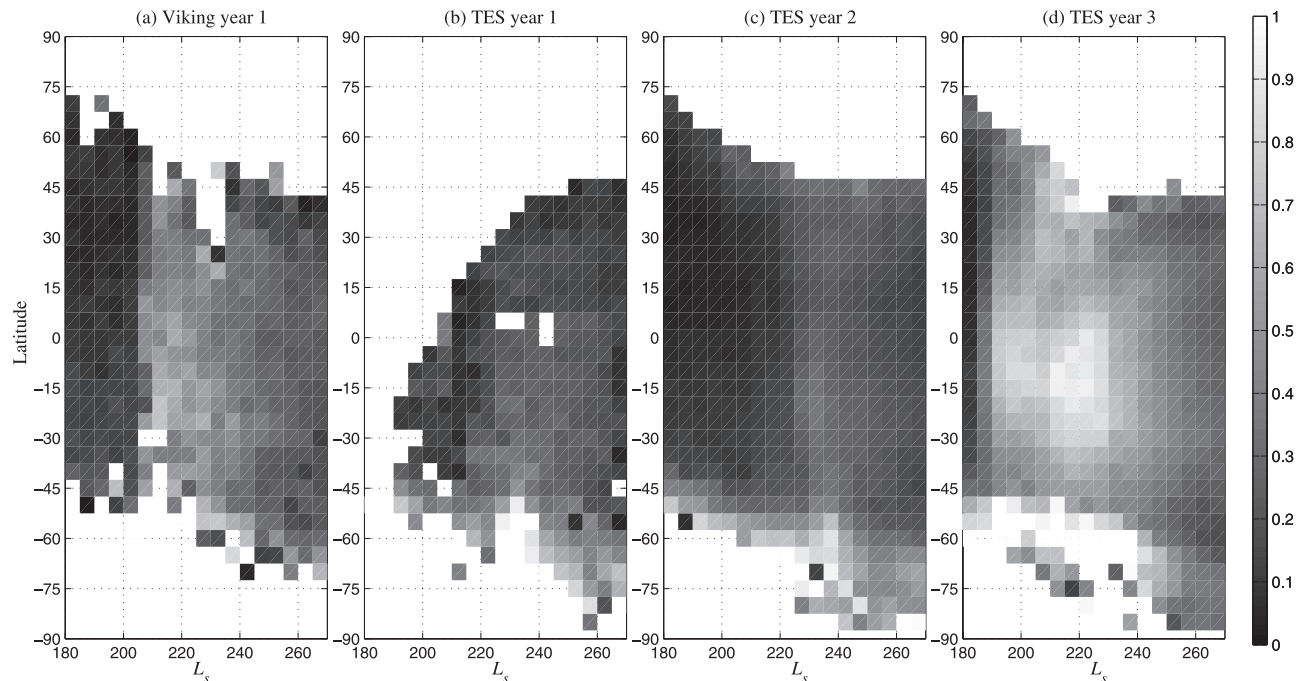
Figure 15. The southern spring dust storms. The data are zonal averaged and binned in 5° latitude and 5° L_s. a) Viking year 1. b) TES year 1. c) TES year 2. d) TES year 3.

Figure 15. The storms are the 1977a storm from Viking year 1 [*Briggs et al.*, 1979; *Martin and Richardson*, 1993], and the MGS storms of 1997 (TES year 1) (the "Noachis" storm) [*Smith et al.*, 2000], 1999 (TES year 2) [*Cantor et al.*, 2001; *Smith et al.*, 2001b], and the planet-encircling 2001 dust storm [*Smith et al.*, 2002]. With the exception of the TES year 2 storm, each of these events is believed to have begun in the southern hemisphere. In the case of the 1977a storm, on the Tharsis plateau south and west of Solis Planum; the TES year 1 storm, on the southern highlands in Noachis Terra; and 2001 in the Hellas basin. Contrasting the TES year 1 and TES year 2 storms, it is clear that the TES year 1 storm did not transport significant dust into the northern hemisphere. In the case of the TES year 2 storm, the dust storm event likely originated in the northern hemisphere, as is evident in the thermal infrared and imaging data (next section) [*Cantor et al.*, 2001; *Wang et al.*, 2003]. For the Viking 1977a storm, the conventional wisdom has been that the storm began in the southern hemisphere, as stated above. However, the IRTM and imaging coverage were quite poor. While the imaging data suggest that the atmosphere to the north and east of the earliest identified 1977a storm progenitor (at $L_s = 205°$) was clear, the observations of the 1999 storm leads one to wonder where, exactly, the 1977a storm began (although it probably did begin in the south).

4.3.2. "Flushing" Dust Storm of TES Year 2

[73] The 1999 southern spring storm represents a completely different mechanism of dust storm origin from (at least) the other MGS storms. Its behavior, as observed in the visible, has been described by *Cantor et al.* [2002]. While the infrared data have been shown by *Smith et al.* [2001b], the true origin of the storm was not apparent in the data or discussion provided there. Here, we demonstrate that the

storm behavior in the infrared is consistent with the MOC observations.

[74] Figure 16 shows spatial maps of dust opacity at time intervals of 2° of L_s from $L_s = 205°-245°$. Dust activity can be seen throughout this period at the edge of the southern seasonal cap, associated with cap-edge winds. At the northern edge of the data, sporadic dust events can be seen that are also evident in the MOC imaging (H. Wang, personal communication, 2002). One example is near 120°W and north of 45°N at $L_s = 216°$. Other events are evident at $L_s = 210°$ and $L_s = 220°$, at pretty much the same latitude, and at 30°W. However, these events become ensnared in the southward, low-level Hadley return flow, as also shown in Figures 10 and 11 of *Cantor et al.* [2001]. The $L_s = 210°$ event flushes into the southern hemisphere and then decays (Figures 16c and 16d). The $L_s = 220°$ event is quite a bit stronger, and can be seen crossing the equator in Figures 16h, 16i, 16j, and 16k. At this point, the dust accumulates in the southern convergence zone (defined by the upwelling branch of the Hadley circulation) and spreads rapidly in the westerly trade winds (subtropical jets that are prominent at this latitude of ∼30°S [*Haberle et al.*, 1993]). This westerly spreading between 0° and 30°S can be seen in Figures 16k, 16l, 16m, and 16n. It is this expansion that is noted by *Smith et al.* [2001b] as the origin of the storm. With dust now filling the southern tropical convergence zone, the Hadley cell is intensified, and this generates the signature in the air temperature date (Figure 8).

[75] The sequence of events that lead to the 1999 southern spring storm, and similar "flushing" events that did not spark storms of global impact, have already been described by *Cantor et al.* [2001] and *Wang et al.* [2003] (we define the term "flushing" to represent the cross-equatorial transport of large dust fronts, and the "flushing dust storm" as
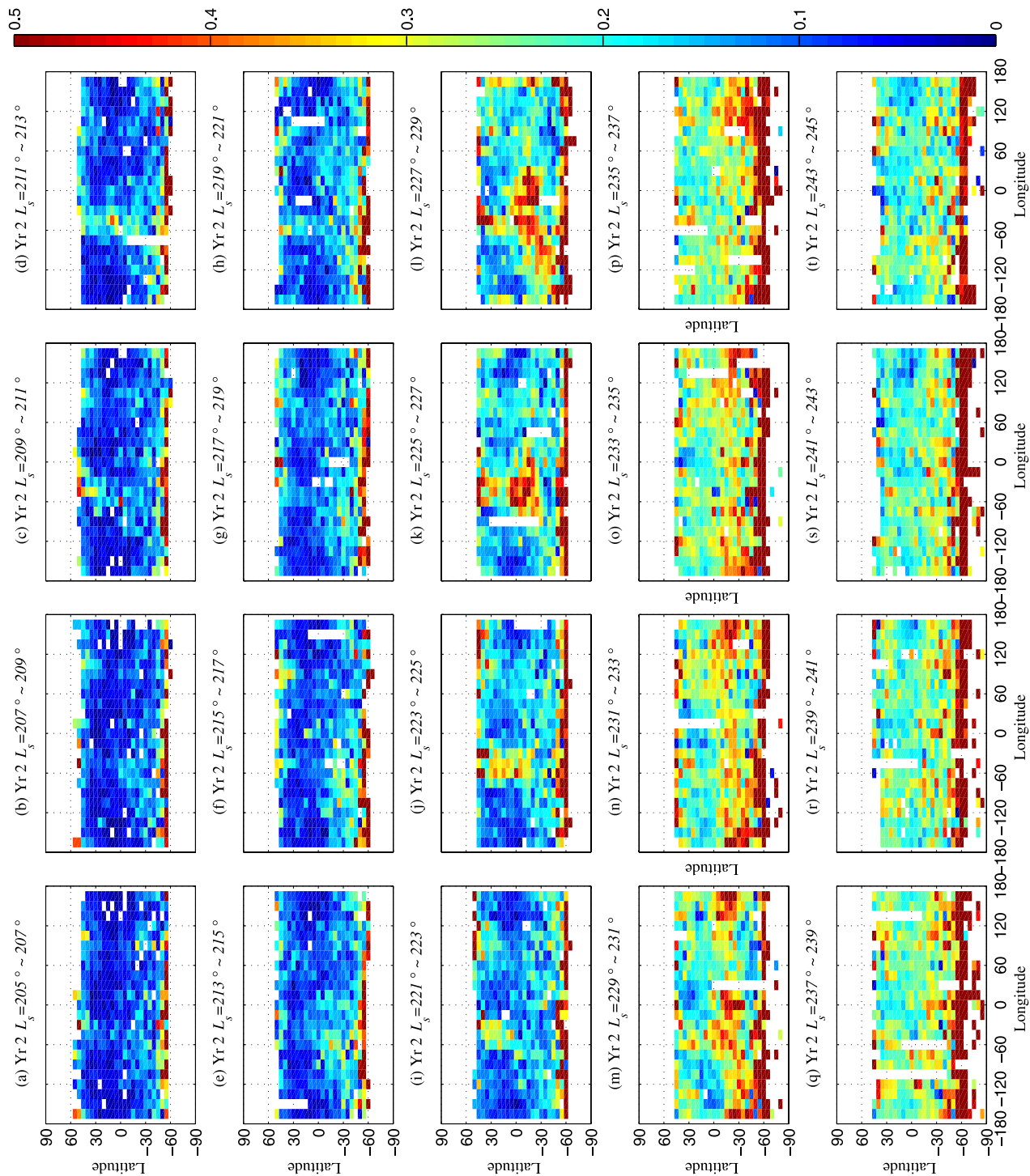
the large storm that resulted from the accumulation of successive ''flushing'' events in the southern tropics). However, it is should be emphasized just how interesting and novel this event is, as it represents a generation mechanism for large-scale storms that is (apparently) completely different from those responsible for all of the other southern spring storms. In particular, very easily appreciated mechanisms are implicated for initial dust lifting by strong winds associated with the northern polar frontal storms and the subsequent transport into the southern hemisphere by the western boundary current associated with the lower branch of the Hadley circulation. We suggest that this represents a completely novel telecommunication phenomena in the Martian atmosphere [*Wang et al.*, 2003]. These events couple mesoscale and synoptic scale meteorological phenomena in ways that on the one hand lay down a challenge for dynamical modeling (because of the mixture of scales), but on the other, are sufficiently clearly illustrated in the data as to be very unambiguous targets for such modeling. In any case, a completely new mechanism for dust storm genesis has been revealed.

[76] The 1999 storm event also provides something of a categorization quandary. As clearly shown in Figure 16 and evident in the MOC WA images (H. Wang, personal communication, 2003), the dust storm begins with lifting events in the high northern latitudes, moves into the southern tropics, and encircles the planet at those latitudes. However, compared with the 2001 global dust storm, the 1999 storm was quite small and did not enshroud the planet. Categorization following *Martin and Zurek* [1993] is then difficult as the storm is significantly larger than regional (it builds from the agglomeration of several regional frontal storms), but not quite global. *Martin and Zurek* [1993] use the term ''planet encircling'' for the largest category of dust storm, but while the 1999 storm did encircle the planet, it was hardly in the same league as the 2001 storm (section 4.3.3). We would therefore propose to split the category for dust storms that are larger than regional into ''planet-encircling'' and ''planet enshrouding'' (or truly global) storms.

4.3.3. The 2001 Planet-Encircling (Global) Storm

[77] TES observations of the 2001 storm have previously been shown by *Smith et al.* [2002]. We include plots and discussion here for completeness. Figure 17 shows opacity maps at intervals of 2° of L_s for the developmental period of the storm. The first four frames show clearly that the storm began as a local event on the northwestern rim of the Hellas Basin and the nearby southern highlands. The storm grew slowly and moved to the east over the course of the following ∼6° of L_s (∼10 days). Drift to the east would be expected, since the diurnal-mean wind at these latitudes is to the east within the just-established convergent jet of the Hadley cell low-level return flow. The storm center moves roughly 800 km in 10 days, which is consistent with a low-level wind of ∼1 ms⁻¹. This is the right order of magnitude for the low-level wind, and hence it is possible that the storm motion is due to advection. However, additional dust

lifting is clearly occurring as the system moves since the opacity of the storm grows between each map (Figures 17a– 17d). Explosive growth occurred in the subsequent ∼8° of L_s, as the region of high dust opacity (>0.5) expanded to encircle the planet. The rapid development of opacity in Daedalia Planum between $L_s = 188°$ and 190°, would require mean transport speeds of over 20 ms⁻¹, and combined with the fact that there appears to be a subtle break in opacity around 180° longitude, this suggests that Daedalia Planum is a separate lifting center. After ∼$L_s = 195°$, there was little net growth of the storm in terms of size or opacity. However, the structure of the global dust cloud (the spatial distribution of opacity maxima and minima) did change, accompanied by relatively subtle increases and decreases in total opacity.

[78] The location of the initial dust cloud suggests that an ultimate model for the initiation of this storm will have to involve dust lifting on the rim of the Hellas basin, and it is possible that the location of the seasonal cap within the Hellas Basin will be important [*Siili et al.*, 1997]. Dust activity in Hellas is quite commonly observed in MOC WA images (H. Wang, personal communication, 2003); thus a major challenge will be in understanding the mix of circulation systems and circumstances that allowed a small storm to blow up into a global-scale event in this particular case, and not in others. The initiation of secondary lifting centers after an initial dust storm has begun also presents a major challenge. The interaction between dust and water ice in the Hellas Basin, later in the 2001 storm, is discussed in section 5.2.3.

4.3.4. Dust Storm Decay Rates

[79] Dust storm decay rates have been reported for Mariner 9 [*Fenton et al.*, 1997], Viking [*Pollack et al.*, 1979], and MGS [*Smith et al.*, 2000], each using different techniques for opacity retrieval. The opacity decay behaviors for all missions at the equator and at 30°S are shown in Figure 18. Previous decay rate estimates from various locations and storms range from 40 to 80 days. We show decay rates for each of the major storms, holding the location of the plots constant. The aim is to provide additional, uniform measurements to allow relative comparison. Our estimates generally show decay rates that are somewhat lower than previous estimates (ranging from 20 days to over 60 days). The spread in dust opacity values at any given L_s makes tightly constraining the decay rate difficult.

5. Water Ice Opacity

[80] Water ice clouds provide a unique means for studying the dynamics of the Martian climate. The evolution of the spatial distribution of clouds over the course of the annual cycle provides important information about the transport of water vapor, the circulation of the atmosphere (specifically about the location of upwelling), the atmospheric temperature structure, and radiative cooling. Examination of the interannual repeatability of these cloud systems hence provides insight into the repeatability of all of these components, albeit in a convolved sense. As a

Figure 16. (opposite) The evolution of dust opacity and the generation of ''dust flushing'' events in TES year 2. The data are binned in 5° latitude and 15° longitude. Every map is composed of the retrieved dust opacity for 2° of L_s. The whole L_s range is from 205° to 245°. L_s for each panel is as indicated in figure.
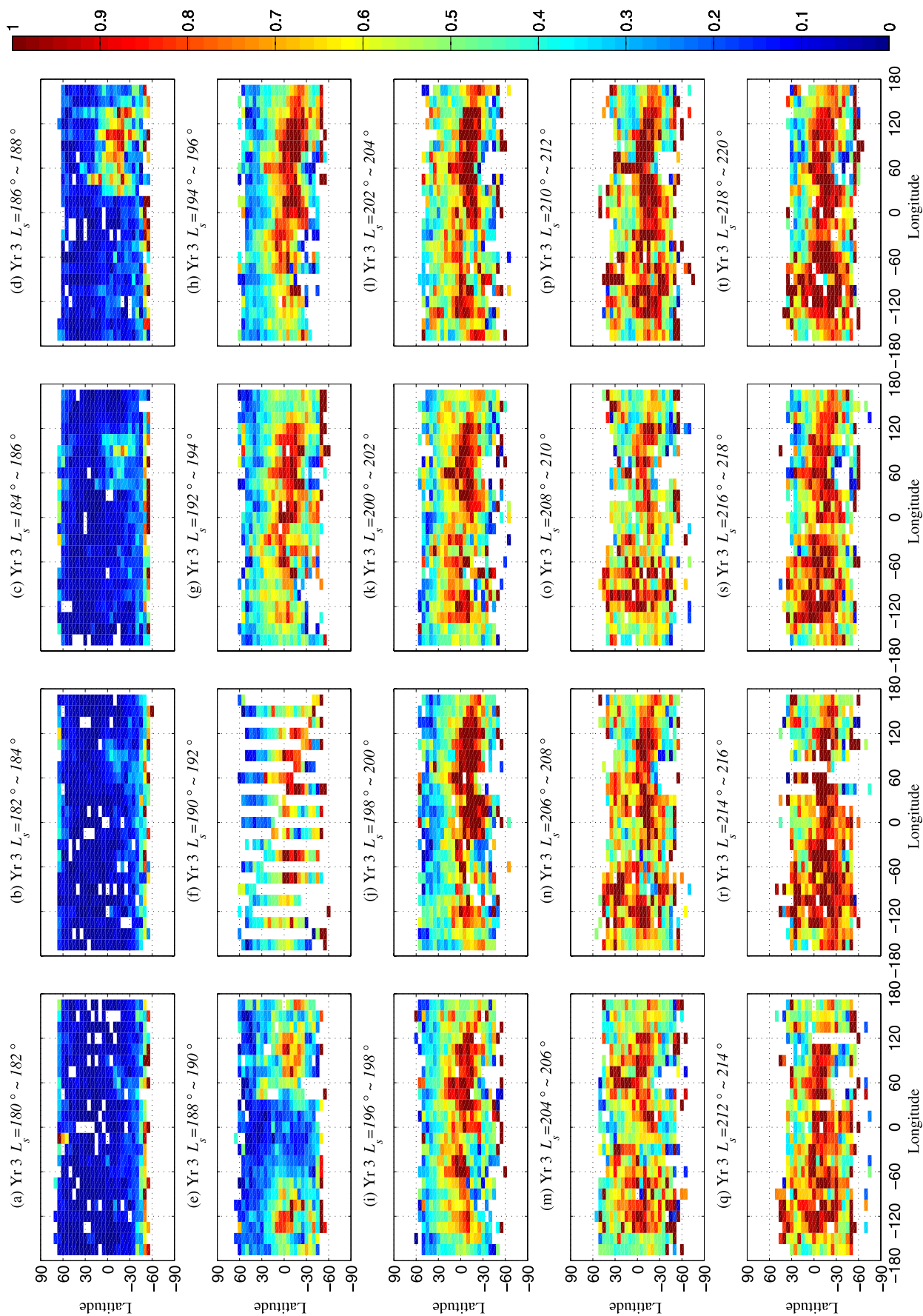
Figure 17. Same as Figure 16 but for the 2001 global dust storm.
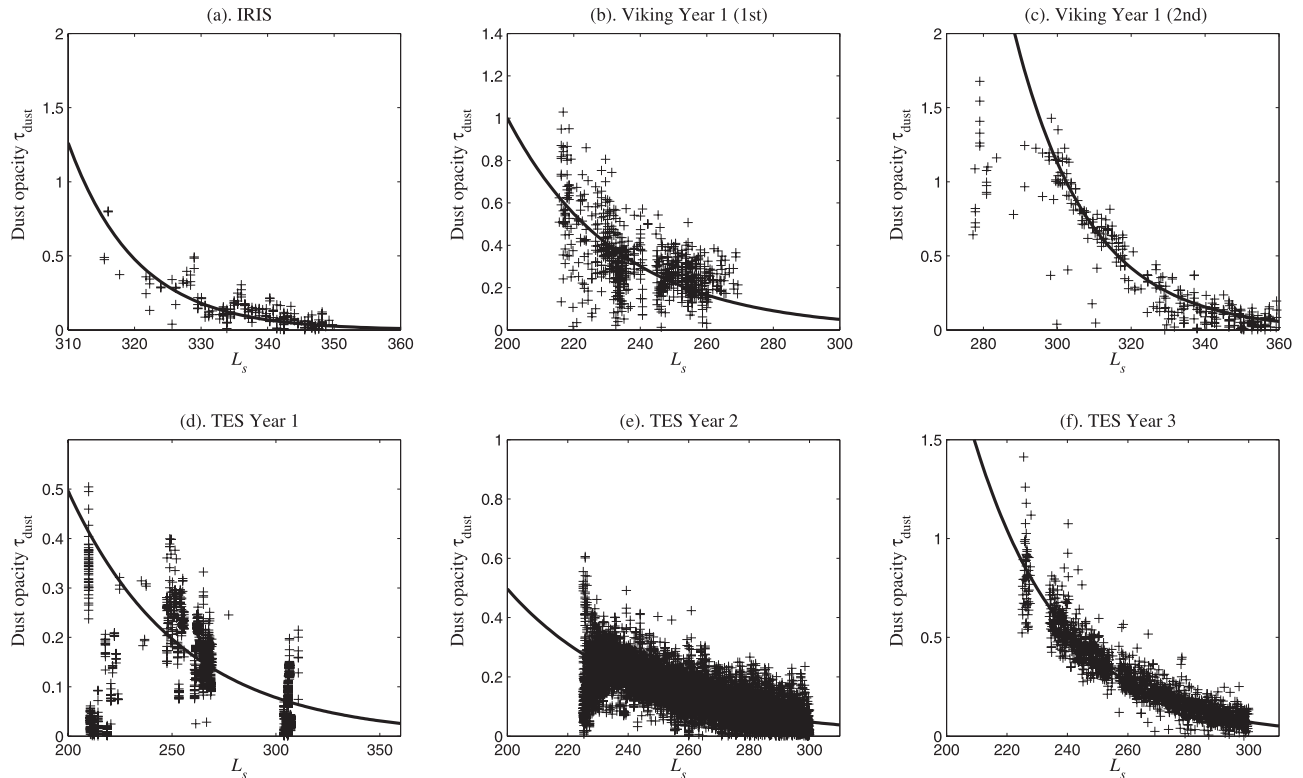
Figure 18. Dust decay rate in the equatorial region (2.5°S−2.5°N), including data from all longitudes, but only daytime observation. a) IRIS dust storm. b) The first dust storm in Viking year 1. c) The second dust storm in Viking year 1. d) The dust storm in TES year 1. e) The dust storm in TES year 2.

result, the water ice cloud cycle is one of the more sensitive tools for study climate. Further, water ice clouds provide additional and distinct information about the Martian climate in addition to the cycles of air temperature and dust already discussed.

[81] In this section, we provide some discussion of the validity of the new water ice retrieval scheme developed for this study by comparing results with MOC images [*Wang and Ingersoll*, 2002] and the published water ice cloud retrievals derived by the TES team [*Pearl et al.*, 2001]. We show the evolution of the major cloud systems throughout the Viking and MGS mission, with specific emphasis on the tropical cloud belt. Finally, the degree of interannual variability is examined.

5.1. Comparison With the MOC Images and the TES Team Retrievals

[82] The period $L_s = 134° − 140°$ in mid-northern summer is the first for which nominal MOC mapping mission images are available from the second MGS year. It also corresponds to a time of well-developed tropical water ice clouds [*Pearl et al.*, 2001; *Wang and Ingersoll*, 2002]. In Figure 19 we show the tropical ice cloud belt (and parts of the southern polar hood) as viewed by MOC (Figure 19a) [*Wang and Ingersoll*, 2002], by TES and processed by the TES team (Figure 19c) [*Pearl et al.*, 2001], and by TES using the retrieval scheme described in section 2 (Figure 19b). A longitudinally variable, but still relatively coherent tropical cloud belt is visible in each of the maps, with concentrations of cloud over Tharsis and the associated shield volcanoes, the rims of Isidis Planitia, Hellas, and Argyre,

and over Elyssium. Satisfyingly, at the broadest level, all three maps show essentially the same features.

[83] The detail of the coherence between our retrieval from the TES data and the MOC data is extremely good for many, very fine-scale features of the cloud distribution. Topographic clouds associated with all five of the Tharsis volcanoes (Olympus, Ascraeus, Pavonis, Arsia Mons, and Alba Patera) are clearly evident in both data sets, but also are features like the trailing cloud tail to the north and west of Olympus Mons (22°N, 140°W). Also captured in both data sets is the northeast trending, linear cloud structure between 30°N, 80°W and 45°N, 50°W. A distinct arcuate concentration in the cloud belt is seen at 15°N, 75°E in both data sets that corresponds to the rim of Isidis Planitia. Some apparent differences exist between the data sets, for example, to the south of the most southerly of the Tharsis shield volcanoes at 20°S, 120°W, and at 30°S and 10°W. However, closer inspection of the MOC data show that these regions do, in fact, exhibit visible clouds, but that clouds in these regions are transient. Because the MOC data are wide-angle, they capture the regions multiple times within the observation period. This tends to average-out transient clouds maps (H. Wang, personal communication, 2002). TES provides a single strip sample on each orbit, and as such, multiple samples of transients remain in our TES-retrieved maps. Overall, the IRTM-scheme appears to perform very well.

5.2. Seasonal Cycle

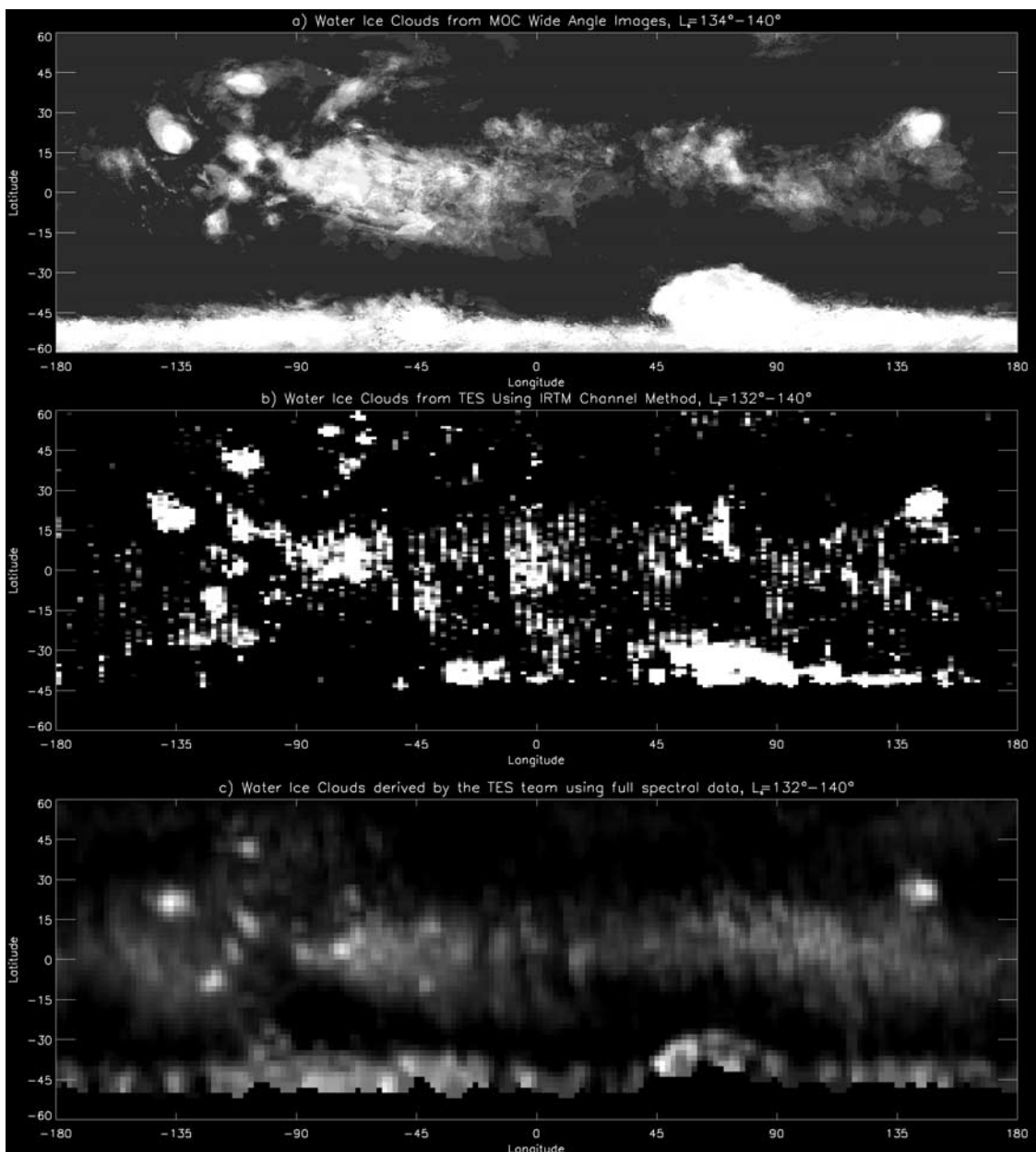[84] The seasonal cycles of zonal mean cloud opacity for the IRIS, IRTM, and TES data sets are shown in Figure 20.

Figure 19. Water ice in the Martian atmosphere for $L_s = 134° - 140°$ from TES Year 2. a) Water ice as identified using the Mars Orbiter Camera Wide-angle color imager (H. Wang, personal communication, 2002). b) 11-μm water ice opacity using the IRTM scheme discussed in this paper. c) Infrared ice opacity retrieved by the TES-team (M. Smith, personal communication, 2002).

A similar plot for TES year 2 data have been shown by *Smith et al.* [2001a]. The combined data sets presented here allow the full annual cycle of water ice cloud systems to be examined for at least two Mars years. There are two major features evident in these figures: the tropical cloud belt, and polar hood clouds.

5.2.1. Tropical Cloud Belt

[85] The latitudinal distribution of water ice at the time of peak belt thickness is best gauged from the TES year 3 data. From $L_s = 90 - 110°$ the zonal-mean belt can be said to extend from the equator to about 30°N (rather arbitrarily, on the basis of opacities greater than ∼0.2). In fact, elevated opacities (greater than 0.05) exist across the tropics through-

out most of northern spring and summer. Defining a time of commencement for the tropical cloud belt is somewhat difficult as water ice opacities are elevated near the equator at times during southern summer. However, cloud opacity builds quite strongly within the period $L_s = 0° - 30°$. Thickening of zonal mean cloud into a recognizable belt sitting north of the equator occurs somewhere around $L_s = 40°$. This belt thickens progressively until about $L_s = 80° - 90°$, at which point it has attained maximum opacity (0.25 - 0.3). Opacities remain at these high levels until roughly $L_s = 120°$, and then fall slowly. A major decrease in opacity occurs near $L_s = 140°$, as reported by *Pearl et al.* [2001]. Zonal-mean water ice cloud remains in the tropics at levels

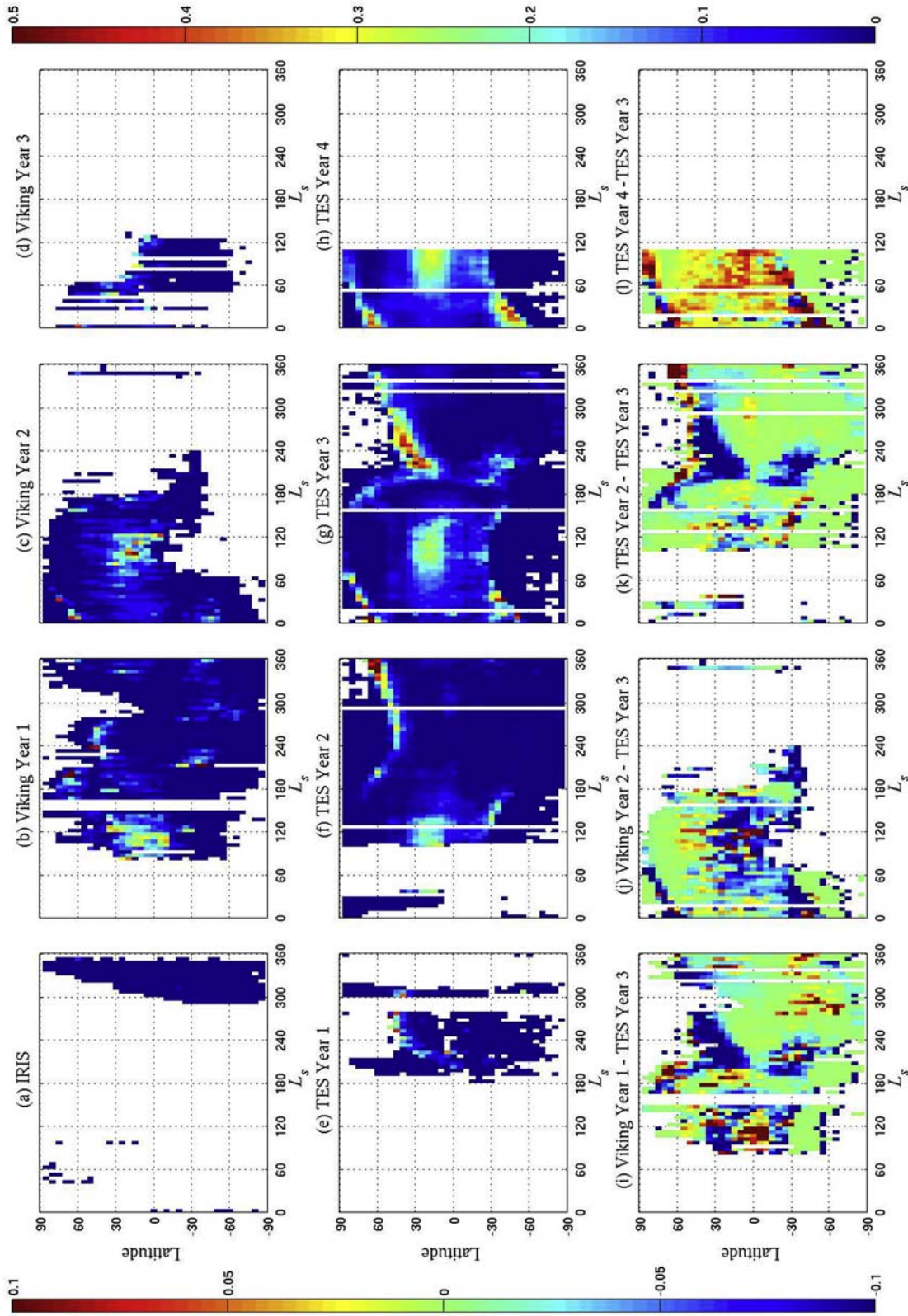**Figure 20.** Zonal-mean water ice opacity as a function of latitude and L_s. The data are binned by 5° of latitude and 5° of L_s, including only data collected between 10 am and 6 pm, with all longitude being included. a) IRIS. b) Viking Year 1. c) Viking Year 2. d) Viking Year 3. e) TES year 1. f) TES year 2. g) TES year 3. h) TES year 4. i)–l) Differences between various years. Note the color bar for a)–h) is on the right, while the color bar for i)–l) is on the left.
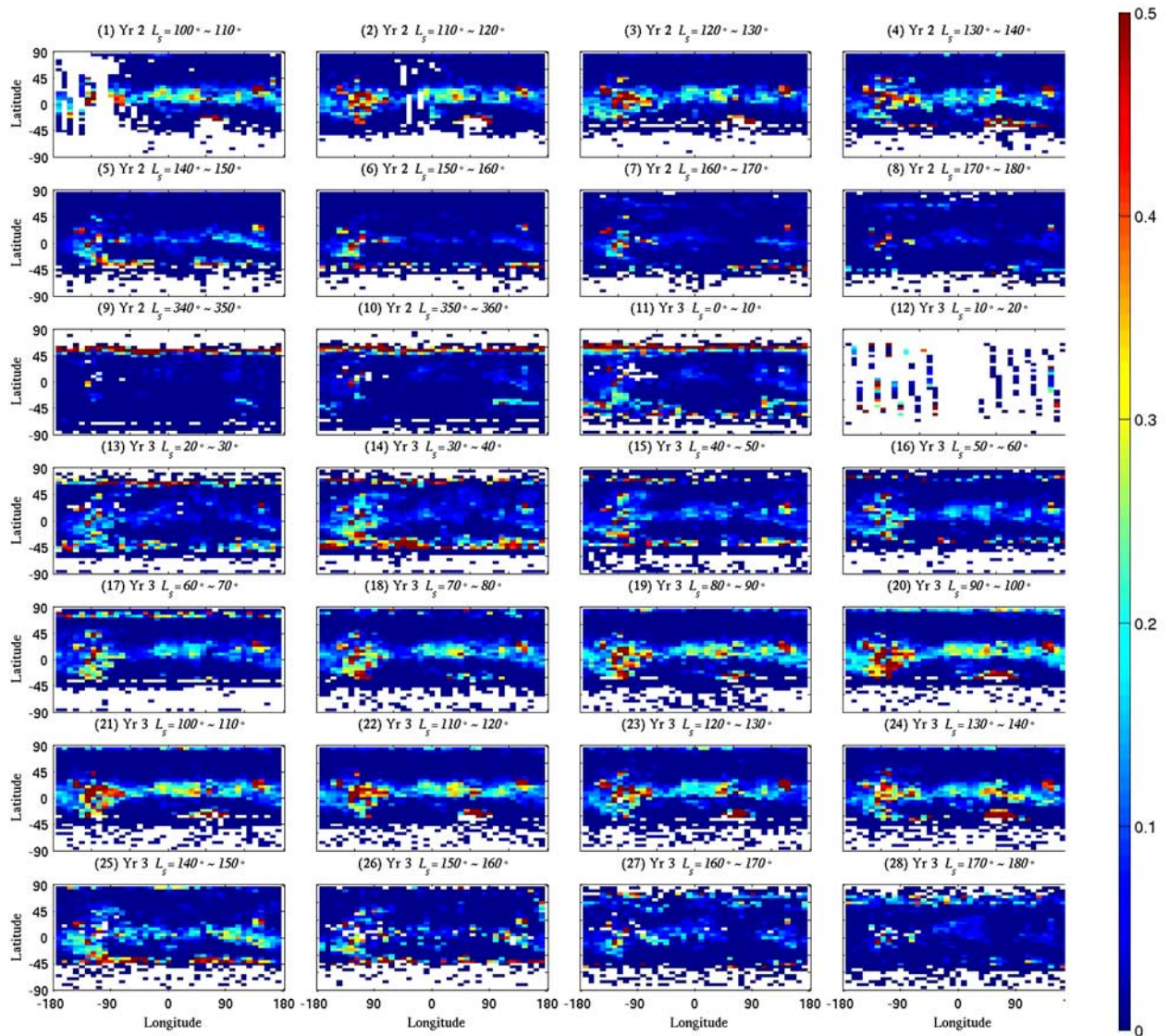
Figure 21. The evolution of the northern spring and summer tropical water ice cloud belt for TES years 2 and 3. The data are averaged in 5° of the latitude and 9° of the longitude. Each map contains the water ice opacity retrieved over 10° of L_s. The seasonal dates for each panel are as indicated in the figure.

of up to 0.1–0.15. The ice opacity decreases to below our threshold for detection by $L_s = 210°$.

[86] The same patterns of zonal-mean cloud behavior can be seen in both the IRTM and TES data. However, the IRTM data are significantly more noisy. This is mainly due to the great differences in spatial coverage, and also to the lower data volume of IRTM. As expected, little cloud ice is observed in the IRIS data set, which mainly consists of dust storm observations. Only one bin sits in the cloud belt at $L_s = 90°$ and 15°N. Here, the opacity is 0.35.

[87] The evolution of the cloud belt during northern spring and summer can be viewed in greater detail in Figure 21. This figure shows geographical maps of cloud ice opacity in 10° bins of L_s. TES data from years 2 and 3 are shown because in combination they provide excellent coverage for the whole of northern spring and summer (with the exception of $L_s = 10°–20°$, during which time no data were returned due to solar conjunction). Figure 21(11) shows that

at the very beginning of northern spring, tropical clouds are already established with a broken belt existing between the equator at 30°N. Highest opacity concentrations are over Tharsis, as they are throughout the northern spring and summer. The tropical cloud builds after conjunction, until by $L_s = 40°$, a cloud belt is seen to exist which is similar in form to that observed by the Hubble Space Telescope [Clancy et al., 1996; James et al., 1996]. After $L_s = 40°$, the cloud belt shape remains rather consistent for the rest of northern spring. Development after $L_s = 40°$ mainly consists of thickening, in the sense of increasing opacity. The Tharsis, Elysium, and Arabia regions, in particular, can be seen to strongly increase in opacity. The belt remains very similar in shape and opacity between $L_s = 80°–140°$. The rapid decay after $L_s = 140°$ is both in opacity and in shape. Cloud essentially disappears from the regions between Elysium and Tharsis, and between Tharsis and Arabia. The clouds remain thick over Tharsis and Elysium.
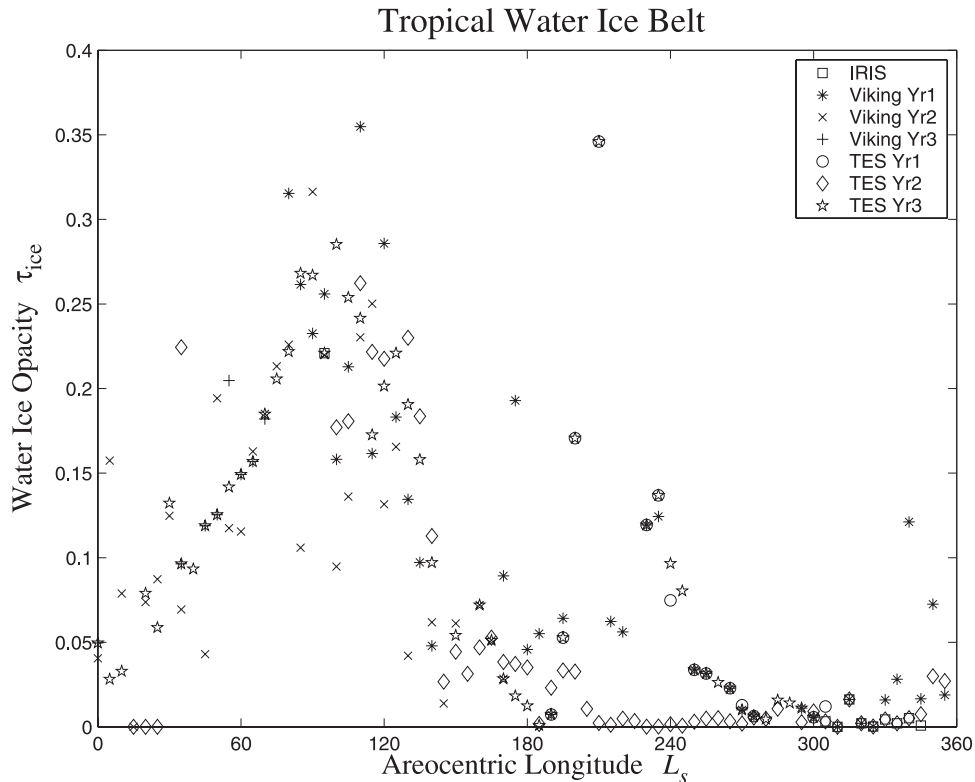
Figure 22. Tropical averaged water ice opacity for all the years. The water ice opacity is averaged over 5° of L_s, 5° of latitude and 9° of longitude; only the daytime observations are included. The data are constructed using the same binning and differencing scheme used to produce Figures 7 and 10d.

As the cloud decays further, the gaps in the belt grow, until cloud in the tropics remains only over Tharsis, Elysium, and Arabia.

[88] Figure 22 shows the water ice opacity averaged over longitude and between 12.5°N and 17.5°N as a function of seasonal. This figure quantitatively captures the evolution of the tropical cloud belt. Opacities can be seen to begin rising just before $L_s = 360°$. The opacity increase is roughly linear from this point until $L_s = 100°–110°$. The peak opacities are roughly 0.2. The decay of the belt begins at this point and is somewhat more rapid than the growth phase. A good fraction of the cloud is gone by $L_s = 140°$, as discussed by *Pearl et al.* [2001], but the cloud belt remains evident until around $L_s = 180°$. This behavior was predicted in the GCM study of *Richardson et al.* [2002], and is explained by increasing temperatures at $L_s = 140°$, and finally decreasing water vapor supply at $L_s = 180°$. Very little ice cloud is observed between $L_s = 180°$ and $L_s = 360°$.

5.2.2. Polar Hoods

[89] The second major feature evident in Figures 20 and 21 is the polar hood. In the zonal-average, polar hood clouds are clearly indicated as arcuate traces on Figure 19 that surround each winter pole. These shapes reflect the location of the polar hood near the growing and decaying seasonal ice caps. The lack of ice opacity poleward of these arcuate traces may represent a drop off in water ice cloud formation resulting from a failure of vapor to penetrate deep into polar night (as suggested by models [*Richardson et al.*, 2002]). However, our scheme does not work well over surfaces with very low emission temperatures, and so these

data probably can't be taken as strong evidence for the absence of water ice inside the polar vortex. It is also important to note that these opacity measurements reflect the presence of cloud ice rather than the aliased signatures of dust. Figure 13 showed that dust opacity is high near the cap edge, consistent with imaging from MOC which suggests intense local storm activity [*Cantor et al.*, 2001; *Wang and Ingersoll*, 2002]. However, comparison of Figures 13 and 20 shows that if dust was being confused for ice in our scheme, the water ice signature in Figure 20 should be strongest near the southern pole at roughly $L_s = 230°$. In fact, despite high dust opacities at that time and location, no water ice opacity is indicated in Figure 20. The polar edge opacities in Figure 20 do, in fact, represent the condensation of water ice in the atmosphere.

[90] Figure 20 shows that the water ice polar hood is stronger in the northern hemisphere than in the southern hemisphere. Unfortunately, there is only sufficient data in the transition from TES year 2 to year 3 to see this, so it remains to be seen whether similar behavior is exhibited every year. In the north, the hood cloud builds steadily from about $L_s = 150°$. The maximum equatorward extent is at roughly $L_s = 270°$, when the cloud is located equatorward of 40°N. The cloud opacity increases and the latitudinal extent increases after $L_s = 230°$. This may be associated with enhanced transport of water to the northern seasonal cap from the rapidly subliming southern seasonal cap, as suggested in the GCM study of *Richardson and Wilson* [2002]. The hood cloud continues to expand and thicken until the end of southern winter, with maximum extent just before
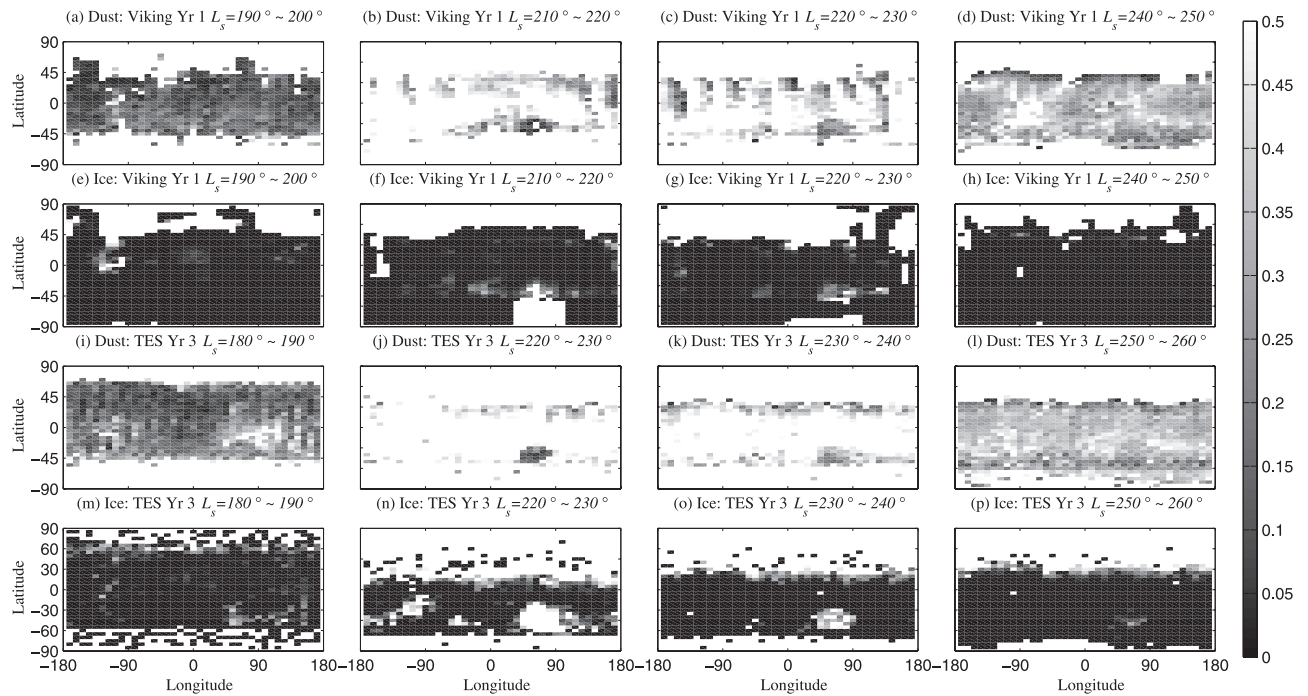
Figure 23. Dust and water ice maps of the1977a and 2001 dust storms. a)–d) Dust opacity from Viking year 1 for the early ($L_s = 190°–200°$), mid- ($L_s = 210°–220°$ and $L_s = 220°–230°$), and late ($L_s = 240°–250°$) stages of the 1977a storm. e)–h) Corresponding maps of water ice opacity for the 1977a dust storm period. Note the development of significant ice opacity in the Hellas Basin. i)–l) Dust opacity from TES year 3 for the 2001 dust storm. m)–p) Corresponding maps of water ice opacity for the 2001 dust storm period.

equinox. The cloud accompanies the retreat of the northern seasonal cap until it expires near northern summer solstice.

[91] In the south, the hood cloud is less continuous than in the north (Figure 20). Distinct peaks in ice opacity occur in mid southern autumn, at solstice, and in mid southern spring. The latter of these distinct thickenings of the hood are evident in both TES years 2 and 3. Unlike the northern hood, the southern hood dies down to essentially zero opacity just before local spring equinox ($L_s = 180°$). This likely reflects a cut-off in the supply of water from the northern hemisphere, and increased southern polar air temperatures associated with dust lifting.

5.2.3. Interaction of Dust and Water Ice During Major Storms

[92] The southern spring time global encircling storms observed by Viking and MGS, 1977a and 2001, are shown in Figure 23. This figure shows four maps for each storm, composed of data averaged over 10° of L_s for each storm, and for the distributions of dust opacity and water ice opacity in each case. For the 1977a storm, it has already been noted by *Martin and Richardson* [1993] that the Hellas basin became depleted of dust relatively early in the storm's evolution (by $L_s = 215°$) and remained clear from that point on (reproduced in Figures 23b and 23c). A similar clearing of the Hellas basin occurred in the 2001 storm (Figures 23j and 23k). Thus, to the extent that two springtime storms represent a database, early clearing of the Hellas basin appears to be a common behavior of such storms.

[93] The water ice cloud distribution during these storm periods is also shown in Figure 23. In both years, during the storms, water ice opacity is elevated along the edge of the cold polar regions in both hemispheres. However, the Hellas basin is associated with particularly large water ice optical depths. These water ice opacities grow and decay rapidly before and after the dust storms. It is unlikely that these water ice opacities result from confusion of dust for water ice in the retrieval scheme. First, elevated dust opacities are evident during these times at locations throughout the tropics and midlatitudes, but ice opacities are high specifically within the basin. Second, dust tends not to be aliased into water ice opacity for the reasons discussed in section 2.3.1 (higher dust amounts produce an underestimate rather than an overestimate of water ice opacity).

[94] The coincidence of low dust opacity and high water ice opacity within the Hellas basin during these storms suggests one of either two interaction processes. Most trivially, the presence of water ice clouds within the Hellas basin could be biasing the retrieved dust opacity to low values, in a similar manner to that already described for the tropical ice cloud belt. Alternatively, the water ice cloud that develops in the Hellas basin may be locally scavenging the dust out of the atmosphere. In either case, the preferential clearing of dust in Hellas that was first discussed by *Martin and Richardson* [1993] appears to be directly traceable to the presence of large amounts of water ice. The existence of the water ice, in turn, is likely due to the sublimation of the seasonal ice cap at this season, and the copious availability of cloud condensation nuclei, in the form of dust.

5.3. Year-to-Year Variability

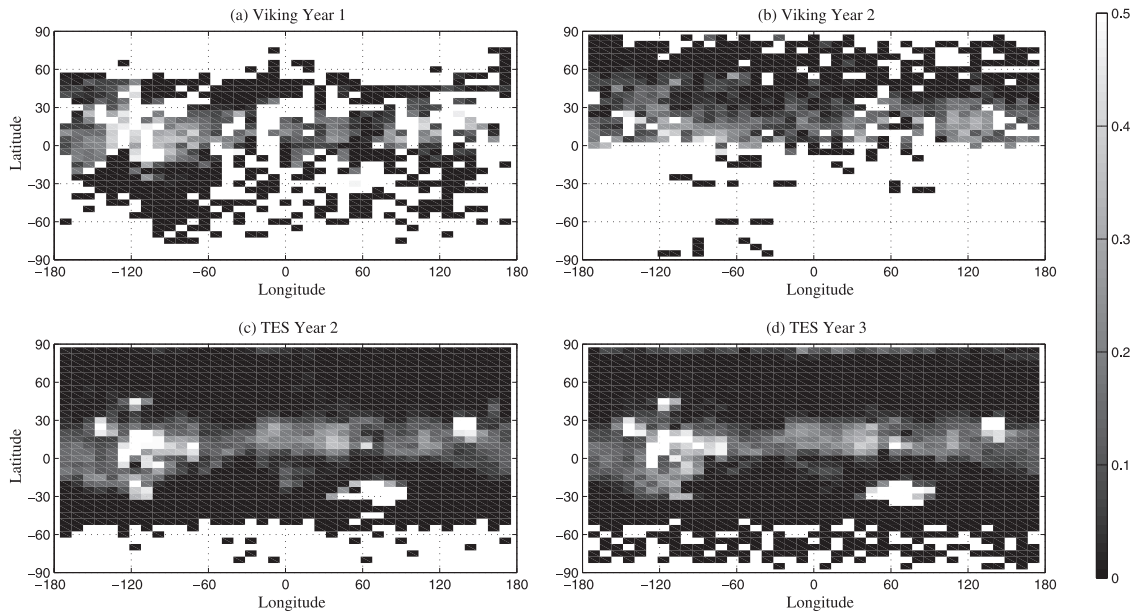[95] Due to the nature of the coverage in different years and from different spacecraft, it is easier to talk about

Figure 24. The distribution of water ice clouds for $L_s = 105° - 130°$. The data are binned in 5° of latitude and 9° of longitude, including only the daytime observation. a) Viking year 1. b) Viking year 2. c) TES year 2. d) TES year 3.

interannual variability (or consistency) of the tropical cloud belt than of the hood clouds. The most that can be said is that from comparison of Viking year 2 and TES year 3 data in Figure 20, very similar hood behavior was exhibited during northern spring in these two widely separated years. In this section we will focus on interannual variability of the tropical water ice cloud belt.

[96] The tropical cloud belt in Viking year 1 at $L_s = 100°$ (Figure 20) seems to be extended much further into the southern hemisphere than at the same season in TES year 2. The situation at this season in Viking year 2 is ambiguous, as data are missing south of the equator (although for mid-northern spring, there appears to be a distinct bias in cloud opacity in favor of the northern tropics). To examine whether the cloud belt was located within a significantly different latitude range during the Viking years as compared to the TES years, we need to look at the geographical distribution of cloud.

[97] Figure 24 shows the distribution of cloud for the period $L_s = 105° - 130°$ for Viking years 1 and 2 and TES years 2 and 3. This seasonal range was chosen as the cloud belt is fully developed and relatively unchanging at this time. The Viking year 2 data provide complete determination of the northern edge of the tropical cloud belt. The familiar concentration of cloud at specific longitudes is seen, as described in section 5.2.1. The location of the northern edge of the belt is consistent with that seen in both years of TES data, suggesting that at least the northern half of the cloud belt has not changed much since the 1970s. The Viking year 2 coverage is spottier on both the northern and southern boundaries of the cloud belt. However, coverage extends just sufficiently far poleward that the northern edge of the belt in year 2 appears to agree with that in year 1 and with the TES years. Southern edge coverage is poorer, but a significant fraction of the Tharsis region is covered. In this region, the TES data show the cloud belt to have its greatest

latitudinal extent, including a significant excursion into the southern hemisphere. The extension of the belt into the southern hemisphere in Viking year 1 is very similar to that in the TES data, again suggesting a very similar cloud belt in all four years. The bias in the Viking year 1 data in favor of the Tharsis sector also explains the apparent difference in tropical belt extent in Figure 20: with only the Tharsis region properly sampled, the zonal average location of the southern belt edge is strongly biased to higher southern latitudes.

[98] Similarities and differences between all four years can be made quantitative by examining plots of opacity differences. Figure 25 shows the difference between the each of the Viking years and each of the TES years, and between TES and Viking. In general, differences are largest where the opacities are largest, with the largest differences being about 0.1 for a total opacity of 0.5 (so about a 20% difference). The pattern of the differences is also somewhat random, suggesting no systematic effects. The one potential exception is over Tharsis between Viking year 1 and both TES years. If the maps are averaged over the cloud belts and differenced, the total opacity difference between any of the years is less than 10%. Thus, to the limit of the quality of the data, it would appear that the tropical cloud belt is locked into a repeatable annual cycle.

[99] The foregoing discussion demonstrates that at its peak, the tropical cloud belt is very repeatable, and that it was just as significant a feature of the atmosphere during the time of the Viking mission as during the MGS mission. However, the TES data suggest some interannual variability in the cloud belt during late northern autumn. In TES year 2, the cloud belt thins quite dramatically after $L_s = 140°$. While a belt can be seen after this, it is optically thinner and less spatially extensive. In TES year 3, $L_s = 140°$ also represents a point of change in the cloud belt, but the decay after $L_s = 140°$ is less rapid than in TES year 2. Specifically, the
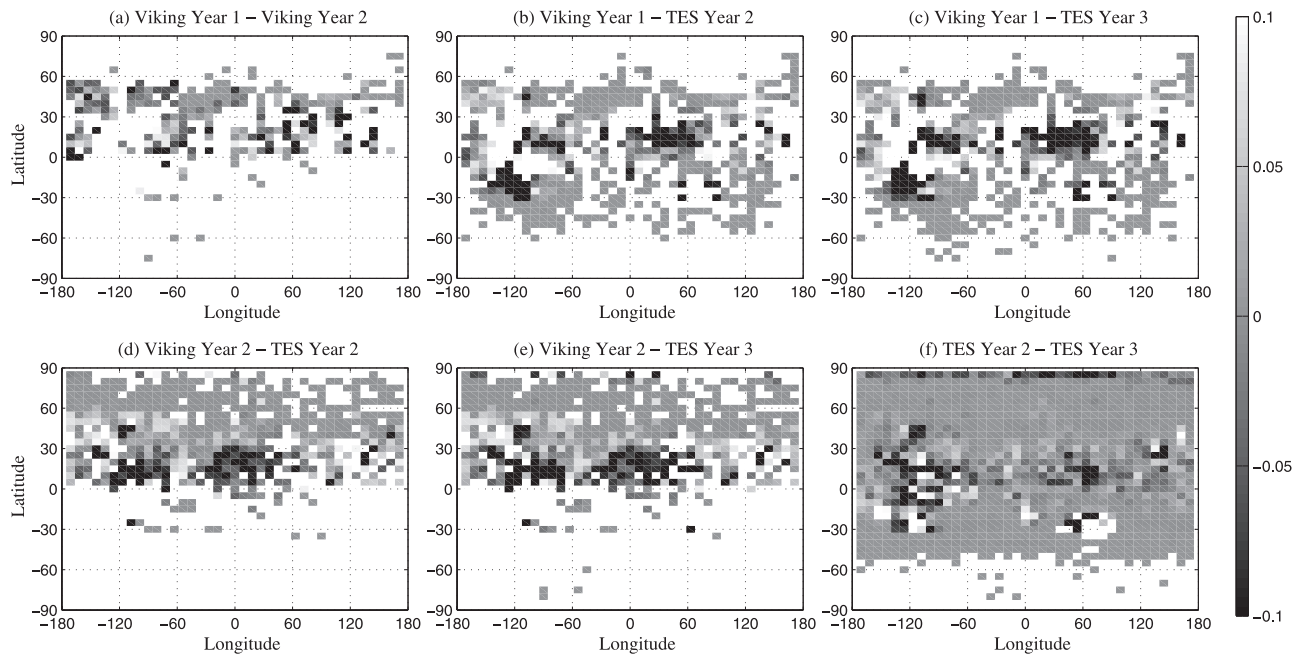
Figure 25. The difference in the water ice opacity between years for $L_s = 105° - 130°$. The data are binned in 5° of latitude and 9° of longitude, including only the daytime observation. a) The difference between Viking year 1 and Viking year 2. b) The difference between the Viking year 1 and TES year 2. c) The difference between the Viking year 1 and TES year 3. d) The difference between the Viking year 2 and TES year 2. e) The difference between the Viking year 2 and TES year 3. f) The difference between the TES year 2 and TES year 3.

belt retains higher opacities and greater extent between $L_s = 140° - 160°$ in year 3. By $L_s = 170°$, the pattern of ice opacity in the two years is similar again, and the cloud belt is essentially dissolved by $L_s = 180°$ in both years.

6. Discussion and Summary

[100] At the heart of this study is the longest, most uniform, and highest spatially and temporally resolved record of the Martian climate yet assembled. The resolution results from the fact that the data were collected from orbiting platforms, while the length results from the duration of and the time separating the various missions (Mariner 9, 1971–1972; Viking, 1976–1980; and MGS, 1997 to present). The uniformity of the record is generated by degrading the relatively high spectral resolution of the Mariner 9 IRIS and the MGS TES infrared spectrometers to generate equivalent IRTM radiometer band brightness temperatures. Along with previous studies, we used the IRTM 15-μm band as a record of mid-level (~25 km) air temperatures [*Martin and Kieffer*, 1979; *Martin*, 1981; *Wilson and Richardson*, 2000], and dust opacities generated from the 9-μm channel band depth with respect to the 7-μm channel continuum [*Martin*, 1986; *Martin and Richardson*, 1993]. A new scheme has been developed as part of this study to derive water ice opacity from the IRTM 11-μm channel ice band, relative to the 20-μm channel continuum.

[101] The requirement for uniformity in the data and careful treatment of coverage biases in the data sets results from the fact that sufficient progress has been made in describing the Martian atmospheric and climatic state over the last decade, that more specific and precise questions are now demanded. During the late 1990s, the major question centered on which of two competing thermal states, differing by 15–20 K, better represented the typical Martian year (specifically, the northern spring and summer seasons) [*Clancy et al.*, 1996]. That question was resolved by *Richardson* [1998] and *Wilson and Richardson* [2000] in favor of the cooler state. Factor-of-two questions regarding dust opacity in these cooler seasons [*Clancy et al.*, 2000] have also been resolved in favor of lower opacity [*Toigo and Richardson*, 2000]. And the question of whether the tropical cloud belt, which is such a major feature of the atmosphere in northern spring and summer in Hubble and MOC images [*Clancy et al.*, 1996; *James et al.*, 1996; *Wang and Ingersoll*, 2002], was also present during the Viking mission has been answered in the affirmative [*Tamppari et al.*, 2000]. To make progress in quantitatively understanding the Martian climate system, we now want to ask questions such as: Exactly how repeatable are northern summer air temperatures, to within a Kelvin or so globally? Exactly how repeatable is the dust opacity cycle to within 10%? What types of dust storm events are possible, and how similar are the different systems in different years? What are the major, repeatable, spatial structures that compose, for example, the tropical cloud belt? What is a typical seasonal cycle of the cloud belt, and how representative is it? The first two questions are important for modeling the annual cycle because they constrain the type of "memory" sites the system must have, and interannual variability would probably provide insight into what type of memory sites were active. The third question is important because it suggests what kind of dynamical structures should be investigated

and modeled in attempts to understand the origin and evolution of dust storms. The latter two questions matter because in trying to model the evolution of the tropical cloud belt, it is important to know which parts of the cloud structure are persistent (and therefore likely to convey real information about formative processes) and which are transient (and therefore unlikely to be captured in detail in the model, except in a statistical sense).

[102] The highest-level conclusion that can be drawn from this work is that the Martian climate executes a seasonal cycle that is highly asymmetric about the equinoxes, and includes both tremendous repeatability from year-to-year and dramatic transience. The data suggest a strong dichotomy between northern spring and summer (when Mars is near aphelion), and southern spring and summer (when the planet is near perihelion) that is related to the eccentric Martian orbit, and which is broadly in line with conventional thinking [*Zurek et al.*, 1992]. This work has potentially placed much tighter constraints on the degree of repeatability of this cycle, with four Mars years of global nighttime air temperature data during northern spring and summer closing to within one degree Kelvin. Using nighttime data alone, these results appear to confirm the idea that Mars' northern summer returns to essentially the same state each year, as first suggested by *Richardson* [1998]. However, our results show an unexpected type of variability in northern spring and summer air temperatures: while nighttime temperature repeat very closely, the daytime temperatures are more varied, with year-to-year variability ranging up to 6 K. Interestingly, the cooler daytime years are ones that follow years with global dust storms. The reason for the daytime-nighttime dichotomy in air temperature behavior is not understood. It does not appear to be a simple noise issue as the mean values of daytime and nighttime temperatures are quite similar, with the nighttime values slightly higher.

[103] The global-average air temperature is very smooth throughout northern spring and summer (especially the nighttime data) with essentially no short-term (days-to-weeks) variability. Very high repeatability is also exhibited in the global-mean dust and water ice opacities. Extraordinary transience is exhibited by the occurrence of dust storms of variable magnitude in southern spring and summer. This aspect of interannual variability has been known for some time, but it would appear that there is potential regularity even in dust storm evolution. Although the combined data set is still of modest duration, we note that dust storms of moderate to great size are developing or decaying near the southern spring period $L_s = 220°-230°$ for all Mars' years for which we have spacecraft observations.

[104] In this work, we have examined the hypothesis, laid out by *Wilson and Richardson* [2000] that the Viking IRTM 15-μm channel was affected by leakage of surface emission and that this leakage can be "corrected" with a simple algorithm. The hypothesis was examined using TES and IRTM *T15* values for northern spring and summer, and from 2 am and 2 pm. The primary prediction, that nighttime IRTM *T15* values should be essentially unaffected by the defect in the instrument, is borne out through good agreement with 2 am TES *T15*. We examined the "correction" procedure outlined by *Wilson and Richardson* [2000], finding it to produce good agreement between 2 pm TES and the corrected IRTM *T15* value.

[105] The dust opacity at the Viking and Pathfinder Lander sites reached their lowest values ($\tau_9 \sim 0.05$) at $L_s = 135°$. This is seen for all the years observed by infrared instruments and for all the Landing sites. Repeatability in the dust cycle is very high, with values closing to considerably less than 10%. The retrieved infrared opacities are very low, and may be biased by inclusion of dust opacity effects in the surface emissivity date used. When uniform emissivities were used, opacities increased by roughly a factor of 2, but year-to-year repeatability was unaffected. Despite this increase, the infrared dust opacity for Pathfinder is lower than the opacity derived by the visible dust opacity measurements obtained by the Pathfinder, even taking into account the 2.5 ratio of visible to infrared opacity derived by *Martin* [1986]. Such offsets are exhibited in all the years observed by infrared instruments. While we demonstrate that the IRTM opacity scheme appears to be biased by the presence of water ice opacity, estimates based on uniform emissivity agree well with TES opacities.

[106] The high degree of repeatability during the northern spring and summer season is of significance as it provides a solid foundation for combining a range of data sets, from different years, to investigate dynamic and climatic processes operating during this portion of the Martian year. For example, these results suggest that the four year record of surface pressure tidal observations at VL1 is likely representative of other years as well. This record suggests little interannual variability in tide forcing during four aphelion seasons [*Wilson and Hamilton*, 1996] and may be used to constrain simulations of dust heating. Similarly, other observations from different spacecraft during different years can likely be used to develop a combined picture of the atmosphere for these seasons, as long as heterogeneity due to spatial and local time coverage is considered.

[107] The lack of variability in northern spring and summer should also simplify the development of theories for the maintenance of the background dust distribution in this season, as it points to a process that is steady on seasonal timescales, and dependent upon annually repeating forcing and conditions. To the extent that water ice clouds may be significant for influencing the dust distribution, the highly-repeatable behavior of water ice clouds during the Viking and MGS periods suggests a similar ability to develop a useful picture of cloud processes and cloud-dust interactions that is generally applicable.

[108] Spatially resolved mapping of dust behavior shows many of the dynamical phenomena observable in visible imaging. Specifically, we find clear support in the infrared for the "dust storm flushing" events in early northern autumn reported from visible imaging by *Cantor et al.* [2001]. These "flushing" events represent a completely new form of dust lifting phenomena that can clearly be traced to an easily understood lofting mechanism: cross frontal winds in baroclinic storm systems. The development of these storms and their entrainment in the western boundary current along the edge of the Tharsis Plateau represents a significant and exciting "teleconnection" process operating in the Martian climate system. We also find significant dust lifting activity along the seasonal cap edges that agrees well with the MOC observation [*Cantor et al.*, 2001]. However, we also find similar activity in the Viking

data sets, suggesting that strong cap edge lifting is a regular part of the current Martian seasonal cycle.

[109] The most significant new retrieval capability developed for this work was for water ice. This involved converting the *Martin* [1986] dust opacity scheme to retrieve water ice opacity at 11-μm, using the 20-μm channel as a surface continuum. We show that this scheme does very well in mapping the spatial distribution of water ice by comparison with simultaneous MOC images. We examined the interannual variability of the northern tropical cloud belt [*Clancy et al.*, 1996] in two Viking and two MGS years, and showed that spatial structure and opacities are essentially identical in early northern summer (opacity values agree to within much less than 10%). We showed the seasonal evolution of the tropical cloud belt structure throughout northern spring and summer, describing the evolution with time. Peak water ice opacities occur near $L_s = 120°$, with the decrease in opacity sharper than the rise. Repeatability in the evolution of the cloud belt is high, except in mid-to-late northern summer. In TES year 2, the cloud belt was initially disrupted by dust activity after $L_s = 140°$ [*Pearl et al.*, 2001], finally decaying after $L_s = 180°$. In TES year 3, the cloud belt decay is smoother, with opacities identical to year 2 before $L_s = 140°$ and after $L_s = 160°$, and higher in between these dates. The other major cloud structure observed in the data was the polar hood. Hood clouds were observed in both hemispheres. In southern summer, the hood exhibits multiple thickening and thinning events through southern spring and summer, presumably associated with the supply of water vapor.

[110] In summary, the Martian climate returns each year to essentially the same state between $L_s = 0°-140°$. This period exhibits repeatability of bulk air temperatures of better than 1 K (if you favor the nighttime data) or 6 K (if you favor the daytime data), with essentially no transience. This period is also associated with the lowest air temperatures, lowest dust opacities, and highest water ice cloud amounts. These bulk climatic results, which represent buttressing and refinement of pictures of the climate presented previously [*Richardson*, 1998; *Wilson and Richardson*, 2000; *Toigo and Richardson*, 2000; *Clancy et al.*, 2000], have recently been supported by MOC imaging of repeatable meteorological phenomena [*Cantor et al.*, 2002]. That we can state that the climate is repeatable within this seasonal range is profoundly different from saying that we understand how the climate operates at these times. The northern spring and summer climate is likely controlled by a mixture of steady (or at least repeatable) dust injection processes, and the interaction of atmospheric dust with atmospheric water. Abundances of the latter are, in turn, controlled by poorly understood exchange processes with the caps and regolith [*Richardson and Wilson*, 2002]. More comprehensive and better vertically resolved observations are sorely needed if we are to understand the workings of climate in this season.

[111] The remainder of the year sees varying degrees of transience in dust and air temperature. Even in the midst of the great variability of "dust storm season", coherent patterns are beginning to emerge (real or coincidental), including high opacities in southern spring ($L_s = 220°-230°$) in every year thus far observed by spacecraft associated with the onset or decay of major dust storms. This study can provide little additional insight into the mechanism of regional and planet-encircling storms beyond those provided by earlier data studies, which in turn do little more than describe what is happening in the atmosphere. Major dust storm development remains a significant unsolved problem of Martian atmospheric and climate dynamics, and requires further modeling and data acquisition.

[112] The collected observations presented in this paper suggest that the Martian atmosphere is driven to repeat similar dynamical behavior by the strong direct influence of solar forcing, and the indirect effect of solar forcing on small scale dust lifting (e.g., dust devils) and on the availability of atmospheric water. Interruptions to this clockwork system occur only when stochastic processes inject massive amounts of atmospheric dust during major dust storms. The lack of significant system "memory" rapidly brings the system back to its repeatable state at the conclusion of these events. The occurrence of these major storms suggests that Mars may possess a memory site, but if so, this memory is likely on the surface with the dust. Observations of interannual variations in surface water ice [*Cantor et al.*, 2002] and atmospheric water vapor (M. Smith, personal communication, 2003) suggest that further memory sites exist, and that the coupled Mars climate system (atmosphere, surface dust deposits, and ice deposits) exhibits vastly more complex long-period behavior than the atmosphere alone.

References

Albee, A. L., Mars 2000, *Annu. Rev. Earth Planet Sci.*, *28*, 281–304, 2000.

Anderson, E., and C. Leovy, Mariner 9 television limb observation of dust and ice hazes on Mars, *J. Atmos. Sci.*, *35*, 723–734, 1978.

Banfield, D., B. J. Conrath, M. D. Smith, P. Christensen, and R. J. Wilson, Forced waves in the Martian atmosphere from MGS TES nadir data, *Icarus*, *161*, 319–345, 2002.

Beish, J. D., and D. C. Parker, Meteorological survey of Mars, 1969–1984, *J. Geophys. Res.*, *95*, 14,657–14,675, 1990.

Briggs, G. A., W. A. Baum, and J. Briggs, Viking Orbiter imaging observations of dust in the Martian atmosphere, *J. Geophys. Res.*, *84*, 2795–2820, 1979.

Cantor, B. A., P. B. James, C. Caplinger, and M. J. Wolff, Martian dust storms: 1999 Mars Orbiter Camera observations, *J. Geophys. Res.*, *106*, 23,653–23,687, 2001.

Cantor, B., M. Malin, and K. S. Edgett, Multiyear Mars Orbiter Camera (MOC) observations of repeated Martian weather phenomena during the northern summer season, *J. Geophys. Res.*, *107*(E3), 5014, doi:10.1029/2001JE001588, 2002.

Christensen, P. R., Martian dust mantling and surface composition: Interpretation of thermophysical properties, *J. Geophys. Res.*, *87*, 9985–9998, 1982.

Christensen, P. R., Variations in Martian surface composition and cloud occurrence determined from thermal infrared spectroscopy: Analysis of Viking and Mariner 9 data, *J. Geophys. Res.*, *103*, 1733–1746, 1998.

Christensen, P. R., and R. W. Zurek, Martian north polar hazes and surface ice: Results from the Viking survey completion mission, *J. Geophys. Res.*, *89*, 4587–4596, 1984.

Christensen, P. R., et al., Thermal Emission Spectrometer experiment: Mars Observer mission, *J. Geophys. Res.*, *97*, 7719–7734, 1992.

Christensen, P. R., et al., Mars Global Surveyor Thermal Emission Spectrometer experiment: Investigation description and surface science results, *J. Geophys. Res.*, *106*, 23,823–23,871, 2001.

Clancy, R. T., D. O. Muhleman, and G. L. Berge, Global changes in the 0–70 km thermal structure of the Mars atmosphere derived from 1975 to 1989 microwave CO spectra, *J. Geophys. Res.*, *95*, 14,543–14,554, 1990.

Clancy, R. T., A. W. Grossman, M. J. Wolff, P. B. James, D. J. Rudy, Y. N. Billawala, B. J. Sandor, S. W. Lee, and D. O. Muhleman, Water vapor saturation at low altitudes around Mars aphelion: A key to Mars climate?, *Icarus*, *122*, 36–62, 1996.

Clancy, R. T., B. J. Sandor, M. J. Wolff, P. R. Christensen, M. D. Smith, J. C. Pearl, B. J. Conrath, and R. J. Wilson, An intercomparison of ground-based millimeter, MGS TES, and Viking atmospheric temperature measurements: Seasonal and interannual variability of temperatures and dust loading in the global Mars atmosphere, *J. Geophys. Res.*, *105*, 9553–9571, 2000.

Colburn, D., J. B. Pollack, and R. M. Haberle, Diurnal variations in optical depth at Mars, *Icarus*, *79*, 159–189, 1989.

Conrath, B. J., Thermal structure of the Martian atmosphere during the dissipation of the dust storm of 1971, *Icarus*, *24*, 36–46, 1975.

Conrath, B. J., J. C. Pearl, M. D. Smith, W. C. Maguire, S. Dason, M. S. Kaelberer, and P. R. Christensen, Mars Global Surveyor Thermal Emission Spectrometer (TES) observations: Atmospheric temperatures during aerobraking and science phasing, *J. Geophys. Res.*, *105*, 9509–9519, 2000.

Fenton, L., J. C. Pearl, and T. Z. Martin, Mapping Mariner 9 dust opacities, *Icarus*, *130*, 115–124, 1997.

Forget, F., F. Hourdin, R. Fournier, C. Hourdin, O. Talagran, M. Collins, S. R. Lewis, P. L. Read, and J.-P. Huot, Improved general circulation models of the Martian atmosphere from the surface to above 80 km, *J. Geophys. Res.*, *104*, 24,155–24,175, 1999.

Goody, R. M., and Y. L. Yung, *Atmospheric Radiation: Theoretical Basis*, Oxford Univ. Press, New York, 1989.

Haberle, R. M., C. B. Leovy, and J. B. Pollack, Some effects of global dust storms on the atmospheric circulation of Mars, *Icarus*, *50*, 322–367, 1982.

Haberle, R. M., J. B. Pollack, J. R. Barnes, R. W. Zurek, C. B. Leovy, J. R. Murphy, H. Lee, and J. Schaeffer, Mars atmospheric dynamics as simulated by the NASA Ames general circulation model: 1. The zonal-mean circulation, *J. Geophys. Res.*, *98*, 3093–3123, 1993.

Haberle, R. M., M. M. Joshi, J. R. Murphy, J. R. Barnes, J. T. Schofield, G. Wilson, M. Lopez-Valverde, J. L. Hollingsworth, A. F. C. Bridger, and J. Schaeffer, GCM simulations of the Mars Pathfinder ASA/MET data, *J. Geophys. Res.*, *104*, 8957–8974, 1999.

Hanel, R., B. C. Conrath, W. Hovis, V. Kunde, P. Lowman, W. Maguire, J. Pearl, J. Pirraglia, C. Prabhakara, and B. Schlachman, Investigation of the Martian environment by infrared spectroscopy on Mariner 9, *Icarus*, *17*, 423–442, 1972.

Jakosky, B. M., and T. Z. Martin, Mars-north-polar atmospheric warming during dust storms, *Icarus*, *72*, 528–534, 1987.

James, P. B., and B. A. Cantor, Martian north polar cap recession: 2000 Mars Orbiter Camera observations, *Icarus*, *154*, 131–144, 2001.

James, P. B., J. F. Bell, R. T. Clancy, S. W. Lee, L. J. Martin, and M. J. Wolff, Global imaging of Mars by Hubble space telescope during the 1995 opposition, *J. Geophys. Res.*, *101*, 18,883–18,890, 1996.

Jaquin, F., P. Gierasch, and R. Kahn, The vertical structure of limb hazes in the Martian atmosphere, *Icarus*, *68*, 442–461, 1986.

Kahn, R. A., The spatial and seasonal distribution of Martian Clouds, and some meteorological implications, *J. Geophys. Res.*, *89*, 6671–6688, 1984.

Kahn, R. A., Ice haze, snow, and the Mars water cycle, *J. Geophys. Res.*, *95*, 14,677–14,693, 1990.

Kahn, R. A., T. Z. Martin, R. W. Zurek, and S. W. Lee, The Martian dust cycle, in *Mars*, edited by H. H. Kieffer et al., pp. 1017–1053, Univ. of Ariz. Press, Tucson, 1992.

Leovy, C. B., The general circulation of Mars: Models and observations, *Adv. Geophys.*, *28a*, 327–346, 1985.

Leovy, C. B., G. Briggs, A. Young, B. Smith, J. Pollack, E. Shipley, and R. Widley, The Martian atmosphere: Mariner 9 television experiment progress report, *Icarus*, *17*, 373–393, 1972.

Lewis, S. R., M. Collins, P. L. Read, F. Forget, F. Hourdin, R. Fournier, C. Hourdin, O. Talagrand, and J.-P. Huot, A climate database of Mars, *J. Geophys. Res.*, *104*, 24,177–24,194, 1999.

Malin, M. C., et al., Mars Observer Camera, *J. Geophys. Res.*, *97*, 7699–7718, 1992.

Martin, L., and R. W. Zurek, An analysis of the history of dust activity on Mars, *J. Geophys. Res.*, *98*, 3221–3246, 1993.

Martin, T. Z., Mean thermal and albedo behavior of the Mars surface and atmosphere over a Martian year, *Icarus*, *45*, 427–446, 1981.

Martin, T. Z., Thermal infrared opacity of the Mars atmosphere, *Icarus*, *66*, 2–21, 1986.

Martin, T. Z., Mass of dust in the Martian atmosphere, *J. Geophys. Res.*, *100*, 7509–7512, 1995.

Martin, T. Z., and H. Kieffer, Thermal infrared properties of the Martian atmosphere: 2. The 15 μm band measurements, *J. Geophys. Res.*, *84*, 2843–2852, 1979.

Martin, T. Z., and M. I. Richardson, New dust opacity mapping from Viking infrared thermal mapper data, *J. Geophys. Res.*, *98*, 10,941–10,949, 1993.

Murphy, J. R., O. B. Toon, R. M. Harberle, and J. B. Pollack, Numerical simulations of the decay of Martian global dust storms, *J. Geophys. Res.*, *95*, 14,629–14,648, 1990.

Murphy, J. R., R. M. Harberle, O. B. Toon, and J. B. Pollack, Martian global dust storms: Zonally symmetric numerical simulations including size-dependent particle transport, *J. Geophys. Res.*, *98*, 3197–3220, 1993.

Newman, C. E., S. R. Lewis, P. L. Read, and F. Forget, Modeling the Martian dust cycle: 1. Representations of dust transport processes, *J. Geophys. Res.*, *107*(E12), 5123, doi:10.1029/2002JE001910, 2002.

Palluconi, F. D., and H. H. Kieffer, Thermal inertia mapping of Mars for 60°S to 60°N, *Icarus*, *45*, 415–426, 1981.

Pearl, J. C., M. D. Smith, B. J. Conrath, J. L. Bandfield, and P. R. Christensen, Observations of Martian ice clouds by the Mars Global Thermal Emission Spectrometer, *J. Geophys. Res.*, *106*, 12,325–12,338, 2001.

Peterfreund, A. R., Contemporary aeolian processes on Mars: Local dust storms, Ph.D. thesis, Ariz. State Univ., Tempe, 1985.

Peterfreund, A. R., and H. H. Kieffer, Thermal infrared properties of the Martian atmosphere, 3, Local dust clouds, *J. Geophys. Res.*, *84*, 2853–2863, 1979.

Pleskot, L. K., and E. D. Miner, Time variability of Martian bolometric albedo, *Icarus*, *45*, 179–201, 1981.

Pollack, J. B., D. S. Colburn, F. M. Flasar, R. Kahn, C. E. Carlston, and D. Pidek, Properties and effects of dust suspended in the Martian atmosphere, *J. Geophys. Res.*, *84*, 2929–2945, 1979.

Pollack, J. B., M. E. Ockert-Bell, and M. K. Shepard, Viking Lander image-analysis of Martian atmospheric dust, *J. Geophys. Res.*, *100*, 5235–5250, 1995.

Richardson, M. I., Comparison of microwave and infrared measurements of Martian atmospheric temperatures: Implications for short-term climate variability, *J. Geophys. Res.*, *103*, 5911–5918, 1998.

Richardson, M. I., and R. J. Wilson, Investigation of the nature and stability of the Martian seasonal water cycle with a general circulation model, *J. Geophys. Res.*, *107*(E5), 5031, doi:10.1029/2001JE001536, 2002.

Richardson, M. I., R. J. Wilson, and A. V. Rodin, Water ice clouds in the Martian atmosphere: General circulation model experiments with a simple cloud scheme, *J. Geophys. Res.*, *107*(E9), 5064, doi:10.1029/2001JE001804, 2002.

Santee, M. L., and D. Crisp, Thermal structure and dust loading of the Martian atmosphere during late southern summer: Mariner 9 revisited, *J. Geophys. Res.*, *98*, 3261–3279, 1993.

Schneider, E. K., Martian great dust storms: Interpretive axially symmetric models, *Icarus*, *55*, 302–331, 1983.

Siili, T., R. M. Haberle, and J. R. Murphy, Sensitivity of Martian southern polar cap edge winds and surface stresses to dust optical thickness and to the large-scale sublimation flow, *Adv. Space. Res.*, *19*, 1241–1244, 1997.

Slipher, E. C., *The Photographic Story of Mars*, Northland, Flagstaff, Ariz., 1962.

Smith, M. D., J. C. Pearl, B. J. Conrath, and P. R. Christensen, Mars Global Surveyor Thermal Emission Spectrometer (TES) observations of dust opacity during aerobraking and science phasing, *J. Geophys. Res.*, *105*, 9539–9552, 2000.

Smith, M. D., et al., One Martian year of atmospheric observations by the Thermal Emission Spectrometer, *Geophys. Res. Lett.*, *28*, 4263–4266, 2001a.

Smith, M. D., J. C. Pearl, B. J. Conrath, and P. R. Christensen, Thermal Emission Spectrometer results: Atmospheric thermal structure and aerosol distribution, *J. Geophys. Res.*, *106*, 23,929–23,945, 2001b.

Smith, M. D., et al., Thermal Emission Spectrometer observations of Martian planet-encircling dust storm 2001A, *Icarus*, *157*, 259–263, 2002.

Smith, P. H., and M. Lemmon, Opacity of the Martian atmosphere measured by the Imager for Mars Pathfinder, *J. Geophys. Res.*, *104*, 8975–8986, 1999.

Tamppari, L. K., R. W. Zurek, and D. A. Paige, Viking era water-ice clouds, *J. Geophys. Res.*, *105*, 4087–4107, 2000.

Toigo, A. D., and M. I. Richardson, Seasonal variation of aerosols in the Martian atmosphere, *J. Geophys. Res.*, *105*, 4109–4121, 2000.

Tomasko, M. G., L. R. Doose, M. Lemmon, P. H. Smith, and E. Wegryn, Properties of dust in the Martian atmosphere from the Imager on Mars Pathfinder, *J. Geophys. Res.*, *104*, 8987–9007, 1999.

Toon, O. B., J. B. Pollack, and C. Sagan, Physical properties of the particles composing the Martian dust storm of 1971–1972, *Icarus*, *30*, 663–696, 1977.

Vasavada, A. R., et al., Surface properties of Mars' polar layered deposits and polar landing sites, *J. Geophys. Res.*, *105*, 6961–6969, 2000.

Wang, H., and A. P. Ingersoll, Martian clouds observed by Mars Global Surveyor Mars Orbiter Camera, *J. Geophys. Res.*, *107*(E10), 5078, doi:10.1029/2001JE001815, 2002.

Wang, H., M. I. Richardson, R. J. Wilson, A. P. Ingersoll, A. D. Toigo, and R. W. Zurek, Cyclones, tides, and the origin of a cross-equatorial dust storm on Mars, *Geophys. Res. Lett.*, *30*(9), 1488, doi:10.1029/2002GL016828, 2003.

Warren, S. G., Impurities in snow: Effects on albedo and snow melt, *Ann. Glaciol.*, *5*, 177–179, 1984.

Wilson, R. J., A general circulation model simulation of the Martian polar warming, *Geophys. Res. Lett.*, *24*, 123–127, 1997.

Wilson, R. J., Evidence for diurnal peroid Kelvin waves in the Martian atmosphere from Mars Global Surveyor TES data, *Geophys. Res. Lett.*, *27*, 3889–3892, 2000.

Wilson, R. J., and K. P. Hamilton, Comprehensive model simulation of thermal tides in the Martian atmosphere, *J. Atmos. Sci.*, *53*, 1290–1326, 1996.

Wilson, R. J., and M. I. Richardson, Comparison of Mars GCM dust storm simulations with Viking mission observations, in *The Fifth International Conference on Mars* [CD-ROM], abstract 6234, *LPI Contrib. 972*, Lunar and Planet. Inst., Houston, Tex., 1999.

Wilson, R. J., and M. I. Richardson, The Martian atmosphere during the Viking mission, 1. Infrared measurements of atmospheric temperatures revisited, *Icarus*, *145*, 555–579, 2000.

Zurek, R. W., and L. J. Martin, Interannual variability of planet-encircling dust storms on Mars, *J. Geophys. Res.*, *98*, 3247–3259, 1993.

Zurek, R. W., J. R. Barnes, R. M. Haberle, J. B. Pollack, J. E. Tillman, and C. B. Leovy, Dynamics of the atmosphere of Mars, in *Mars*, edited by H. H. Kieffer et al., pp. 835–933, Univ. of Ariz. Press, Tucson, 1992.

J. Liu and M. I. Richardson, Division of Geological and Planetary Sciences, California Institute of Technology, MS 150-21, Pasadena, CA 91125, USA. (mir@gps.caltech.edu)

R. J. Wilson, NOAA/Geophysical Fluid Dynamics Laboratory, Princeton, NJ 08540, USA. (rjw@gfdl.noaa.gov)